IMPROVED WALL AND LUMEN IMAGE ACQUISTION AND PROCESSING FOR CARDIAC AND PERIPHERAL MAGNETIC RESONANCE

A Dissertation
Presented to the Faculty of the Graduate School
of Cornell University
in Partial Fulfillment of the Requirements for the Degree of
Doctor of Philosophy

by

Keigo Kawaji

August 2012

IMPROVED WALL AND LUMEN IMAGE ACQUISTION AND PROCESSING FOR CARDIAC AND PERIPHERAL MAGNETIC RESONANCE

Keigo Kawaji, Ph.D.

Cornell University 2012

Magnetic Resonance Imaging (MRI) is regularly used for routine diagnostics in clinical medicine today. It is a versatile imaging modality that can be tailored to provide anatomical and functional information for clinicians to assess a vast range of diseases without surgical or invasive interventions. Over the last several decades, over thousands of clinical MRI techniques have been developed for the advancement of medicine.

Post-processing of routinely acquired MR image or data is one area where such innovation happens. Specifically, these methods use dedicated methods or algorithms to extract clinically relevant parameters that can aid in the diagnostics of diseases. In cardiac MRI, processing of cinematic images of left ventricular motion throughout the cardiac cycle was considered to be challenging, as it required the manual segmentation of the left ventricular blood volume and myocardium from over 200 images – from 8-10 slices over 20-28 temporal frames. In this case, an automated segmentation algorithm of the LV allows rapid generation of volumetric filling curves, which can be further analyzed to assess the presence or absence of diastolic dysfunction.

Another example of MR technology development happens in pulse sequence design, where novel acquisition methods are programmed to allow imaging tailored to a specific

anatomy, such as the arterial vessel wall in the peripheral arteries. Vessel walls are difficult to visualize using standard MRI approaches, and novel pulse sequence components have been explored to provide a black-blood effect, which provides improved contrast between the vessel wall and the darkened blood signal.

Finally, technology development on the MRI scanner to enable real-time feedback during data acquisition is a challenging, yet an exciting area of research with tremendous potential applications in the clinical arena. One such example is in coronary artery imaging, which faces the challenges of acquiring high-quality images of the moving heart. In this work, a 2D fat image snapshot – called a navigator – is developed to directly monitor the epicardial fat surrounding the coronary arteries at every heartbeat, and is incorporated into a real-time interactive software that allows rapid setup and efficient motion extraction on a standard clinical scanner.

BIOGRAPHICAL SKETCH

Keigo Kawaji was born in Mito City, Japan in 1984. He grew up in Toronto, Ontario, Canada before attending Duke University, where he received a Bachelor of Science in Engineering degree with Distinction in Biomedical Engineering, with a second major in Bachelor of Arts in Mathematics in 2007. He joined the Department of Biomedical Engineering at Cornell University in the Fall of the same year, and received a Master of Science degree in Biomedical Engineering in 2010.

This work is dedicated to my parents and my sister.

This work is also dedicated to Richard Hoshino and Tom Griffiths, two tremendous teachers who have taught me a very important life lesson.

In their spirit, I hereby offer the work here in Paying forward to Humanity.

ACKNOWLEDGMENTS

I’ve been truly blessed to have the mentors, colleagues, family and friends, who have all helped me through this journey. I would first like to express my deepest gratitude for my advisor Yi Wang, who has greatly influenced and supported my pursuit of a career in magnetic resonance imaging research. He has always offered his guidance and support as a very enthusiastic, positive, and a passionate advisor, and has provided me the virtually unlimited resources to hone my skills in MR technology development and to conduct original research. I am truly indebted to Yi for the opportunity to work under his guidance and tutelage.

I would also like to thank Martin Prince, who has been a very insightful advisor and a tremendous clinical resource on all of my projects. I appreciate the many opportunities where he has given me his insights to think from a clinician’s viewpoint, and the ensuing stimulating discussions. Dr. Prince has taught me the importance of thinking outside the box, maintaining successful collaborations in medical research, and providing me clinical input for all my work.

I also thank Jonathan Weinsaft, Thanh Nguyen, and Pascal Spincemaille, who have all closely guided me through different phases of my graduate training as a predoctoral researcher. They have shown me how to conduct scientific research in a proper manner, each spending countless hours in support of my skills and technique development. Much of my expertise in MR physics, pulse sequence programming, MR hardware architecture, and image post-processing can be attributed to their willingness, passion, and kindness to both teach and assist.

I’d like to express my gratitude to all postdocs, clinical fellows, and graduate students in the Cornell MRI Laboratory group: of note, I especially thank Jing Liu, Yanchun Zhu, and Mitchell

Cooper for sharing their infectious passions in cardiac MR research. I also appreciate the extended friendships with Grace Choi, Tian Liu, Ildar Khalidov, James Ledoux, Wei Zhang, Michelle Cerilles, Mukta Agrawal, Nandadeepa Thimappa, and Lisa Teahan outside of the workplace during my four years in New York. I thank all other members of the Cornell MRI Laboratory group, as well as Yang Zhang, Honglei Zhang, Priscilla Winchester, Beatriu Reig, Andrew Shih, Zhitong Zou, Silvena Dutrel, Moazzem Kazi, Christopher Chu, Dorinna Mendoza, Ashish Raj, Carlo Salustri, Rebecca Cramer, Karen Matthews and Belinda Floyd for their support. I am also thankful to the MRI technologists at the Vascular MR center, notably Minh Chao, Edna Hong, Joseph Agosta, Ciro Colandrea, as well as the entire nursing and administrative staff at the 416 East 55th street MRI Center. I am truly blessed to have spent the last four years in the company of such tremendous cohort.

I acknowledge here my family and friends, who have provided tremendous support throughout my graduate training. I offer the deepest of my gratitude for my parents, Masahiro and Harumi Kawaji, and to my sister, Naomi, as they have always been the backbone of my strength over the past five years.

And dear my friends – thank you for the occasional reunions together; the sightseeing visits around New York City; the hiking trails upstate and the beach, rafting, and ski trips; the bicycle rides; the picnics; the dinners; and the camaraderie on the basketball courts and the softball fields – I'm truly grateful for all the company and support over the past five years. I'm greatly indebted to all of you for making the ups of graduate life vastly more enjoyable, and the rigors of being a PhD student more manageable; I'm especially thankful to Amrith Krushnakumaar, William Sang Lee, Stephanie Chiu, and Calen Harrison for regularly being in touch all the way from the start to the end of my training, and would also like to thank Ronal Abraham, Shih-en Lu, Ye Wang, Serge Reshetnikov, Ralph Furmaniak, Clare Park, Craig Reeson, Stephanie Guan, Sophia Yang, Ivan Qu, Mekhala Raghupathy, Mitesh Patel, and many others for joining my occasional strolls away from MRI research that were both refreshing and enlightening.

Finally, I would like to acknowledge my committee members: Yi Wang, Peter Doerschuk, David Christini and Jonathan Weinsaft.

--

Here, I would like conclude by offering a tribute to two individuals who, with their tremendous passion for mathematics and science, have brightly guided my path thus far in a career as a scientific researcher. They are Richard Hoshino and Tom Griffiths, both of whom are among the best in the art of inspiring students through excellent teaching. I first met Richard and Tom as an excited 10th grader attending a summer math camp, and later had the opportunity to learn as a junior instructor under them in the same program, teaching some of the brightest 8th through 10th graders from all across Canada. Richard was a tremendous role-model for many students including myself, and has dedicated a career thus far in guiding many to become truly enthusiastic about math and science. Tom, who I consider the quintessential authority in the art of teaching, has taught me my most important lesson in life – he always quoted: *"Paying forward to Humanity"* which is the reason why he loves to teach, and this statement has always remained very close to my heart. Both Richard and Tom continue to inspire, motivate, and empower the next generation of young minds through teaching exciting mathematics and science. As a student empowered by these two spectacular individuals, I humbly offer this thesis as my contribution towards *Paying forward to Humanity*.

TABLE OF CONTENTS

LIST OF TABLES

LIST OF FIGURES

Chapter 1

INTRODUCTION

Magnetic resonance imaging (MRI) is a noninvasive imaging technique used to visualize anatomical structures. Using the same principles as nuclear magnetic resonance (NMR), MRI makes use of a strong magnetic field to align the magnetization of water molecules for imaging. Specifically, MRI technology excites the aligned magnetization using radio frequency pulses while encoding the positional information using a spatially varying magnetic gradient field, which allows the reconstruction of anatomical images.

Cardiac MRI offers a noninvasive method in the diagnostic imaging of cardiovascular diseases. Alternative modalities such as x-ray radiography and computerized tomography expose patients to ionizing radiation, and are therefore unsuited for repeatable diagnostic screening. Additionally, MR assessment of coronary artery diseases has significant advantages over assessments using X-ray and CT for detection of stenosis, as well as IVUS for vessel wall plaque assessment. Unlike the other invasive techniques, MRI offers a noninvasive alternative.

MR technology development has therefore become an area of great interest for routine assessment of cardiovascular and peripheral vascular diseases.

1.1 Summary of Contributions

In this thesis, three new developments in cardiac and vascular magnetic resonance imaging are proposed. First, a diagnostic indicator of diastolic dysfunction is developed through volume filling curve assessment derived from routine clinical cine cardiac MR images. Second, a large-volume black-blood suppression technique for assessment of the vessel wall is developed, and its feasibility is demonstrated in the imaging of the popliteal artery. Finally, a 2D fat image navigator-based coronary MR Angiography (CMRA) technique with direct coronary artery motion tracking for real-time gating and motion correction is developed. This novel method addresses cardiac and respiratory motion, and thereby allows fast, navigator-efficient, and high-quality CMRAs potentially suited for routine clinical use.

1.2 LV Diastolic Assessment

Chapter 3 presents a novel image post processing method in detecting diastolic dysfunction. Cardiac Magnetic Resonance (CMR) is established for assessment of left ventricular (LV) systolic function, but has not been widely used in diastolic assessment. A model-free automated segmentation algorithm is used on cine-CMR images to rapidly generate LV volume filling curves through one cardiac cycle. From the volume filling curves, diastolic function parameters, including a novel index – Diastolic Volume Recovery, calculated as percent diastole required for 80% stroke volume recovery – are measured. This method demonstrates that the automated cine-CMR segmentation-derived LV filling profiles may be used in the assessment of diastolic dysfunction. A patient study (n=101) has demonstrated that the cohort with diastolic dysfunction have prolonged diastolic filling intervals, which are associated with echo-evidenced diastolic dysfunction independent of clinical and imaging variables.

1.3 Black-Blood Peripheral Vessel Wall Imaging

Chapter 4 develops a large-volume 3D black-blood vessel wall MRI sequence. A flow-independent T2-prepared inversion recovery black-blood magnetization preparation is employed to suppress luminal signal, and is combined with either a 3D fast spin echo readout employing variable flip-angles for extended echo train, or a 3D balanced steady-state free precession sequence with high SNR efficiency for vessel wall imaging. This technique is independent of flow, and demonstrates effective blood suppression and good wall visualization over a large 3D volume coverage of the popliteal artery wall, thereby minimizing any flow-based artifacts that are observed with alternative black-blood luminal signal suppression techniques.

1.4 2D Fat Image Navigator-based Coronary MRA

Chapter 5 presents a free-breathing coronary angiography sequence that incorporates a novel method to directly track coronary artery motion through a spectrally and spatially selective excitation of epicardial fat surrounding the targeted coronary arteries. The technique integrates prospective navigator gating and retrospective motion correction from the extracted coronary motion into a 3D SSFP coronary MRA sequence to minimize respiratory motion-based artifacts. A low-resolution 2D navigator image of the epicardial fat is generated and processed in real-time immediately prior to CMRA imaging signal acquisition, which provides a feedback guided acquisition of the imaging volume in real-time. Further improvements in image quality are made by retrospectively correcting for translational motion using the 2D displacements from the navigator image.

Chapter 2

BACKGROUND

A typical magnetic resonance (MR) scanner has four major hardware components: the magnet, the transmitter coils, the gradient coils, and the receiver coils. In addition to these four components, the MR system includes a scanner control chassis, which includes the processors and boards to synchronously manipulate the RF, gradient waveforms and the readout with significant precision, and an additional console to allow operator control as well as basic image post processing.

The scanner components on the MRI scanner are manipulated with 4 microsecond precision, and this is achieved by a combination of carefully designed and timed RF transmission and gradient waveforms, as well as timing the data acquisition readout. The programming of the carefully aligned waveforms on the MRI is known as pulse sequence design, and a standard MRI scanner from major vendors including GE, Philips, and SIEMENS would already include a wide variety of product MRI pulse sequences. Each pulse sequence has a unique combination of excitation, gradient encoding, and acquisition of spectral response using the receiver coil; therefore MRI can be used to collect a wide variety of anatomical images, extract tissue characteristics, and can also be combined with dedicated reconstruction schemes to further extract parameters that are clinically relevant for diagnostics.

MRI technology development can loosely fit into one of two categories; either in data acquisition, which includes the development of pulse sequences, new scanner hardware, or any innovation performed directly on the scanner or during the scan: or alternatively in post-processing, which extracts useful information out of the acquired MRI k-space data for clinical diagnostics.

Accordingly, this chapter is divided into two major parts; the first offers a brief overview of each hardware component and explores how MRI has the versatility to generate a wide variety of pulse sequences for a significant number of applications. The second offers an overview of the MR hardware architecture, and provides two examples of novel technology development. This chapter establishes a background on how MR technology development is tailored to solve the existing clinical problems, which is discussed further in chapters 3-5. A more complete overview of MR physics can be found in (1) by Mark Haacke. Also, (2) by Bernstein et al offers greater insights into details and implementations of pulse sequence design that is discussed in **2.1.6**.

2.1 The Components of the MR Scanner Hardware

2.1.1 Magnet - Polarization

The main magnet yields a large and uniform magnetic field B_0 (in units of Tesla, T) at the center of the scanner bore. The large external field influences molecules with an intrinsic magnetization moment to become polarized. For human imaging applications, water molecules and to a lesser extent triglyceride molecules contained in fat are known to have an angular momentum, referred to as *spin*.

The MRI signal excitation and acquisition relies on polarizing these *spins* under the influence of a strong magnetic field B_0. The aggregate behavior of these *spins* would align in an either parallel or anti-parallel manner to the direction of the field, and is often called the *net magnetization moment vector*. Without the presence of such a field, the magnetic moment from each water molecule will point in a random direction, resulting in a net moment of zero. In a polarized state, the *spins* aligned in the anti-parallel direction are in a slightly higher energy state than those aligned in parallel direction, resulting in a net 5 parts per million spins points in the parallel direction. The MRI uses the other hardware components to excite, manipulate, and acquire signal from these polarized bulk spins, as explained in this chapter.

2.1.2 The Transmission Coils - Excitation

The second component of the MRI is the radiofrequency (RF) transmitter coil, which uses RF pulses to excite the polarized molecules. Under the influence of a strong magnetic field, a small net magnetization pointing in the B_0 direction is not composed of static spins; instead, each of these spins acquires a torque due to the interaction with the field, resulting in a *precession* about the B_0 axis describing a conical shape. Therefore, the net magnetization is in fact the aggregate sum of such *precessing* spins, which is a dynamical equilibrium in the direction of B_0. The *precession* of these spins would occur at a natural frequency proportional to the field strength, and the concentration of excited spins in the tissue. This linear relationship, known as the Larmor equation, can be described as, where ω is known as the *Larmor* frequency, γ is the *gyromagnetic ratio* that is dependent on tissue characteristics, or material properties, and *B* is the magnetic field strength. For protons (hydrogen atoms) in water molecules, γ = 42.18 MHz/T.

An RF field which includes the *Larmor frequency* can be used to excite the net magnetization vector, which results in tipping the net magnetization vector away from the z-direction into the x-y plane. This excited magnetization vector then exhibits *Larmor precession* at a frequency proportional to the main field $\vec{\boldsymbol{\omega}} = -\gamma\vec{\boldsymbol{B}}$, where vector $\vec{\boldsymbol{B}}$ is the main magnetic field and $-\gamma\vec{\boldsymbol{B}}$ indicates a clockwise spin.

The *Bloch Equation* can be derived from the above, and is used to model the behavior of magnetization in a magnetic field over a course of time.

$$\frac{d\vec{\boldsymbol{m}}}{dt} = -\gamma\vec{\boldsymbol{B}} \times \vec{\boldsymbol{m}} \qquad \dots [2.1]$$

When a transmit coil is turned on, a small field b_1 that is substantially smaller than the main magnetic field is created. From the Bloch equation, the following expression describes the field experienced by the precessing spins:

$$\vec{\boldsymbol{B}} = B_0\hat{\boldsymbol{z}} + b_{1x}\hat{\boldsymbol{x}} + b_{1y}\hat{\boldsymbol{y}} \qquad \dots [2.2]$$

where b_{1x} and b_{1y} are the x and y components of b_1, respectively.

The above can be broken down into a matrix equation in the x, y, and z coordinate system, as follows:

$$\begin{bmatrix} \dot{m}_x \\ \dot{m}_y \\ \dot{m}_z \end{bmatrix} = -\gamma \cdot det \begin{vmatrix} \hat{x} & \hat{y} & \hat{z} \\ b_{1x} & b_{1y} & B \\ m_x & m_y & m_z \end{vmatrix} \qquad \dots [2.3]$$

In complex number form, this becomes:

$$\dot{m}_x + i\dot{m}_y = -\gamma\left[\left(b_{1y} - ib_{1x}\right)m_z + \left(-m_y + im_x\right)B\right] \qquad \ldots [2.4]$$

which is analogous to:

$$\dot{M}_\perp = -i\gamma M_\perp B + \gamma\left(b_{1y} - ib_{1x}\right)M_0 \qquad \ldots [2.5]$$

This is a 1st order differential equation with the following solution:

$$M_\perp = -\gamma M_0 \int b_1(t')\, e^{-i\omega_0 t'} dt' e^{-i\omega t} \qquad \ldots [2.6]$$

The integral expression in this solution is equivalent to the Fourier Transform of $B_1^*(\omega)$. The RF field has to have a component that overlaps with the resonance frequency. In order to achieve this, a time-dependent b_1 field is considered:

$$b_1^*(t) = b_1^* e^{-i\omega_0 t} \qquad \ldots [2.7]$$

Several observations can be made in regards to RF excitation. First, a polychromatic RF pulse can be designed to excite a specific spectral bandwidth. For example, a short pulse replicating a Dirac delta function – which results in a non-selective *hard* excitation of all frequency spectrums in the Fourier domain - will tip the net magnetization moment vector *precessing* at all frequencies. A more selective excitation pulse can be designed using a pulse length with a longer duration. Advanced and optimized RF pulse design methods, such as those proposed by Shinnar and Le Roux (SLR designed pulses) (3-6) can be used to create RF waveforms tailored to excite a specific spectral bandwidth or slab thickness, provided that the RF waveform is sufficiently long. In such spectrally selective RF excitations, the pass band can be centered on different frequencies. **Figure 2.1** shows examples of two SLR-designed 16 msec RF waveforms and its spectral responses.

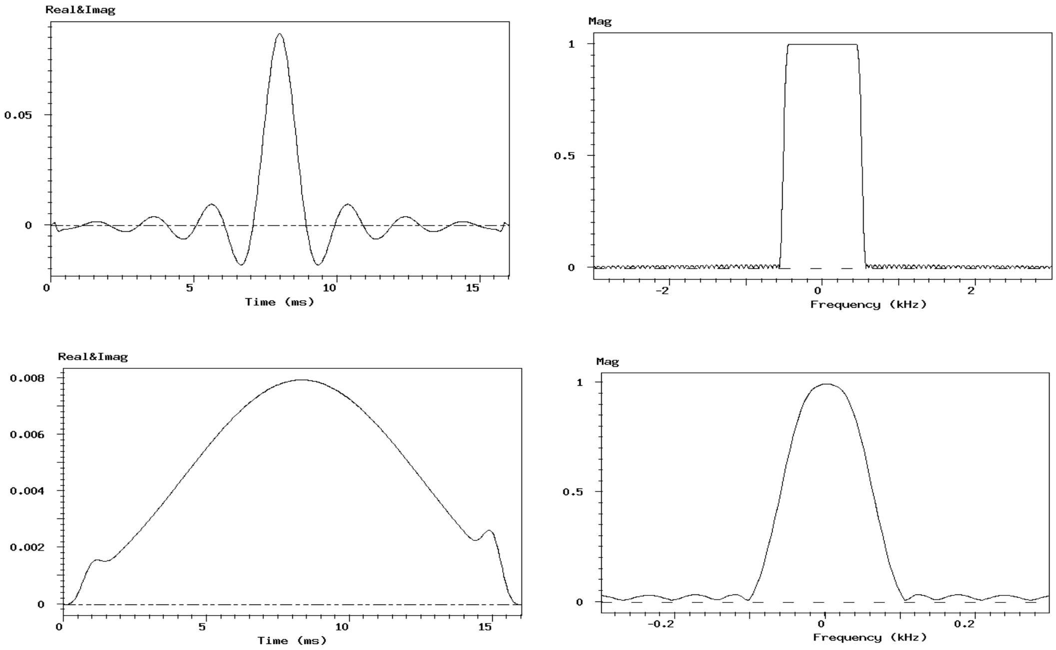

Figure 2.1 Shinnar-Le Roux optimized 16 msec RF excitation pulses.
The time profile (top left), and the frequency response (top right) of a 16 msec SLR-designed RF excitation pulse with a bandwidth of 1kHz and linear phase, corresponding to the flip to occur at the true center of the RF time profile. A 16 msec minimum-phase, 100Hz bandwidth RF pulse timecourse (bottom left) and its response (bottom right) are also shown. In general, narrower pass-bands require a longer RF pulse duration, and imperfections may be observed when substantial constraints are placed on the SLR designed pulses (ie. short bandwidth, short pulse duration).

2.1.3 The Gradient Coils - Spatial Encoding

The third component is a set of gradient coils – noting a few exceptions recently introduced in research environment (7-9), the vast majority of clinical MR systems today typically have a set of three gradient coils, each capable of producing a linear field that are orthogonal to one another in the right-left (x), anterior-posterior (y), and superior-inferior (z) directions. The linear gradient fields can be used to introduce a variation in the response of the polarized molecules to an RF excitation by its position in the physical space. This process, known as *spatial encoding*, incorporates the positional information into the aggregate signal produced by the *precessing* spins.

The spatial encoding mechanism can be explained by the following example. A gradient coil is set up in such a way that the magnetic field varies in space as given by a gradient vector $\vec{\boldsymbol{G}}$, governed by the equation:

$$B(\vec{\boldsymbol{r}}) = B_0 + \vec{\boldsymbol{G}} \cdot \vec{\boldsymbol{r}} = B_0 + G_x x + G_y y + G_z z \qquad \ldots [2.8]$$

The Larmor Precession equation can now be expressed as follows:

$$\omega = \gamma\left(B_0 + \vec{\boldsymbol{G}} \cdot \vec{\boldsymbol{r}}\right) = \omega_0 + \gamma \vec{\boldsymbol{G}} \cdot \vec{\boldsymbol{r}} \qquad \ldots [2.9]$$

The rotating net magnetization vector, $\boldsymbol{m}(\vec{\boldsymbol{r}}, \boldsymbol{t})$, can be described as:

$$\boldsymbol{m}(\vec{\boldsymbol{r}}, \boldsymbol{t}) = m_0(\vec{\boldsymbol{r}}) e^{-i\omega_0 t} e^{-i\gamma \vec{\boldsymbol{G}} \cdot \vec{\boldsymbol{r}} t} \qquad \ldots [2.10]$$

where $\boldsymbol{m_0}(\vec{\boldsymbol{r}})$ is the initial value at t = 0. Now let us recall the Signal equation, for which $\boldsymbol{\rho}(\vec{\boldsymbol{r}})$ accounts for $\boldsymbol{m_0}(\vec{\boldsymbol{r}})$. It follows that:

$$\boldsymbol{S}(t) \propto \sum_{\vec{r}} -\boldsymbol{\rho}(\vec{\boldsymbol{r}})i\left(\omega_0 + \gamma\vec{\boldsymbol{G}} \cdot \vec{\boldsymbol{r}}\right)e^{-i\omega_0 t}e^{-i\gamma\vec{\boldsymbol{G}}\cdot\vec{\boldsymbol{r}}t} \qquad \ldots [2.11]$$

Now consider applying a frequency demodulation, which loosely works as follows:

ω_0 is the Larmor frequency, in the order of MHz, whereas the $\gamma\vec{\boldsymbol{G}} \cdot \vec{\boldsymbol{r}}$ contribution is in the order of kHz. Therefore, as $\omega_0 \gg \gamma\vec{\boldsymbol{G}} \cdot \vec{\boldsymbol{r}}$, the following approximation can be made:

$$\omega = \omega_0 + \gamma\vec{\boldsymbol{G}} \cdot \vec{\boldsymbol{r}} \cong \omega_0 \qquad \ldots [2.12]$$

This yields:

$$\begin{aligned} \boldsymbol{S}(t) &\propto \sum_{\vec{r}} -\boldsymbol{\rho}(\vec{\boldsymbol{r}})\left(-i\omega_0 e^{-i\omega_0 t}e^{-i\gamma\vec{\boldsymbol{G}}\cdot\vec{\boldsymbol{r}}t}\right) \\ &= -i\omega_0 e^{-i\omega_0 t}\sum_{\vec{r}} \boldsymbol{\rho}(\vec{\boldsymbol{r}})\left(e^{-i\gamma\vec{\boldsymbol{G}}\cdot\vec{\boldsymbol{r}}t}\right) \end{aligned} \qquad \ldots [2.13]$$

where the terms independent from position are rearranged to outside the summation expression. This expression can be further modified to $\gamma\vec{\boldsymbol{G}} \cdot \vec{\boldsymbol{r}}t$ by first considering $\bar{\gamma} = \gamma/2\pi$.

$$\gamma\vec{\boldsymbol{G}} \cdot \vec{\boldsymbol{r}}t = 2\pi\left(\bar{\gamma}\vec{\boldsymbol{G}}\right) \cdot \vec{\boldsymbol{r}}t \qquad \ldots [2.14]$$

Now recall the Fourier Transform Equation, and consider the expression of $\vec{\boldsymbol{k}}$:

$$\vec{\boldsymbol{k}} = \bar{\gamma}\vec{\boldsymbol{G}}t \qquad \ldots [2.15]$$

which yields:

$$2\pi\left(\bar{\gamma}\vec{\boldsymbol{G}}\right) \cdot \vec{\boldsymbol{r}}t = 2\pi\left(\bar{\gamma}\vec{\boldsymbol{G}}t\right) \cdot \vec{\boldsymbol{r}} = 2\pi\vec{\boldsymbol{k}} \cdot \vec{\boldsymbol{r}} \qquad \ldots [2.16]$$

It then follows that:

$$\boldsymbol{S}(t) = \iiint \boldsymbol{\rho}(\vec{\boldsymbol{r}}) e^{-2\pi i \vec{\boldsymbol{k}} \cdot \vec{\boldsymbol{r}}} d^3\vec{\boldsymbol{r}} \qquad \ldots [2.17]$$

which is a volume integral, or the 3D-FT of the object. So the signal acquired is the Fourier Transform of the superposition of the spins affected by the gradient field $\vec{\boldsymbol{G}}$.

It is now necessary to consider the gradient field $\vec{\mathbf{G}}$ as it changes with respect to time. For simplicity, consider a 2D gradient field from here onwards. Namely,

$$\vec{\boldsymbol{G}}(t) \cdot \vec{\boldsymbol{r}} = G_x(t)x + G_y(t)y \qquad \ldots [2.18]$$

The general equation that relates magnetic moment is the *Bloch Equation*:

$$\frac{d\vec{\boldsymbol{m}}}{dt} = -\gamma \vec{\boldsymbol{B}} \times \vec{\boldsymbol{m}} \qquad \ldots [2.19]$$

In the x, y, and z coordinate system in matrix form:

$$\begin{bmatrix} \dot{m}_x(t) \\ \dot{m}_y(t) \\ 0 \end{bmatrix} = det \begin{vmatrix} \hat{x} & \hat{y} & \hat{z} \\ 0 & 0 & -\gamma \vec{\boldsymbol{G}}(t) \cdot \vec{\boldsymbol{r}} \\ m_x & m_y & 0 \end{vmatrix} \qquad \ldots [2.20]$$

This yields a system of differential equations:

$$\begin{aligned} \dot{m}_x(t) &= \left(\gamma \vec{\boldsymbol{G}}(t) \cdot \vec{\boldsymbol{r}}\right) m_y \\ \dot{m}_y(t) &= -\left(\gamma \vec{\boldsymbol{G}}(t) \cdot \vec{\boldsymbol{r}}\right) m_x \end{aligned} \qquad \ldots [2.21]$$

Representing this in complex number form yields:

$$\dot{m}_x(t) + i\dot{m}_y(t) = -i\left(\gamma \vec{\boldsymbol{G}}(t) \cdot \vec{\boldsymbol{r}}\right)\left(m_x + i m_y\right) \qquad \ldots [2.22]$$

$$\dot{m}(t) = -i\left(\gamma\vec{\boldsymbol{G}}(t)\cdot\vec{\boldsymbol{r}}\right)m \qquad \ldots [2.23]$$

which is a simple 1st order differential equation, with the following solution:

$$\dot{m}(t) = m_0 e^{-i\int \gamma\vec{\boldsymbol{G}}(t)\cdot\vec{\boldsymbol{r}}dt} \qquad \ldots [2.24]$$

And making a similar substitution $2\pi\left(\gamma\vec{\boldsymbol{G}}t\right)\cdot\vec{\boldsymbol{r}} = 2\pi\vec{\boldsymbol{k}}\cdot\vec{\boldsymbol{r}}$ yields:

$$\vec{k}_{\boldsymbol{x}}(t) = 2\pi\gamma\int G_x(t)\,dt \qquad \ldots [2.25]$$

$$\vec{k}_{\boldsymbol{y}}(t) = 2\pi\gamma\int G_y(t)\,dt \qquad \ldots [2.26]$$

The area under the Gradient waveform will be the location in k-space sampled at time *t*.

Example: Spatially Selective Excitation

The method to introduce spectral selectivity by manipulating the RF excitation waveform has been introduced in ***2.1.2***. In this section, the addition of gradient waveform during RF waveform playout is used to demonstrate the excitation of a spatially selective slab, allowing anatomical imaging of a targeted volume.

Consider an RF pulse with a sync profile, whose Fourier spectrum is a rectangular function Π(B). In **Figure 2.2**, a trapezoidal z-gradient played out would introduce a spectral range varying linearly by position. Then, magnetization vectors within the spectral RF bandwidth Π(B), or equivalently in the spatial range exhibiting the precession frequency within the spectral bandwith, would experience resonance:

$$M_{\perp} = \begin{cases} i\gamma M_0 e^{-i\omega t} & \text{if B is within a specified bandwidth} \\ 0 & \text{otherwise.} \end{cases} \qquad \ldots [2.27]$$

A spectrally selective RF pulse can be combined with a gradient excitation to selectively excite a slice thickness.

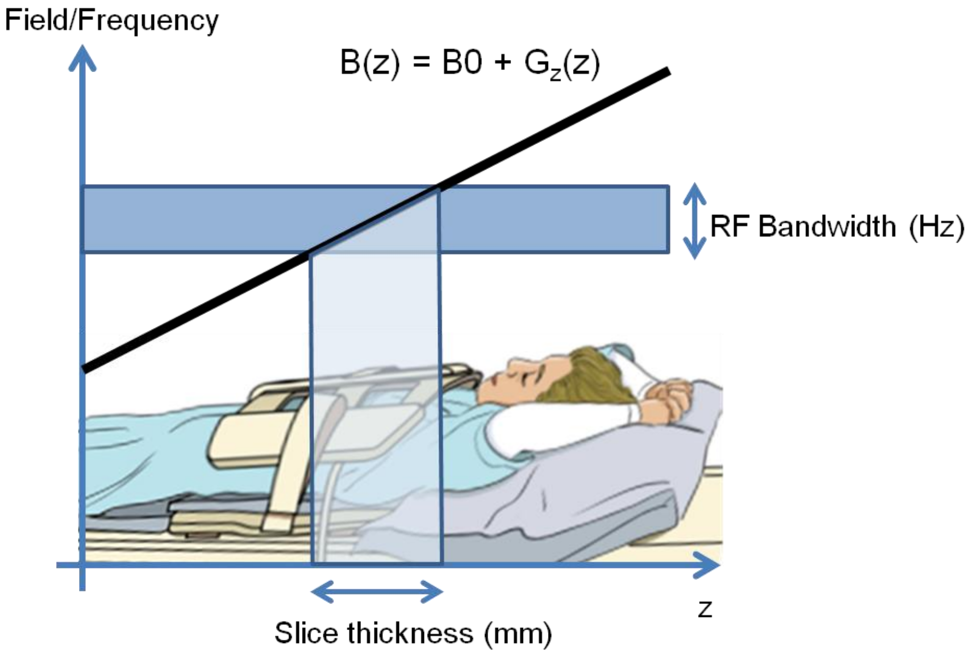

Figure 2.2 Spatially Selective Excitation.
A sync-shaped RF excitation provides a spectral RF bandwidth. A linear gradient played out during this RF pulse duration introduces a slice-encoding effect onto the RF spectral range that is excited, which results in exciting a specific volume, for targeted anatomical imaging with MRI. Illustration by Robert Zubkoff: Courtesy of www.learnmri.org.

2.1.4 Receiver Coil - Signal Reception

The signal equation from the Faraday’s Law of Induction is as follows:

$$\text{flux} = \Phi_{\mathrm{B}} = \iint \vec{\mathbf{B}}(\vec{\mathbf{r}}) \cdot \mathrm{d}\mathbf{A} \qquad \ldots [2.28]$$

in which the magnetic flux, Φ_{B}, is equal to the integral of the magnetic field through its surface. In this equation, d**A** is the element of the surface area across the receiver coil. The induced electromotive force EMF, is the change in flux:

$$EMF \propto -\frac{d\Phi_{\mathrm{B}}}{dt} \qquad \ldots [2.29]$$

In this equation, EMF is also proportional to the number of wire loops in the receiver coil. Furthermore, each net magnetization vector has a contribution of:

$$-\frac{d\Phi_{\mathrm{B}}}{dt} \propto \omega m_{\perp 0} e^{-i\omega t} \qquad \ldots [2.30]$$

Thus the total signal observed by a coil, or the sum of EMF, can be expressed using the ***principle of superposition***:

$$S(t) \propto \sum_{\vec{r}} \rho(\vec{r})\left(\omega m_{\perp} e^{-i\omega t}\right) \qquad \ldots [2.31]$$

Signal sampling must also be considered upon the examination of the receiver coil. A fundamental concept in sampling theory is the Nyquist Theorem, which states that the maximum frequency that can be sampled must be less than half the sampling frequency. In practice, the maximum frequency sampled is about a tenth of the sampling rate, which holds true in MRI acquisition as well. In medical imaging, insufficient sampling of the resonant frequencies would result in aliasing artifacts. Many literature are available on the sampling theory, and dedicated research to undersample the acquisition while being able to reconstruct a high-quality image has gained interest (10-13). Namely, accelerated imaging techniques using parallel imaging, compressed sensing, or a combination of the two, have emerged over the last 15 years. These methods utilize unique strategies to undersample the k-space and reconstruct an image to yield anatomically accurate images at the cost of a slightly reduced SNR.

2.1.5 The TPS Chassis – Scanner Hardware Control

On the General Electric MRI scanner hardware platform (GE Excite), the components described in 2.1.1 – 2.1.4 are controlled by a dedicated system known as the transceiver processor and storage (TPS) or alternatively as multi-generation data acquisition (MGD) chassis in the more recent hardware versions, which manipulates all scanner hardware including the RF, gradients, and signal acquisition. The MGD has a 4 µsec precision in the synchronous generation of different waveforms, as well as the signal acquisition. As demonstrated in ***2.1.3*** to show an example of spatially selective excitation, the manipulation of these waveforms allows virtually an infinitely possible ways to both spatially and spectrally excite, as well as acquire spatially encoded frequency responses, with realistic limitations due to sampling, safety, as well as clinical constraints for routine MR application on the patient population.

Dedicated MRI pulse sequences can be designed and used to acquire a wide variety of anatomical images with different contrasts, or be applied in combination with post processing methods beyond a simple 2D or 3D Fourier transformation to extract functional information about tissue and blood characteristics (ie. phase-contrast (14), T1 and T2 mapping, DTI, QSM, etc.), as well as magnetization-prepared methods (eg. DIR (15), T2IR (16), etc.) to extract specific clinically relevant information. Carefully timed acquisition of k-space signal would enable temporally dynamic reconstructions (ie. perfusion, cine, and navigators), which allows more than a simple anatomical imaging volume reconstruction that may be applied to clinical manner for examination of diseases that cannot be diagnosed from static images. These novel methods beyond a simple 2D or 3D Fourier transformation of a k-space data are often handled in post-processing. While many of the described techniques require dedicated post-processing, a fundamental aspect of MR imaging volume reconstruction utilizes a multidimensional Fourier transform to convert the spatially encoded k-space signal into an anatomical image.

2.1.6 GE EPIC - Pulse Sequence Design

Pulse sequence software development on the GE's scanner platform is performed using a software environment called EPIC (which stands for Environment for Pulse programming In C). In the 14M5 software version used for the majority of the work in this thesis, the compilation of the MRI pulse sequence in EPIC produces two executable files: the first is the PSD host process that runs on the host console and communicates with the entire scanner system, and the second is the PSD target process (known as IPG in previous software versions) that performs dedicated control of scanner hardware.

In the host process, a set of predefined variables called *Control Variables*, or CV, are used to communicate with the remaining part of the scanner system. The host process runs during setup of the scan and has four subroutines. All CVs are initialized in the *cvinit* section. Once initialized, their values are continually updated after any operator action during setup in the *cveval* section. In the *cvcheck* section, all CVs are verified so that relevant scan parameters remain within the hardware and software constraints. Finally, the *predownload* section executes once more before the entire set of CVs are sent to the target for pulse generation through the download process.

The download process commences the target process, which transfers the set of CVs from the host onto the scanner hardware. The target component includes two notable subroutines: the waveform generation known as *PulseGen* (PG), and the *Real-time Sequence Preparation* (RSP) that runs during the scan with the hardware sequencers that control the TPS. PG is the section where each set of pulse is generated, and is individually saved into memory blocks that can be easily accessed during RSP. In the research environment, CVs can be forced to a fixed value specified by the operator after the download process. The target component hence plays a significant role in the timing and manipulation of the waveforms.

The RSP section specifies the sequential order of all waveforms that are to be played out. For a majority of MRI scans, the acquisition scheme of the scan is predetermined; real-time imaging discussed in **2.2.3** and **Chapter 5** requires additional feedback from a separate piece of software that runs concurrently with the RSP section of the pulse sequence. Another notable constraint in the pulse sequence development is the resource allocated for waveforms that can be saved; there is a limit on the number of RF excitation pulses that can be archived per scan, as well as the number of waveforms (which is a combination of RF, gradient, and readout) that can be called back in the RSP. Pulse sequence development on the GE platform must also account for these constraints.

2.1.7 Volume Reconstruction and Analysis – Image Post-Processing

For volumetric image reconstruction stored after the end of an MRI scan, a 2D k-space raw data is applied the 2D Fourier transformation into the image domain. Likewise, a 3D k-space raw volume data is applied a Fourier transform in 3D.

While the k-space data acquired using the Cartesian scheme can be readily processed by the VRE board as soon as the data acquisition completes, it is more involved to reconstruct images from sampling methods that are either non-Cartesian (eg. spiral, radial, etc.) or inherently undersampled and require a specific reconstruction scheme, including parallel imaging methods such as SENSE, SMASH, and compressed sensing. These methods often require additional dedicated post-processing, using a dedicated hardware such as an offline workstation, server cluster, or more recently a graphical processing unit (GPU) for rapid processing of raw data into an image or a format with clinically diagnostic utility while the clinician is on the scanner.

Additionally, MR technology is not limited to a static imaging volume or functional analysis. Manipulation of k-space acquisition over the scan duration allows reconstruction of temporally dynamic images, as well as reconstructions whose primary utility is not in the reconstructed volume, but rather in the functional parameters that can be readily extracted from the specific post-processing methods (eg. left ventricular myocardial motion and volume filling analysis from cine-CMR sequences, flow velocity measurements from Phase Contrast sequences, motion information from myocardial tagging methods, fiber tracking with Diffusion Tensor Imaging, hemodynamic response with BOLD fMRI sequences, etc).

One clinical application of image post-processing described in Chapter 3 is the automated segmentation of left ventricle from short-axis cine SSFP images. This technique, which can be used readily on clinically acquired cine-CMR short axis images of the LV, utilizes a region-growth algorithm on the left ventricular chamber using an operator-defined seed point across a slice range, and monitors the effusion of the region growth to leak to the outside of the myocardium. The algorithm detects a significant change in the segmented volume upon this leakage, which is then used to retract and identify the left ventricular volume. This approach can be used iteratively on multiple slices and temporal phases in a cine-SSFP image to fully segment the entire left ventricular volume, and the volume filling profiles can be further assessed to identify physiological abnormalities of the heart. Likewise, myocardial volume can be segmented using an analogous algorithm, which allows a clinical evaluation of myocardial performance.

Manipulation of MRI pulse sequences and the development of corresponding post-processing and clinical evaluation methods enable a tremendous number of ways for MRI to diagnose diseased states, and in some cases provide guided intervention in the therapeutics. In the most recent annual meeting of the International Society of Magnetic Resonance and Medicine (ISMRM) held in Melbourne, Australia in May of 2012, there were approximately 4500 research abstracts presented in over 120 different clinical, technical, and a handful of educational categories, which suggests significant interest in active and ongoing MRI research.

2.2 The MR System Architecture

The previous section, **2.1** loosely referred to different hardware components and their primary roles in the MR system. Additionally, the work presented in Chapter 5 of this thesis makes use of a unique MR hardware and a software system to enable a novel MR data acquisition technique. Additional modifications to the storage mechanism of the acquired MR signal, or additional instructions can be sent to the scanner hardware and enable novel reconstruction methods. This section provides an overview of both the typical hardware architecture on the General Electric (GE) Excite scanner platform described within the general common sense. Two examples are provided; the first is the use of a dedicated cluster for volume reconstruction of signals sampled with a non-Cartesian spiral trajectory, and the second is the real-time processing of navigator data for prospective acquisition to minimize scan time. Of note, the latter provides the prerequisite background for the real-time and interactive software system introduced in Chapter 5.

2.2.1 The GE EXCITE System Architecture

Figure 2.3 shows the block diagram of the GE EXCITE system architecture. In order to enable real-time MR processing during data acquisition, the system must rapidly process and communicate between different components without encountering any run-time errors while also allowing operator control of the real-time software during a scan.

Fast and real-time MR signal processing is performed on the Multi-Generation Data Acquisition (MGD) Chassis, specifically on the acquisition processing subsystem (APS) board that coordinates MR data acquisition. Allowing the real-time processing on the APS board during an MRI scan allows rapid access, processing, and communication via instructional packets with the host computer which controls the graphics shown on the console, and the application gateway processor (AGP) board which coordinates with dedicated hardware to create the RF and Gradient waveforms, which is also on the MGD.

The GE EXCITE systems used in this research employ the Reflex 400 Vector Array Processor (AP) board, which allows up to 2GB of acquired signal storage into the Bulk Access Memory (BAM). This amount of memory is typically sufficient for storage of one 3D k-space volume. Each data point is stored into the BAM as a pair of real and imaginary 2-byte signed short numbers. Thus an eight-channel cardiac array with a fully sampled k-space dimension of 256 x 256 x 16 requires approximately 33 MB for storing the entire k-space data. A typical MRI scan can be stored into the BAM without reaching close to its size constraints. However, BAM size constraints can potentially be highly oversampled dynamical scans; for example, if assuming a TR of 4 msec in sampling each line with 256 sampling points using an 8 channel coil, it would be possible to continuously acquire data for ~17 minutes before the BAM becomes completely filled.

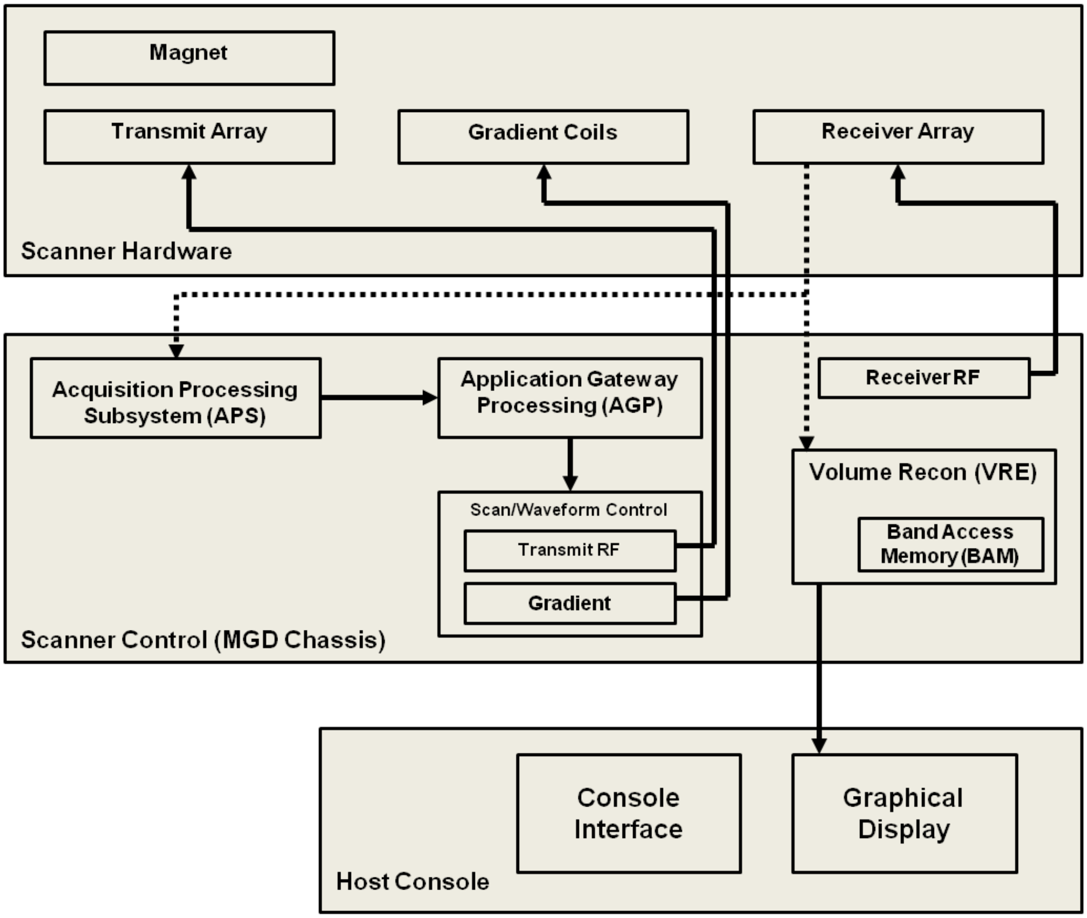

Figure 2.3 A Typical MRI System Architecture Block Diagram.
The system architecture is organized in three sections; the scanner hardware, the scanner control, and the host console.

2.2.2 Example – 3D Spiral Phase Resolved Reconstruction

The 3D Spiral Cine method demonstrates an example of how non-Cartesian sampling can be combined with a dedicated and elaborate reconstruction that uses sliding window view sharing, non-Cartesian spiral reconstruction, and anti-aliasing of spiral artifacts by PILS. On the GE system, dedicated acquisition trajectories such as spiral can be processed seamlessly with a dedicated image reconstruction on the data stored in the BAM. This is enabled by specifying the CV *rhrecon* to a value corresponding to the reconstruction code one seeks to perform. **Figure 2.4** shows the workflow of a dedicated reconstruction of a 3D SSFP cine spiral sequence that is exclusively developed by Kressler *et al* (17,18) on the GE platform. This example is noteworthy because the specific *rhrecon* calls a script to sort the acquired spiral k-space data, pushing it to multiple nodes in a computer cluster accounting for shared views, where each node then generates a 3D k-space volume at a specific phase through the standard non-Cartesian spiral reconstruction, and finally applies a fast and efficient parallel imaging scheme known as coil-specific PILS, which utilizes coil sensitivity information from a calibration scan to weigh down regions sufficiently far from each coil's sensitivity region, which thereby reduces spiral-induced aliasing artifacts in the imaging FOV.

The computation time required for image reconstruction is an important consideration, as clinical applications often require immediate feedback for the operator or clinician to further guide their scan protocols (ie. placing new prescription, or rescanning motion-artifact corrupted volumes). Kressler et al's method is reported to reconstruct the entire cine volume in under 2 minutes onto the scanner console (17), which makes the technique practical for clinical imaging.

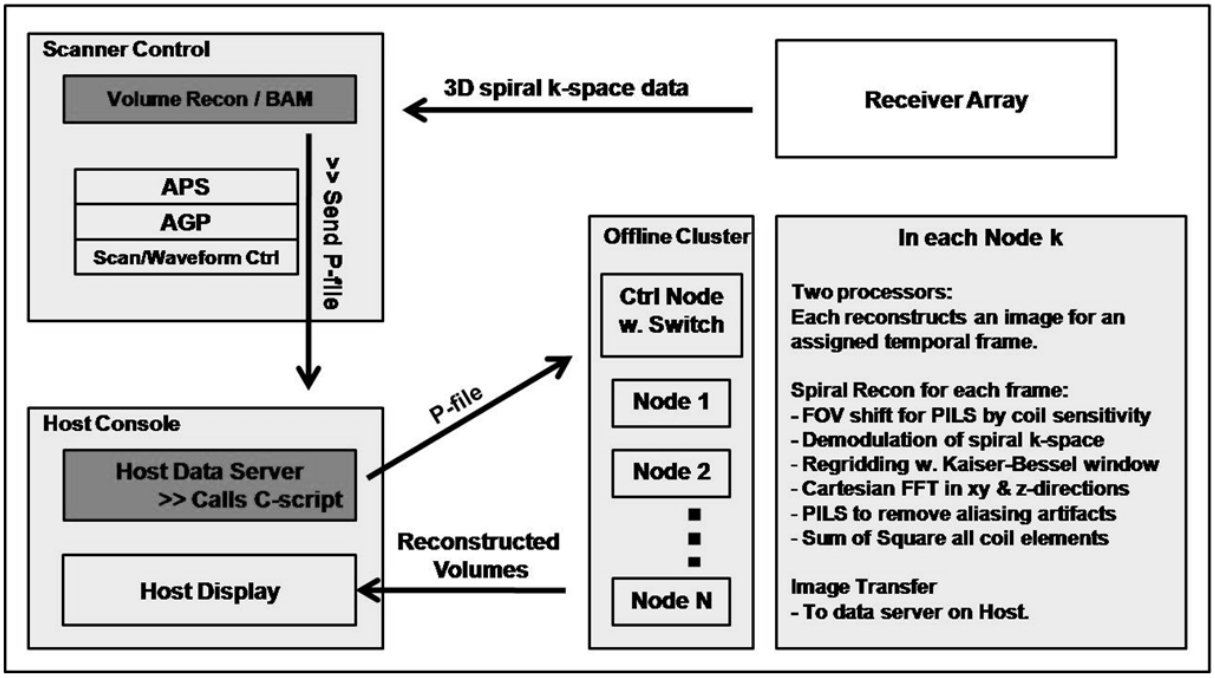

Figure 2.4 Schematics of 3D Cine Spiral Reconstruction by Kressler et al.
This reconstruction utilizes a dedicated N-node cluster (N = 32 in Kressler et al's implementation) to parallelize the spiral reconstruction of multiple volumes. Each node includes two processors each performing an assigned reconstruction task, allowing the reconstruction of all cine images in less than 2 minutes for a 40-fold scan time reduction.

In a general sense, allowing the *rhrecon* to run a computationally inefficient MATLAB-based script on the volume reconstruction hardware is expected to perform the slowest. This can be improved by either running the same MATLAB script on a dedicated server with more powerful hardware capabilities, or alternatively running the reconstruction script using a more high-level programming language such as C or C++. Additionally, parallel post-processing of different volume slices or temporal phase on a multi-node cluster can further speed up the total computation to return the clinically relevant information to the scanner console. More recently, there has been great interest in utilizing a dedicated GPU for nontrivial reconstruction algorithms, and some vendor platforms, such as SIEMENS, have recently introduced a GPU-based reconstruction unit on their most recent scanner products.

2.2.3 Example –Prospectively Gated Coronary MRA

In **2.1.6**, a brief introduction was given to the idea of establishing a communication line in real-time to direct the views to acquire during the scan. For real-time imaging, the interaction between the RSP section, any external software component for real-time data processing, and the entire MRI scanner architecture as a whole must be thoroughly considered to effectively enable real-time imaging on the scanner hardware.

Previous GE Excite system's infrastructures have allocated the navigator signal directly onto the BAM, which has been sufficient for extracting and processing a single echo, but has constrained the development of more elaborate real-time data processing, such as prospective navigator gating. Recent modifications in the software/hardware infrastructure which redirects the acquired navigator echoes into a separate buffer for immediate access the acquired echo has enabled more elaborate real-time MR processing and applications, such as the technique presented in Chapter 5 of this thesis, and that given in ref. (19) by Spincemaille et al, which preceded the real-time processing of 2D navigator image is based on.

The real-time front end of the system is designed using the X-window protocol, which allows graphical manipulation and display necessary for real-time applications without constraining the resource-dependent real-time APS hardware. Software variables on the APS are also created on the host side to replicate the processing environment, and a communication between components using VxWorks (Wind River Systems Inc., Alameda, CA), a real-time operating system (RTOS) for embedded system processing in real-time, to update the APS with modified parameters from the host in a secure and reliable manner.

Performing PAWS gating...

HB Count 151

View Count 30

10 245 10

Figure 2.5 Prospective Diaphragmatic Pencil-beam Navigator Gating Interface. 1D pencil-beam is being displayed over multiple heartbeats in this X-window based graphical display that updates every heartbeat and adjusts the data acquisition with a real-time feedback loop to the scanner based on the current respiratory position and previously acquired data using the PAWS prospective gating algorithm. A more detailed description of PAWS gating algorithm is provided in **5.3.3.**

Figure 2.5 shows the existing real-time interface for processing a 1D pencil-beam prescribed on the diaphragm-liver interface for prospective gating with Phase ordering with Automatic Window Selection (PAWS) (20). The pencil-beam data is first extracted from its storage and applied a 1D Fast Fourier Transform, which depicts the liver-diaphragm position as a sharp contrast between the liver tissue with signal and the air inside the lung with no signal. This information can then be used with a variety of existing prospective gating algorithms, including accept/reject, diminishing variance, PAWS, or CLAWS.

2.3 Summary

MRI is an extremely versatile platform for clinical imaging with a wide variety of anatomical and functional applications. This chapter provided an overview of how the MRI scanner hardware, software, and the overall system architecture can enable a variety of imaging methods to identify clinically relevant information to assist diagnostics and advance medicine. Novel imaging technologies are constantly being developed, and diagnostic methods to aid these methods are becoming more prevalent. Cardiac and peripheral magnetic resonance imaging applications discussed in the remaining chapters form a small but important part of the overall technology development in magnetic resonance research.

Chapter 3

LV DIASTOLIC ASSESSMENT

3.1 Clinical Background

Left ventricular (LV) diastolic dysfunction is a common cause of heart failure, occurring in up to 40-50% of heart failure patients (21,22). Identification of diastolic dysfunction is important for assessment of prognosis and tailoring of therapy. Altered LV compliance changes the timing profiles of LV filling and leads to diastolic dysfunction. LV filling profiles have been used to assess diastolic function by other imaging modalities, such as radionuclide cineangiography (RNCA) (23-25). Similar applications for cardiac magnetic resonance (CMR) imaging have been impractical as manual planimetry of all LV images across all temporal phases would typically require tracing of over two hundred images per patient. Thus, whereas CMR is an accepted reference standard for LV systolic function, its use for assessment of diastolic function is limited and additional testing, such as echocardiography (echo) is typically employed to establish this diagnosis.

Automated segmentation of isolated end-diastolic and end-systolic phases is well-established for measurement of LV ejection fraction (26-28). By extension, automated segmentation of LV volumes across all temporal phases holds the potential to rapidly assess diastolic filling patterns. An advantage of this approach is its application to standard cine-CMR data without additional dedicated imaging, which can be prohibitive in heart failure patients with limited breath hold capabilities. While automated segmentation holds the potential to markedly increase the yield of standard CMR exams, its utility for distinguishing between normal and abnormal diastolic filling has not been validated.

An automated segmentation algorithm (LV-METRIC) was recently developed to quantifies LV volume based on per-voxel signal intensity while employing no assumptions regarding LV shape (28). In an initial validation study, LV-METRIC closely agreed with phantom volumes and LV ejection fraction as manually measured in clinical patients (28). The current study was designed to evaluate whether volumetric filling profiles generated automatically by LV-METRIC can be useful to distinguish between patients with and without isolated diastolic dysfunction as established by the reference standard of echo.

3.2 Experimental Design

This study included consecutive patients with normal LV systolic function (EF ≥ 55% on echo and cine-CMR) who underwent echo assessment of diastolic function within 7 days of CMR. The study was conducted in accordance with the Institutional Review Board (IRB) at Weill Cornell, which approved the research protocol. All prospectively enrolled patients provided written informed consent and the IRB approved use of pre-existing clinical data.

Comprehensive clinical data were collected at the time of CMR including cardiac risk factors, coronary artery disease (CAD) history, NYHA functional class, and medication regimen. Self-reported data were supplemented by review of medical records for assessment of casual blood pressure measurement, invasive filling pressures, and clinical indices.

3.3 Imaging Protocol

In this study, echocardiography was used as a gold standard in the assessment of diastolic function. As described in 3.2, the study limited its population to patients who underwent echo and CMR within 7 days. Three patients were excluded whose CMR data prohibited qualitative assessment of LV performance due to atrial fibrillation or ventricular ectopy. No patients were excluded based on clinical characteristics or quantitative processing results. Imaging was performed between September 2005 and April 2009 at Weill Cornell Medical College.

3.3.1. Echocardiography

Transthoracic echoes were performed using commercially available equipment (General Electric Vivid-7 or Siemens Sequoia). Images were acquired in apical and parasternal orientations and linear quantitative measurements were performed on parasternal views in accordance with American Society of Echocardiography guidelines (29). Mitral valve inflow parameters were acquired in an apical 4 chamber view via pulsed-wave Doppler sampling performed at the mitral valve leaflet tips perpendicular to the valve annulus. Tissue Doppler profiles were acquired in the apical 4 chamber view with sampling performed at the basal septum and, if technically feasible, lateral wall.

The echo diagnosis of diastolic dysfunction was adjudicated in all cases by a single experienced echocardiographer (RBD) who was blinded to patient identity and CMR results. In accordance with established guidelines (30,31), diastolic performance was graded as follows:

- ***Normal:*** E/A ≥0.8, septal e’ ≥8, lateral e’ ≥10, deceleration time 140-240 msec
- *Grade 1(mild)*: E/A <0.8, septal e’ <8, lateral e’ <10, deceleration time >240 msec
- *Grade 2 (moderate)*: E/A 0.8-1.5, septal e’ <8, lateral e’ <10, develeration time 140-240 msec
- *Grade 3 (severe)*: E/A ≥2, septal e’ <8, lateral e’ <10, deceleration time <140

In patients with equivocal tissue Doppler indices (i.e. abnormal lateral but normal septal e’ amplitude), e’/a’ reversal (<1) and pulmonary vein flow profiles were used to establish presence of diastolic dysfunction.

3.3.2. CMR Imaging

CMR exams were performed using 1.5 Tesla scanners (General Electric). Cine-CMR used a commercially available 2D steady state free precession pulse sequence. Images were acquired in contiguous short axis slices from the level of the mitral valve annulus through the LV apex. Typical parameters were as follows: repetition time (TR) 3.5 msec, echo time (TE) 1.6 msec, flip angle 60°, in-plane spatial resolution 1.9 mm x 1.4 mm, slice thickness 6mm, inter-slice gap 4mm. Mean reconstructed temporal resolution (RR interval/# cardiac phases) was 36 ± 10 msec and absolute temporal resolution (TR x views per segment) was 75 ± 17 msec.

3.4 Automated Segmentation of the Left Ventricle

Automated segmentation of isolated end-diastolic and end-systolic phases is well-established for measurement of LV ejection fraction. By extension, automated segmentation of LV volumes across all temporal phases holds the potential to rapidly assess diastolic filling patterns. An advantage of this automated approach is its application to standard cine-CMR data without additional dedicated imaging, which can be prohibitive in heart failure patients with limited breath hold capabilities. While automated segmentation holds the potential to markedly increase the diagnostic yield of standard CMR exams, its utility for distinguishing between normal and abnormal diastolic filling has not been validated.

An automated segmentation algorithm that quantifies LV volume based on per-voxel signal intensity and employs no assumptions regarding LV shape can be used to generate LV volumetric filling curves. One such algorithm, LV-METRIC was used in this study.

3.4.1 LV-METRIC Algorithm for Full-Volume Segmentation

The full-volume implementation of LV-METRIC region-growth is as follows (32):

1. A seed point for the first cine SSFP image is set manually on the LV cavity.
2. LV region grows iteratively with successively lower thresholds until breaching myocardium and effusion.
3. Myocardial breaching point allows determination of myocardial signal intensity (SI) for precise LV-myocardial border detection.

4. Seed points for adjacent/successive cine SSFP images are estimated by looking for a point close to the current segmentation's center-of-mass with similar SI to blood. Steps 2 and 3 are repeated for segmentation of successive images.
5. The automation is stopped when all images in a matrix are segmented.

For all segmentations, user input included indentification of the slice range to be segmented and definition of the valve annulus. Optional user corrections were provided by manually contouring to restrict region-growth and by adjusting blood sensitivity.

This algorithm automatically segments the endocardial border excluding papillary and trabecular structures from the blood volume for assessment of chamber volumes. Epicardial segmentation was also performed for automated quantification of LV mass (33).

3.4.2 Parameter Measurements

End-diastolic volume (EDV) and end systolic chamber volume (ESV) were calculated using Simpson's method and EF was calculated as EF = [EDV-ESV]/EDV *100. Basal and apical image positions were defined in accordance with previously reported criteria, with the basal LV defined by the basal most image encompassing at least 50% circumferential myocardium (34). LV mass was quantified based on automated border detection of end-diastolic endocardial and epicardial contours (33), with mass determined as the product of myocardial volume and specific gravity ([EpiEDV-EDV]*1.05).

3.5 Diastolic Function Assessment

3.5.1 Filling Curve Analysis

For the assessment of diastolic function, LV-METRIC segmentation for each short axis slice was performed across all temporal phases. **Figure 3.1** shows a typical example of the segmented images. Volumetric data were transferred into an automated processing tool developed in MATLAB (MathWorks Inc, Natick, MA) to analyze the LV volume-filling time course. To assess LV filling profiles, the basal and apical LV image positions were defined as the locations in which at least 50% LV myocardium was present during systole and diastole. The following CMR diastolic parameters were evaluated:

- *Peak Filling Rate* [PFR] - maximal LV filling rate defined by maximal change in LV volume between sequential temporal phases (Δ volume/Δ phase); This index was also adjusted for stroke volume to generate *Normalized Peak Filling Rate* [NPFR]
- *Time to Peak Filling Rate* [TPFR] - time interval between end-systole and peak filling rate
- *Diastolic Volume Recovery* [DVR] - proportion of diastole required for recovery of a given percentage (i.e. 80%) of stroke volume

The volumetric filling curve was also transformed to the first derivative in order to obtain early (E) and late (A) filling profiles, similar to a typical mitral inflow pattern. Representative graphic illustrations of each parameter in relation to LV-METRIC generated filling profiles are provided in **Figure 3.2**.

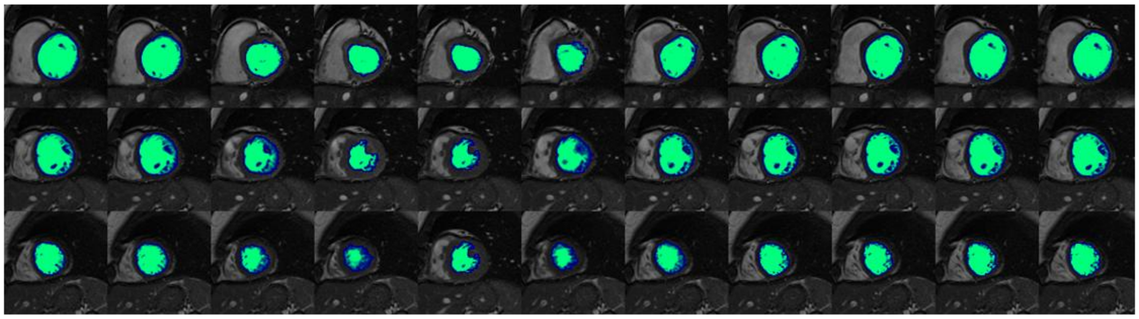

Figure 3.1 A Typical Example of Segmented Left Ventricle Images.
Automated LV-METRIC segmentation of representative time points within basal, mid, and apical slice locations (note that all slice locations and temporal phases segmented for diagnostic purposes). Segmentation was performed across spatial (vertical) and temporal (horizontal) domains for volumetric assessment of LV diastology.

3.5.2 Statistical Methods

Comparisons between groups with or without diastolic dysfunction were made using Student's t test for continuous variables (expressed as mean ± standard deviation and/or median, interquartile range [IQR]). Categorical variables were compared using Chi-square or, when fewer than 5 expected outcomes per cell, Fisher's exact test. Overall diagnostic test performance was evaluated using receiver operator characteristics (ROC) curves, with comparison between ROC curves performed using a univariate z score test of the difference between the partial areas under the two performance curves between specificities of 80% and 100% , a clinically relevant range of specificity for assessment of diastolic dysfunction. Test sensitivity was compared using McNemar?s test for paired proportions. Logistic regression analyses and bivariate correlation coefficients were employed to evaluate associations between

CMR and echo parameters. Two-sided $p < 0.05$ was considered indicative of statistical significance. Statistical calculations were performed using SPSS 12.0 (SPSS Inc, Chicago, IL).

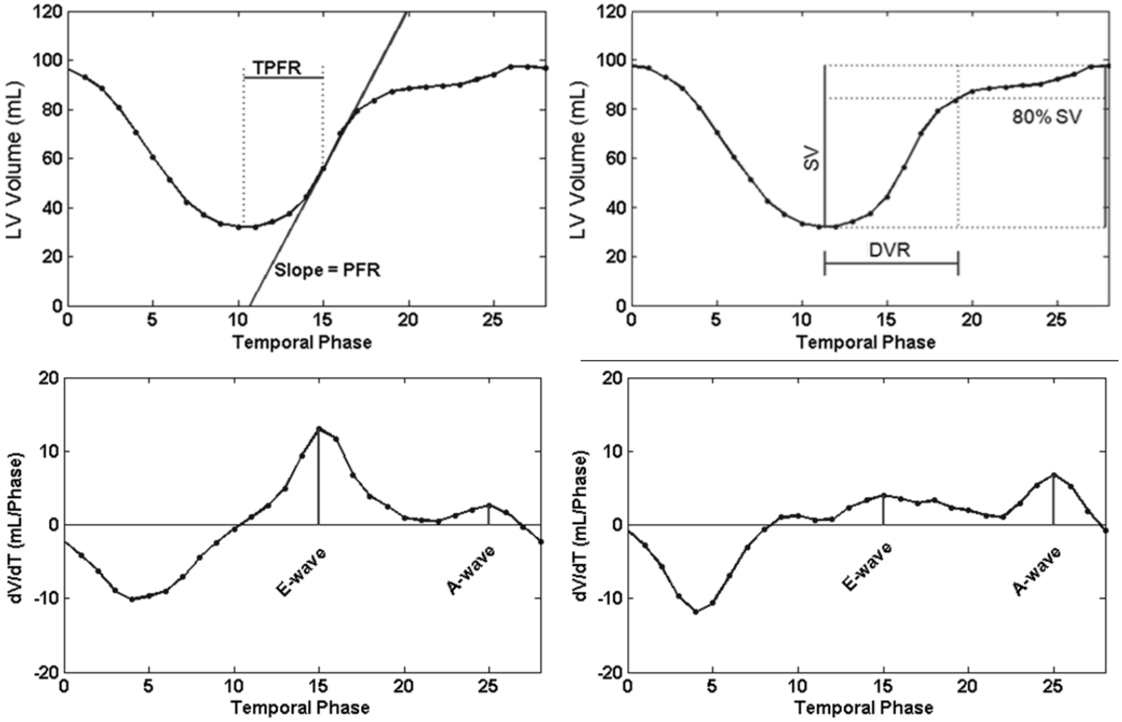

Figure 3.2 Volume Filling Profiles.

(Top) Representative LV filling curves (x-axis=temporal phase, y-axis=volumetric change). Peak filling rate (PFR), defined as maximal slope of Δvolume/Δ temporal phase, and time to peak filling rate (TPFR) are shown on the left-sided graph. Diastolic volume recovery (DVR), calculated as proportion of diastole necessary to recover a threshold of 80% LV stroke volume, is shown on the right-sided graph.

(Bottom) Typical examples of normal (left) and abnormal (right) inflow patterns generated by first derivative transformation of the volumetric filling curve. Note E:A reversal in association with diastolic dysfunction.

3.6 Results

3.6.1 Population characteristics

The study population consisted of 101 patients who underwent CMR and echo within 7 days of one another (mean interval 1.4±2.1 days). 50 patients had echo-evidenced diastolic dysfunction. When classified according to severity, diastolic dysfunction was mild (grade 1) in 38% (n=19), moderate (grade 2) in 60% (n=30), and severe (grade 3) in 2% (n=1) of affected patients.

As shown in **Table 3.1**, patients with echo-evidenced diastolic dysfunction were older, were more likely to have clinically diagnosed hypertension, and had higher clinically-measured systolic blood pressure than those without diastolic dysfunction ($p<0.001$). Left atrial volume and MR severity did not differ significantly between groups; 96% of patients had MR graded as less than or equal to mild severity by echo. Both echo and cine-CMR demonstrated higher LV mass among patients with diastolic dysfunction ($p<0.001$), despite generally smaller measurements by CMR compared to echo (Δ LV mass 27±20gm/m^2, $p<0.001$).

Table 3.1 Population Characteristics.

	Overall	**Normal Diastolic Filling† (n=51)**	**Diastolic Dysfunction† (n=50)**	P
CLINICAL				
Age (year)	51±18	41±14	62±14	**<0.001**
Male gender	59%	55% (28)	64% (32)	0.35
Blood Pressure				
Systolic blood pressure (mm Hg)	124±18	116±12	132±19	**<0.001**
Diastolic blood pressure (mm Hg)	70±11	70±10	71±11	0.59
Heart Rate	69±11	70±11	69±11	0.80
Atherosclerosis Risk Factors				
Hypertension	45%	16% (8)	74% (37)	**<0.001**
Diabetes Mellitus	20%	10% (5)	30% (15)	**0.01**
Hypercholesterolemia	39%	29% (15)	48% (24)	0.06*
Tobacco Use	7%	4% (2)	10% (5)	0.27
Family History	40%	35% (18)	44% (22)	0.37
Coronary Artery Disease	35%	28% (14)	42% (21)	0.12
Prior Myocardial Infarction	27%	24% (12)	30% (15)	0.51
Prior Coronary Revascularization	28%	24% (12)	32% (16)	0.34
NYHA Functional Class *(I/II/III/IV)*	79/12/9/1	44/6/1/-	35/6/8/1	0.06*
Dyspnea	24%	75% (18)	25% (6)	**0.004**
Medications				
Beta-blocker	51%	35% (18)	66% (33)	**0.002**
ACE-Inhibitor/Angiotensin Receptor Blocker	38%	26% (13)	50% (25)	**0.01**
Thiazide diuretic	11%	2% (1)	20% (10)	**0.004**
Loop diuretic	9%	4% (2)	14% (7)	0.09*
Calcium channel blocker	4%	2% (1)	6% (3)	**0.36**
HMG CoA-Reductase Inhibitor	45%	35% (18)	54% (27)	**0.06***
Aspirin	50%	31% (16)	68% (34)	**<0.001**
ECHOCARDIOGRAPHY				
LV Morphology				
End-diastolic diameter (cm)	5.2±0.6	5.2±0.6	5.3±0.6	0.41
End-systolic diameter (cm)	3.4±0.5	3.4±0.5	3.4±0.5	0.83
Anteroseptal wall thickness (cm)	1.0±0.2	0.9±0.1	1.0±0.3	**0.006**
Posterolateral wall thickness (cm)	0.9±0.1	0.9±0.1	1.0±0.1	**0.002**
Relative wall thickness	0.30±.13	0.27±.13	0.33±0.13	**0.03**
Myocardial mass (gm/m^2)	92±22	85±15	101±25	**<0.001**
LV Systolic Function				
Ejection fraction (%)	63±6	63±6	64±6	0.42
Fractional shortening (%)	35±5	34±5	35±5	0.69
LV Diastolic Function				
Deceleration Time (msec)	211±61	192±41	235±74	**0.002**
Mitral Inflow E/A Ratio	1.3±0.5	1.5±0.4	1.1±0.5	**<0.001**
Tissue Doppler e′ (septal)	8±4	11±3	6±2	**<0.001**
Tissue Doppler e′ (lateral)	11±5	15±3	8±2	**<0.001**
Tissue Doppler E/e′ †	11±8	7±3	15±10	**<0.001**
Tissue Doppler e′/a′ †	1.1±0.6	1.5±0.5	0.7±0.2	**<0.001**
Mitral Regurgitation (0-4 severity scale)	0.7±0.3	0.6±0.2	0.7±0.4	0.71
CARDIAC MAGNETIC RESONANCE				
LV Systolic Function				
Ejection fraction (%)	66±7	63±6	68±8	**0.001**
Stroke Volume (ml)	84±23	84±21	84±24	0.95

LV Morphology				
End-diastolic volume (ml)	127±33	132±31	123±36	0.20
End-systolic volume (ml)	44±15	48±14	39±15	**0.003**
Myocardial mass (gm/m^2)	67±18	60±13	74±20	**<0.001**
Left Atrial Volume (ml/m^2)	47±17	45±11	48±20	0.51

Boldface type = $p < 0.05$ * $p < 0.1$ † calculated using average of septal and lateral e’

3.6.2 CMR Diastolic Parameters

LV-METRIC successfully generated LV volumetric filling profiles in all patients; Mean processing time was 2:04 ± 0:53 minutes, which included time for automated segmentation, visual review of the segmented data, and any manual corrections. In 48% of patients, LV segmentation required only manual delineation of the LV outflow tract and apical borders. Additional manual corrections of LV-METRIC contours were necessary in the remainder of the population (3±4 corrections per exam, 1.4% [288/20,584] of all images).

Table 3.2 reports CMR diastolic parameters for patients stratified according to diastolic filling classified by echo. As shown, patients with echo-evidenced diastolic dysfunction had longer normalized peak filling rate and absolute time to peak filling (both $p<0.001$) than those without diastolic dysfunction. Diastolic dysfunction was also characterized by higher DVR ($p<0.001$), calculated as the proportion of diastole required for LV recovery of 80% stroke volume. Among all CMR diastolic indices tested, only DVR was significantly correlated with echo-evidenced deceleration time ($r=0.29$, $p <0.01$).

Table 3.2 Cardiac Magnetic Resonance Diastolic Parameters.

	Overall	**Normal Diastolic Filling***	**Diastolic Dysfunction***	P
E:A wave (peak amplitudes)	2.2±1.5	3.1±1.6	1.6±1.1	**<0.001**
Peak Filling Rate (ml/sec)	286±90	301±79	272±99	0.11
Normalized Peak Filling Rate (stroke vol. adjusted)	3.5±0.9	3.6±0.8	3.3±0.9	**0.04**
Time to Peak Filling Rate (msec)	194±122	160±77	229±149	**0.005**
Diastolic Volume Recovery (80% stroke volume)	70±15	60±14	79±9	**<0.001**

Boldface type indicates p value < 0.05
*** Diastolic categories assigned using an echo standard**

Derivative transformation of the volumetric curves yielded distinct E and A waves in 76% of the population (**Figure 3.2 bottom rows**), with absence of discernable E and A waves in the remainder. CMR-generated E:A filling ratios differed between patients with and without diastolic dysfunction, with lower absolute E:A ratio in the diastolic dysfunction group ($p<0.001$). When E:A ratios were categorized using a binary threshold of 1, there was moderate agreement between CMR and echo (kappa .50, $p<0.001$), although the two modalities were discordant in 16% (12/76) of patients.

3.6.3 Diagnostic Performance of CMR Parameters

Figure 3.3 provides receiver operating characteristics (ROC) curves for CMR-derived diastolic variables. As shown, DVR yielded improved overall performance as compared to both PFR and TPFR based on total area under the ROC curve ($p<0.001$ for both comparisons). Among all diastolic time intervals, DVR yielded the best diagnostic performance using a threshold of 80% of LV stroke volume (AUC 0.87), with slightly worse performance achieved when thresholds between 50-90% of stroke volume were tested (AUC 0.75 – 0.86).

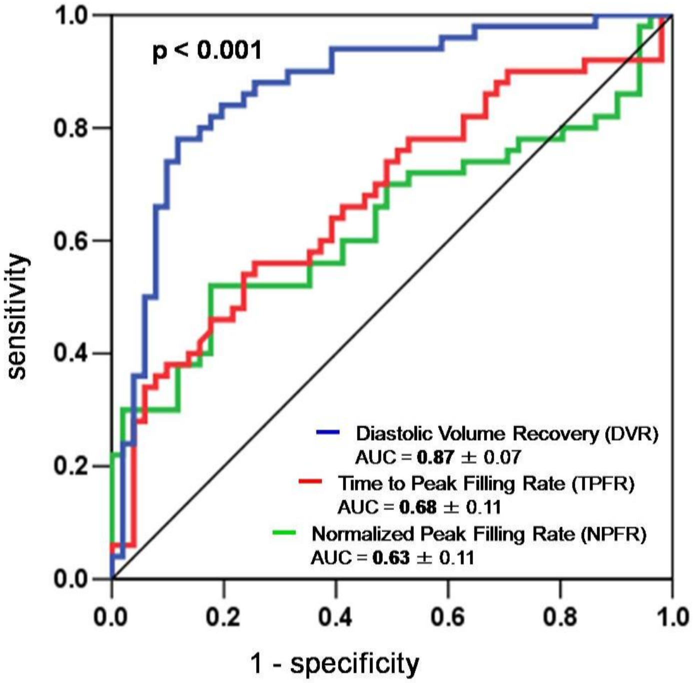

Figure 3.3 Receiver Operating Characteristics Curves.
Among all CMR indices tested, DVR yielded optimal diagnostic performance as evidenced by highest area under the curve (p<0.001 vs. NPFR and TPFR respectively).

Table 3.3 reports sensitivity, positive, and negative predictive value of all CMR diastolic indices as calculated based on a matched specificity cutoff (90%). As shown, sensitivity of DVR (74%) was approximately two fold greater than either TPFR (38%) or NPFR (30%) (both p<0.001). Among the 13 (26%) patients with echo-evidenced diastolic dysfunction that were missed by CMR-evidenced DVR, 4 had mild, 8 moderate, and 1 severe grade diastolic dysfunction. In the one patient with severe (grade 3) diastolic dysfunction, DVR was classified as normal whereas PFR was classified as abnormally low (based on the 90% specificity cutoff), suggesting that this latter parameter may be useful for identifying restrictive filling.

Table 3.3 Diagnostic Performance of CMR Diastolic Indices*

	Threshold	Sensitivity	**Specificity**	**Positive Predictive Value**	**Negative Predictive Value**
Normalized Peak Filling Rate	2.81	30% (15/50) †	90% (46/51)	75% (15/20)	57% (46/81)
Time to Peak Filling Rate	192 msec	38% (19/50) †	90% (46/51)	79% (19/24)	60% (46/77)
Diastolic Volume Recovery	77% of diastole	74% (37/50)	90% (46/51)	88% (37/42)	78% (46/59)

*** Diagnostic performance calculated using a threshold to acheive 90% specificity.**
† p <0.001 vs. DVR

3.6.4 Clinical and Hemodynamic Associations

CMR diastolic parameters differed significantly when patients were grouped based on clinical status. **Figure 3.4 (Left)** reports the prevalence of CMR-evidenced diastolic dysfunction (based on abnormal PFR or DVR) among patients stratified by NYHA functional class; Prevalence of diastolic dysfunction (using cutoffs in **Table 3.3**) was increased in relation to severity of functional impairment and was greater among patients with NYHA class III or IV (80%) compared to those with class II (58%) or class I (40%) functional status (p=0.04). When grouped according to binary presence or absence of clinical dyspnea (**Figure 3.4 Right**), there was nearly a two-fold greater prevalence of CMR-evidenced diastolic dysfunction (PFR or DVR) among symptomatic versus asymptomatic patients (p=0.006). A similar relationship was evident when prevalence of abnormal DVR alone was compared between patients grouped by dyspnea status (63% vs. 39%, p=0.02).

CMR diastolic parameters also stratified groups based on invasive filling pressures. Among the subgroup of the population (n=22) that underwent CMR and invasive angiography within a narrow interval (mean 1.5±1.2 days, range 0-3 days), patients with abnormal PFR (based on **Table 3.3** cutoffs) had higher LV end-diastolic filling pressures than those with normal PFR (32±14 vs. 18±6 mmHg, p < 0.01). A similar trend was demonstrated when LV end-diastolic filling pressures were compared between patients stratified based on DVR (22±10 vs 15±4 mmHg, p=0.08).

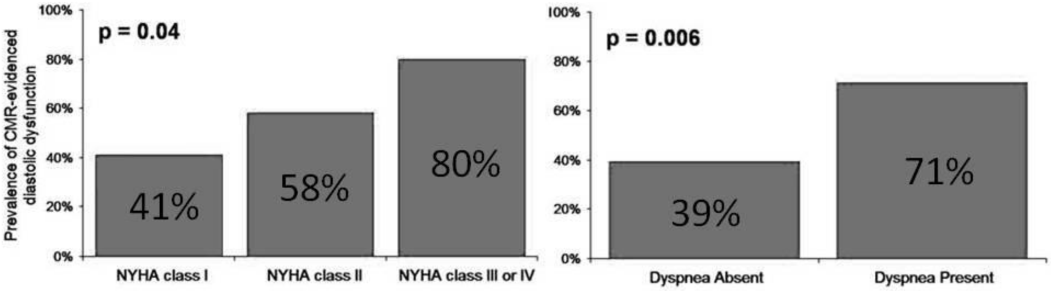

Figure 3.4 Prevalence of Abnormal Diastolic Filling in Relation to Clinical Status. Prevalence of CMR-evidenced diastolic dysfunction was increased among patients with clinically evidenced heart failure as stratified by either NYHA functional class (left) or binary presence/absence of dyspnea (right).

3.6.5 Predictors of Diastolic Function

Clinical and imaging parameters were examined to determine whether CMR diastolic indices yielded incremental value after controlling for standard predictors of diastolic dysfunction. As shown in **Table 3.4**, logistic regression analyses demonstrated that DVR was an independent predictor of echo diastolic dysfunction even after controlling for age, clinically diagnosed hypertension, and CMR-quantified left ventricular mass. The relationship between DVR and diastolic dysfunction was continuous, with over a 75% increase in relative risk for diastolic dysfunction conferred by every 10 percentage point increment in DVR. **Table 3.4** substitutes echo-evidenced LV mass in the multivariate model, demonstrating that the relationship between DVR and diastolic dysfunction was independent of the modality used to measure LV hypertrophy.

Table 3.4 Multivariate Predictors of Echo-Evidenced Diastolic Dysfunction.

4A. CMR LV Mass: Model $\chi^2 = 73.4$, $p<0.001$

Variable	Odds Ratio	95% Confidence Interval	P
Age	1.05	0.99 – 1.11	0.17
Hypertension	4.42	1.24 – 15.71	**0.02**
LV Mass (gm/m^2)*	1.71	1.21 – 2.23	**0.005**
Diastolic Volume Recovery †	1.82	1.13 – 2.57	**0.02**

4B. Echocardiography LV Mass: Model $\chi^2 = 53.0$, $p<0.001$

Variable	Odds Ratio	95% Confidence Interval	P
Age	1.04	0.98 – 1.10	0.21
Hypertension	3.70	1.10 – 12.44	**0.04**
LV Mass (gm/m2)*	1.26	0.87 - 1.65	0.18
Diastolic Volume Recovery †	1.71	1.07 – 2.39	**0.03**

* Per 10 gm/m2 increment

† Per 10 percent increment

3.7 Discussion

This study provides several new observations concerning automated CMR assessment of LV diastolic function: First, automated CMR processing was robust, providing LV filling profiles in all patients tested within an average time of approximately 2 minutes. Filling curves were generated using standard cine-CMR images that were not tailored for diastolic assessment. Second, among a diverse population with normal systolic function, CMR-evidenced diastolic filling parameters generally stratified between patients with and those without echo-evidenced diastolic dysfunction. Prevalence of abnormal CMR diastolic filling parameters increased in relation to clinical heart failure status as classified based on NYHA functional class or the binary presence or absence of dyspnea. Third, CMR-evidenced diastolic filling (DVR) was an independent predictor of echo-evidenced diastolic dysfunction even after controlling for clinical and imaging variables such as hypertension and LV mass. Automated segmentation is important for assessment of LV filling because cavity volumes must be measured on hundreds of short-axis cine images, making manual tracing impractical for widespread clinical application. In prior validation studies, LV-METRIC reduced processing time by >90% versus manual tracing and closely agreed with both phantom volumes and clinical patient data (28). The LV-METRIC algorithm relies on two simple assumptions – (1) signal intensity of blood differs from that of myocardium, and (2) LV blood is surrounded by myocardium. This approach differs from other automated segmentation algorithms, which have typically employed elegant but restrictive assumptions regarding LV shape or contour deformation (26,27). LV-METRIC does not use geometric assumptions and can thereby accommodate differences in LV shape and remodeling patterns among patients with diastolic dysfunction.

The results here demonstrate that decreased peak filling rates (stroke volume normalized) and prolonged time to peak filling can be used to identify patients with diastolic dysfunction. These findings are in general agreement with prior studies that have used RNCA (23,25,35) or single-photon emission computed tomography (36) to evaluate LV filling profiles. Moreover, although differences between modalities prohibit volumetric comparisons for absolute peak filling rates, mean normative values for time to peak filling rate for the CMR results (157 msec) were similar to prior values published for RNCA (172-198 msec) (25,35) and single-photon emission computed tomography (165 msec) (36). Unlike nuclear imaging, CMR involves no radiation exposure and is thereby well suited for population-based screening and serial imaging of patients with diastolic dysfunction to evaluate response to targeted therapies. Additionally, because CMR provides high spatial-resolution imaging, it enables study of other indices that are associated with impaired diastolic performance but not typically imaged by nuclear techniques, including myocardial mass, left atrial size, and pericardial thickness.

In addition to absolute peak filling rate and time required to achieve peak filling, this paper reports a new index – diastolic volumetric recovery time (DVR) – that can be used to assess diastolic function. The findings here demonstrate that this simple parameter, which accounts for variance in heart rate and stroke volume, had excellent diagnostic performance as evidenced by ROC analysis (AUC = 0.87), with superior overall performance to either NPFR or TPFR ($p<0.001$). As DVR is a measure of the proportion of diastole required for recovery of a given fraction of stroke volume, it accounts for per-patient differences in heart rate and volume status, which can affect peak filling rate (23,37). Consistent with the findings here that DVR provides incremental value compared to PFR, prior studies using radionuclide imaging have reported that peak filling rate is affected by loading conditions whereas proportional filling (i.e. filling fraction completed during the first half of diastole) is load independent (38). The findings here that an optimal diagnostic threshold for DVRT is 80% suggests that this parameter reflects LV filling prior to atrial contraction; Prior studies using invasive hemodynamic measurements have shown that in normal controls, approximately 80% (79±7%) of LV stroke volume occurs during active early diastolic LV relaxation and subsequent diastasis (39).

Prior CMR studies have used dedicated imaging techniques to assess LV diastolic dysfunction. Prior studies have demonstrated that phase contrast imaging can be used to demonstrate mitral and pulmonary vein inflow patterns as a means of distinguishing between patients with and without diastolic dysfunction (40,41). Other investigations have used phase contrast imaging to identify regional myocardial tissue profiles in a manner analogous to tissue Doppler imaging (42). Myocardial tagging can also be used to evaluate regional myocardial torsion and diastolic strain rate (43). These approaches require additional imaging for dedicated assessment of diastolic function, which can be technically challenging, increase exam duration, prolong processing time, and prohibitive for patients with limited breath-hold capabilities.

While this study used a dedicated automated segmentation algorithm for assessment of diastologic parameters, the data were obtained from a standard, commercially available, steady state free precession cine-CMR sequence that required no additional imaging beyond that which is commonly applied to assess LV systolic function. To demonstrate the feasibility of this approach, the diagnostic performance was tested among pre-existing exams that were not requested or tailored for assessment of diastolic function. Consistent with this study's approach, CMR assessment of LV filling curves has been shown to be feasible in smaller studies (44-47); Maciera et al (46) used an automated method (CMR Tools) to study normal distributions of LV peak filling rates (PFR) and time to peak filling rates (TPFR) among patients without known risk factors or history of cardiovascular disease. However, as this prior study was limited to normal controls, the utility of CMR to identify diastolic dysfunction was not tested. This study evaluated diagnostic performance of automated CMR segmentation among patients with and without diastolic dysfunction by echo, which is well accepted as a diagnostic standard for assessment of LV diastology (30).

In addition to assessment of diastolic performance based on cavity volumes, LV-METRIC can also employ an automated algorithm to measure myocardial mass (33). This feature is not necessary to generate LV filling curves. However, it provides adjunctive data regarding myocardial hypertrophy, which can contribute to diastolic dysfunction. In this study, LV mass by CMR was significantly lower than echo derived mass. While this may be due to limitations of the automated algorithm used to quantify mass, an alternative explanation relates to methodological differences; Mass by CMR was obtained from 3D delineation of endo/epicardial contours whereas echo-derived mass was derived using a 1D linear formula that incorporates assumptions regarding LV geometry. Prior studies have shown that volumetric mass by CMR yields lower values than does linear-derived mass by echo (48,49) and that magnitude of difference between modalities is greatest in patients with LV remodeling (50).

It is important to recognize that although LV filling profiles add to the information obtained from routine CMR exams, approximately one fourth of patients with echo-evidenced diastolic dysfunction were not identified by CMR indices. There are several potential explanations for discordance between CMR and echo. First, while the interval between tests was short (1.4±2.1 days), diastolic performance can rapidly change due to alterations in LV loading conditions, and it is possible that performance varied during the narrow interval between tests. Second, due to its high temporal resolution, echo may detect subtle manifestations of diastolic dysfunction that are not evidenced by lower temporal resolution imaging by routine cine-CMR. Third, although tissue Doppler is a common criterion for diastolic dysfunction, it can be influenced by regional abnormalities that may not alter global diastolic filling as measured by cine-CMR. Although our study compared CMR filling parameters with echo-Doppler, use of echo as an absolute reference standard is a limitation, given debate regarding how echo patterns of diastolic dysfunction should be interpreted with respect to their clinical context (30,31). However, echo is widely used to assess diastolic performance and consensus guidelines (30), which were used in this study, offer one means to standardize interpretation of echo-evidenced diastolic filling patterns.

Several additional limitations should be acknowledged. Although results demonstrate that LV filling profiles generated by automated processing of routine cine-CMR can be useful to assess the binary presence or absence of echo-evidenced diastolic dysfunction, the utility of CMR for assessing graded severity of diastolic dysfunction was not tested. Additionally, although CMR diastolic parameters were associated with higher LV filling pressures in a subgroup that underwent angiography, CMR was not compared with invasive hemodynamics in the majority of subjects. Finally, data are lacking concerning the prognostic implications of CMR-evidenced diastolic dysfunction and the correlation between CMR diastolic parameters and serological indices such as brain natriuretic peptide.

In summary, this study demonstrates that automated CMR segmentation can generate LV filling profiles that may offer insight into diastolic dysfunction. Prolongation of diastolic filling on cine-CMR is associated with echo-evidenced diastolic dysfunction independent of other clinical and imaging variables. Future research is warranted to assess whether automated CMR assessment of diastolic filling can be used to grade severity of diastolic dysfunction, assess invasive filling pressures, or predict clinical outcomes.

Chapter 4

3D BLACK-BLOOD PERIPHERAL VESSEL WALL IMAGING

4.1 Clinical Background

Vessel wall imaging is essential for accurate assessment of atherosclerosis, aneurysms and vasculitis. Clinically established imaging modalities include ultrasound, computerized tomography, and MRI. High-resolution MRI of the arterial vessel wall has the advantage of characterizing atherosclerotic plaque morphology and composition noninvasively without ionizing radiation. However, MRI requires effective blood suppression to improve the contrast between the artery lumen and the surrounding vessel wall.

Conventional black-blood MRI techniques rely on the inflow of magnetization prepared upstream blood into the imaging volume, such as double inversion recovery (DIR) (15) and spatial presaturation (SPSAT) (51), and are mainly suited for 2D imaging. However, 3D imaging is often desired because it can provide thinner slices and higher signal-to-noise ratio (SNR) than 2D imaging. To address the need for effective blood suppression within a large 3D imaging volume have been developed, including flow-dependent motion sensitizing magnetization preparation (MSPREP) (52-54), which dephases the flowing blood signal using velocity-encoding gradients prior to imaging, and flow-independent T2-prepared inversion recovery (T2IR) (55,56), which exploits the difference in T1 and T2 relaxation times between blood and vessel wall to provide global blood suppression regardless of blood flow velocity and direction.

While black-blood imaging of the aorta (52,53,55,57), coronary (58,59) and carotid arteries (55,60,61), and the heart (15,54,55) has been widely demonstrated, black-blood imaging of the lower extremity vasculature has received less interest (62,63) due to several unique challenges including much slower blood flow, particularly in diseased vessels (64), and the need for much larger coverage compared to other vascular territories. Recent work has demonstrated that stagnant blood flow may induce plaque mimicking intraluminal artifacts in 2D DIR fast spin echo (FSE) images of the lower extremity vessel walls (56). Flow-independent T2IR prepared 2D FSE of the femoral and popliteal artery wall has been shown to be robust against slow flow artifacts, although this technique suffers from low SNR and long scan time. Two studies, which built on top of prior works with 2D T2IR-prepared FSE (56) are conducted: the first demonstrates the feasibility of 3D T2IR-prepared SSFP for large volume vessel wall imaging, and compares its blood suppression performance with the three alternative preparations (65). The second study developed a high-resolution vessel wall imaging using both T2IR prepared SSFP and FSE sequences (66).

4.1.1 Magnetization Prep Comparison

In the first study, the feasibility of an SNR efficient 3D flow-independent T2IR balanced steady-state free precession (SSFP) vessel wall imaging sequence is first shown, and is then compared against flow-dependent DIR, SPSAT and MSPREP magnetization preparations for blood suppression and vessel wall visualization in the popliteal artery.

4.1.2 Submillimeter and Isotropic Popliteal Vessel Wall Imaging

In the second study, a 3D T2IR sequence for high-resolution vessel wall imaging sequence is developed, allowing the acquisition of large coronal volumes with submillimeter isotropic resolution in a fixed scan duration and without ECG gating. Data acquisition is optimized for both FSE and SSFP sampling strategies at 1.5T, and their performance is compared by measuring the muscle and lumen SNR, as well as the muscle-to-lumen CNR.

4.2 Black-Blood Mechanisms

4.2.1 T2-Prepared Inversion Recovery (T2IR)

T2IR is a hybrid magnetization preparation that combines two well-known preparations, T2prep and inversion recovery to provide contrast between tissues with similar T1 but different T2 relaxation times. It was initially developed for applications in MR Angiography, in order to provide contrast between luminal signal and the surrounding vasculature. For black-blood imaging, difference in T1 and T2 relaxation times between blood and vessel wall is exploited to provide global blood suppression regardless of flow velocity and direction. **Figure 4.1** provides an illustrative explanation.

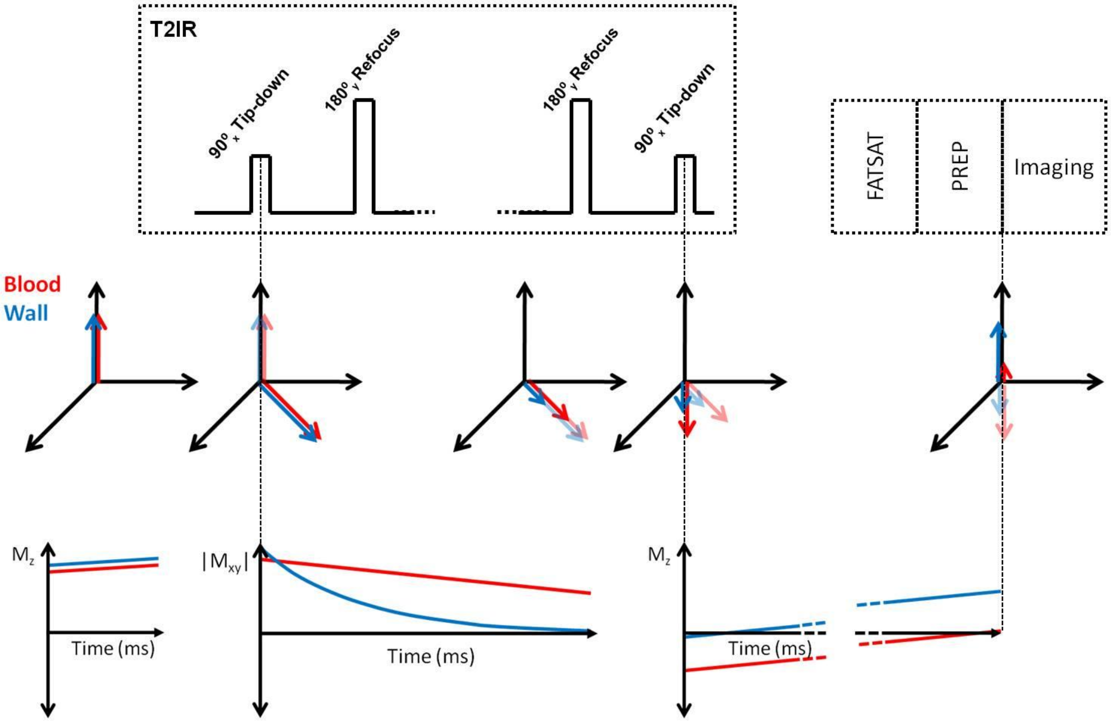

Figure 4.1 Mechanism of T2IR Black-Blood Magnetization Preparation.
T2IR black-blood preparation utilizes a 90° tip-down pulse to flip the magnetization from the longitudinal axis onto the transverse $|M_{xy}|$ plane. After a tissue-specific T2 decay is applied for a duration, T2prep time, another 90° tip-down pulse is played out to further tip down the magnetization onto the –z longitudinal axis. The second tip-down is a combination of the 90° tip-up puse from T2Prep, and a 180° inversion pulse. After an inversion time, TI, imaging commences when the longitudinal magnetization vector from the blood signal crosses the zero nulling point.

4.2.2 Alternative Black-Blood Suppression Mechanisms

Conventional inflow-based black blood techniques include double inversion recovery (DIR) (15,67) and spatial presaturation (SPSAT) (51,68) of upstream blood, but these methods are suited for 2D imaging. Several 3D methods have been developed, including flow-independent T2IR, and flow-dependent motion-sensitizing magnetization preparation

(MSPREP) (52,53,69) which dephases the flowing blood signal using velocity-encoding gradients prior to imaging. These alternative blood suppression magnetization preparations are considered for comparison in this study.

4.2.3 DIR preparation

DIR utilizes two inversion pulses; a 180° hard inversion pulse, followed immediately by a 180° spatially selective re-inversion pulse to restore the magnetization within the imaging volume. The first hard pulse applies a global inversion including the magnetization of upstream blood that will eventually flow into the imaging volume, which is inverted back by the second pulse to the equilibrium position. The inversion time (TI) is chosen so that the inflowing blood signal’s longitudinal magnetization crosses zero, at which readout phase encodes are played out to acquire images with nulled blood signal for black-blood imaging.

4.2.4 SPSAT preparation

Similar to DIR, SPSAT is also an inflow-based blood suppression method, which utilizes a spatially selective excitation pulse prescribed immediately superior to the imaging volume to saturate the upstream blood. A flip angle slightly larger than 90° is followed by spoiler gradients to provide dephasing of the upstream blood signal prior to image acquisition. Unlike DIR, no additional delay is played out between the SPSAT preparation and SSFP imaging.

4.2.5 MSPREP

The MSPREP black-blood mechanism works by providing a large velocity encoding gradient to provide an intravoxel dephasing. An MSPREP magnetization preparation pulse consists of 90° tip-down, 180° refocusing, and 90° tip-up nonselective RF pulses and a pair of velocity encoding gradients positioned around the 180° pulse to dephase blood spins based on their velocities. In this study, a pair of identical unipolar gradients were used. The gradient area can be manipulated to control the degree of dephasing, and this property is characterized by field of speed (FOS), or first-order gradient moment, m1.

4.3 Scout Scan Design

In each 2D black-blood scout scan used in the comparison study, several images were acquired sequentially while the pertinent black-blood imaging parameter was automatically varied over a range of values. The black-blood imaging parameters were inversion time (TI) for DIR (range 275-450 msec) and T2IR (175-350 msec), field of speed (FOS) in the through-plane direction for MSPREP (1-5 cm/sec), and saturation flip angle for SPSAT (90 º -120º) The optimal parameter was identified by visually selecting the 2D black-blood scout image with the best black blood contrast. **Figure 4.1** shows examples of the images from the 2D scout scan for selection of the optimal parameter.

The 2D black-blood SSFP scout scan imaging parameters were as follows: TR = 4.2 msec, TE = 1.7 msec, flip angle = 60º, receiver bandwidth = ±83.3 kHz, axial field of view (FOV) =

18 cm, matrix = 256x256 interpolated to 512x512, slice thickness = 12 mm, number of excitations (NEX) = 1 (DIR, SPSAT) and 2 (MSPREP, T2IR), views per segment (VPS) = 64, centric view order, scan time ~1 min (DIR, SPSAT, MSPREP) and 1.5 min (T2IR) at a nominal heart rate of 60 beats per minute (bpm). The 2D black-blood scout scans were prescribed at the middle of the 3D imaging volume.

For the high-resolution imaging study, experiment setup was performed by first acquiring a one-minute 2D multislice Fast Gradient Echo sequence to estimate the most anterior and posterior position of the femoral and popliteal arteries for image planning of the coronal volume prescription. For T2IR-SSFP parameter optimization, the same scout scan method was used as the comparison study. T2IR-FSE was optimized using a built-in method in the PSD based on the pulse sequence parameters, however, validation was performed by acquiring a set of three low-resolution coronal volume scout scan at TI = 300 msec, at the automatically optimized TI = 353 msec, and at TI = 400 msec. If the blood signal was lower at either extremal TI values, an additional TI was played out 25 msec below 300 msec, or above 400 msec. Each low-resolution scout scan took 2 minutes to complete.

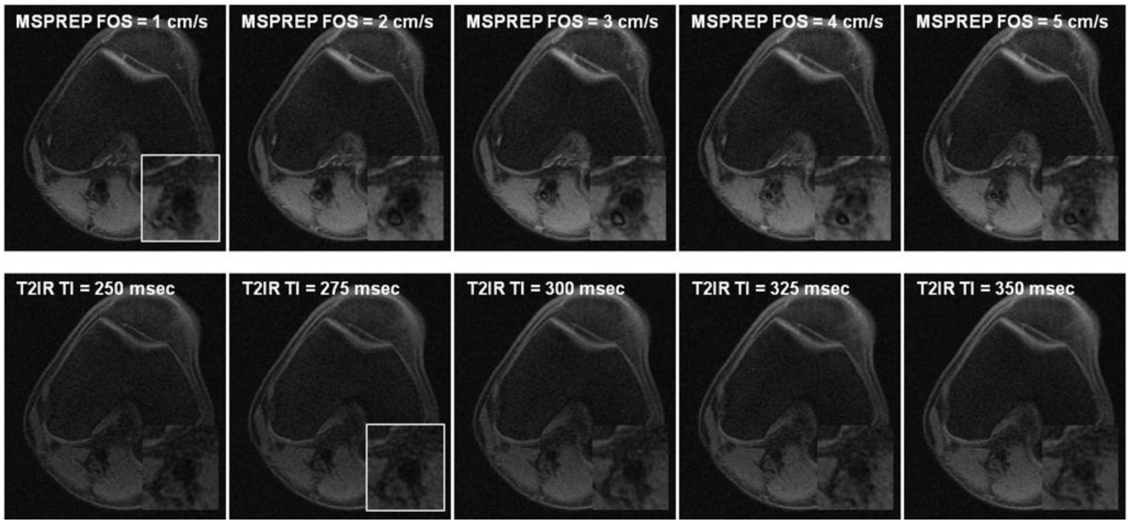

Figure 4.2 Scout Scan for identifying optimal black-blood parameters.
Black-blood parameters were varied by linear increments, and the operator selected the parameters corresponding to the image best suppression of lumen signal without degradation in vessel wall visualization. ROI measurements are performed on the scanner console using a dedicated viewing software for each set of scout scan images. Above shows examples of MSPREP (top row), and T2IR (bottom row) from one volunteer, highlighting the optimal image.

4.4 3D Black-Blood Imaging Sequence

4.4.1 Black-Blood Mechanism Comparison

For the comparison study, SSFP readout is used, as it provides bright blood contrast and thus permits objective comparison of the four black-blood techniques without interference from inherent black-blood image contrast such as in FSE. Additionally, each black-blood magnetization preparation was performed every heartbeat and immediately after the peripheral trigger—typically corresponding to the period of maximum arterial blood flow in the popliteal artery—to enhance blood suppression of the flow-based DIR, SPSAT, and MSPREP techniques. **Figure 4.3** shows the schematics of the implemented cardiac-triggered segmented-k-space 3D SSFP vessel wall MRI sequences.

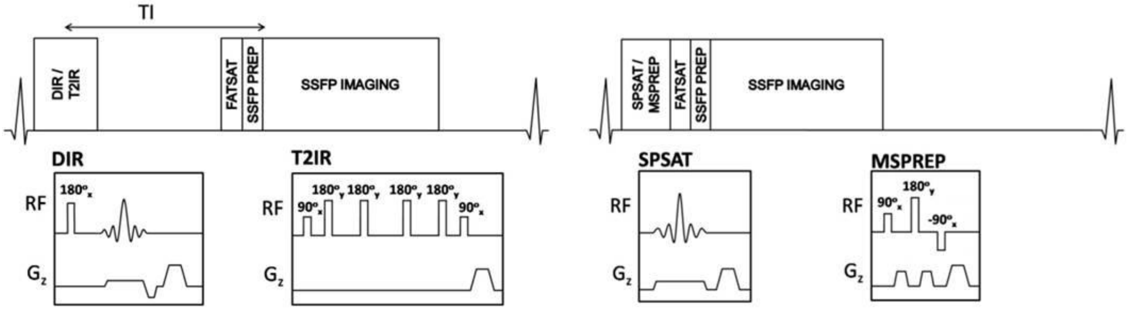

Figure 4.3 Schematic of the Peripheral Triggered 3D black-blood SSFP sequences. The four black-blood preparations were played out either immediately (in SPSAT and MSPREP) or after a time delay (DIR and T2IR). A spectrally selective fat saturation pulse (FATSAT) suppressed the lipid signal and 6 Kaiser-Bessel ramped "dummy" RF pulses (SSFP PREP) prepared the magnetization prior to segmented k-space SSFP data acquisition. The sequence is repeated every heartbeat until data was fully collected.

3D black-blood SSFP imaging: TR = 3.8 msec, TE = 1.5 msec, flip angle = 60°, receiver bandwidth = ±83.3kHz, axial FOV = 18cm, matrix = 256x256 interpolated to 512x512, slice thickness = 3 mm interpolated to 1.5 mm, number of slices = 28 interpolated to 56, NEX = 2, VPS = 64, centric view order, scan time ~4 min at a nominal heart rate of 60 bpm, spectrally selective fat saturation pulse to suppress the lipid signal. 2D PC scan: TR = 8.6 msec, TE = 3.7 msec, flip angle = 25°, receiver bandwidth = ±31.25 kHz, axial FOV = 18 cm, matrix = 256x256, slice thickness = 8 mm, velocity encoding (VENC) = 50-75 cm/sec, VPS = 4, 28 reconstructed cardiac phases. The axial 3D imaging volume was prescribed to cover the distal femoral artery and the proximal popliteal artery of the right leg.

4.4.2. High Resolution Imaging Study

The schematics for the high-resolution coronal T2IR prepared 3D black-blood imaging sequence is shown below in **Figure 4.4**.

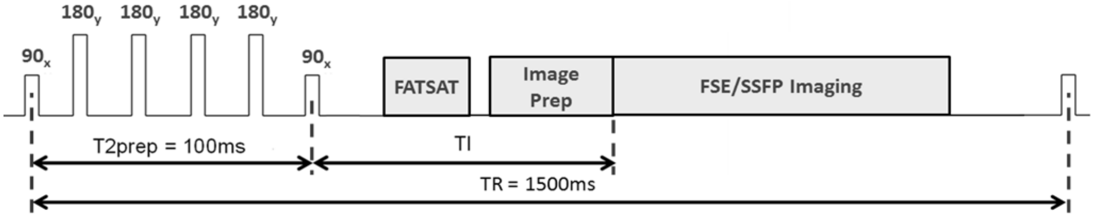

Figure 4.4 Ungated 3D T2IR-SSFP and FSE sequences.
T2IR SSFP and FSE sequences were performed without trigger, and had a fixed scan time of 12 minutes and 48 seconds.

This sequence employed an ungated acquisition method without any triggering with a fixed TR = 1500 msec and T2prep time = 100 msec. Inversion time TI was selected using the 2D scout scan. The 3D black-blood SSFP sequence parameters were the same as those described in **4.5.1**, excluding the coronal 3D volume and matrix size (20x20x5.1cm; 256x256x64 interpolated to 512x512x128), the receiver bandwidth = ±62.5 kHz. With both SSFP and FSE, 32 echoes were acquired per TR. For the T2IR-FSE sequence, the following parameters were used:

A 3-plane scout scan followed by a low-resolution 20-second 2D multi-slice axial FGRE scout scan were used for localization of the 3D imaging volume. The FGRE scout scan had the following parameters: TR = 4.9 msec, TE = 1.3 msec, flip angle = 30, matrix = 256x256, slice thickness = 10 mm, slice gap = 15 mm.

In order to keep the same number of views in each segmented k-space sequence for SSFP and FSE, the problem of T2 decay in large-view FSE acquisitions was addressed by implementing extended echo train by prescribing variable flip-angles (VFA) (70,71) , which minimized signal decay during the readout. Compared to a prior study, VFA has substantially reduced the scan time of the T2IR-FSE sequence, which was previously limited to 2D imaging without VFA to 3D imaging of a large volume in a comparable scan time.

The 2D scout scan parameters were also kept mostly the same as those reported in 4.5.1. The ±rBW was set to 62.5 kHz likewise to the 3D imaging.

4.5 Experimental Setup

4.5.1 Human Imaging Experiment

Two experiments were performed. For the comparison study between different preparations, a total of eleven healthy subjects (8 male, mean age = 28 ± 5 years, 24-39 years) were imaged. For the high resolution imaging protocol with FSE and SSFP, 11 additional subjects were imaged (8 male, mean age = 27 ± 5 years, 24-39 years). Both imaging experiments were performed on a 1.5 T scanner (HDxt, GE Healthcare, Waukesha, WI), and both study protocols were approved by the local institutional review board and a written informed consent was obtained from all subjects prior to imaging.

For the comparison protocol, subjects were imaged in a supine position using a product eight-channel cardiac phased array and peripheral gating for cardiac synchronization. For the high resolution imaging protocol, subjects were imaged in a supine position using a product eight-channel knee array. In both studies, the right knee was imaged on all volunteers centered on the superior end of the patella.

4.5.2 *Measurements and Scoring*

In both studies, a region of interest (ROI) analysis was performed using ImageJ (NIH, Bethesda, MD). For the comparison study, the vessel wall and lumen SNR, and wall-to-lumen contrast-to-noise ratio (CNR) at three locations: the proximal, middle, and distal region of the 3D volume. The inner and outer boundaries of the vessel wall were manually traced from which lumen area, total vessel area, and vessel wall area were obtained from the axial reformats at select locations.

The image quality was scored based on the depiction of the vessel wall and the degree of intraluminal artifacts for the proximal, middle, and distal regions. Specifically, two subscores (0=very poor, 1=poor, 2=fair, 3=good, 4=excellent) were assigned to two images 1.2cm apart in each region and were then averaged to obtain the final score. The reader was blinded to the black-blood techniques. Blood flow measurements were carried out using Flow 3.2 (Medis Medical Imaging Systems, Leiden, The Netherlands).

For the high resolution imaging study, luminal measurements were made at a mid-coronal slice at the level of the patella, and muscle SNR was measured on the gastronemicus muscle in the same slice.

4.6 Results

4.6.1 Black-Blood Magnetization Comparison

All imaging experiments were completed successfully. The optimal black-blood imaging parameters determined by 2D black-blood scout scans were as follows: TI = 366 ± 49 msec for DIR, saturation flip angle = 97º ± 5 º for SPSAT, FOS = 2.0 ± 1.3 cm/s for MSPREP, and TI = 298 ± 47 msec for T2IR. The average heart rate was 55 ± 6 bpm, average blood flow rate was 90 ± 31 mL/min, and average peak blood velocity was 35 ± 6 cm/s.

Figure 4.5 demonstrates typical source images obtained with the four black-blood techniques at proximal, middle and distal locations and a reformatted coronal view of the popliteal artery in one subject. Note that DIR and SPSAT yielded poor blood suppression in the distal half of the 9 cm axial imaging volume, while MSPREP and T2IR provided effective blood suppression and good vessel wall depiction throughout the volume.

Compared to both MSPREP and T2IR, DIR and SPSAT preparations provided significantly higher wall SNR ($P<0.0001$) at the cost of significantly higher lumen SNR ($P<0.05$ at proximal, $P<0.005$ at middle and distal locations) (Fig.4.6). As a result, for DIR and SPSAT, wall-to-lumen CNR from proximal to middle locations decreased by 7% ($P=0.42$) and 49% ($P=0.0001$), respectively, and further decreased by 57% ($P=0.001$) and 44% ($P=0.04$), respectively, from middle to distal locations. While DIR yielded lower wall SNR than SPSAT, it suppressed the blood signal more effectively, leading to significantly higher wall-to-lumen CNR in the middle and distal locations. Compared to T2IR, MSPREP had higher wall SNR, although statistically significant difference was found only in the proximal location (P=0.047). T2IR provided approximately a 22% lower lumen SNR compared to MSPREP at all three locations (P<0.005). The wall-to-lumen CNR difference between T2IR and MSPREP was not found to be statistically significant (P > 0.2).

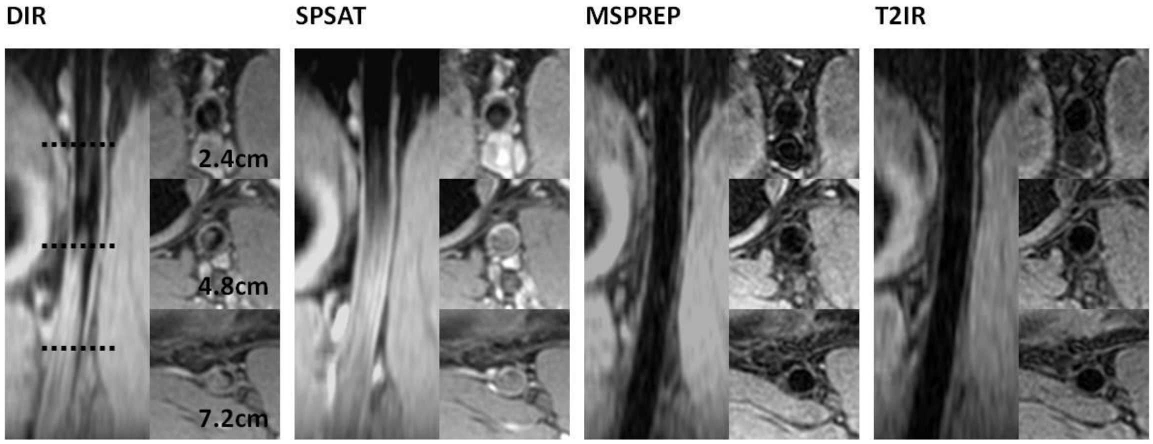

Figure 4.5 Reformatted and axial views of four black-blood techniques.
with respect to wall SNR, lumen SNR, and wall-to-lumen CNR measured at the proximal (2.4 cm from the superior end), middle (4.8 cm), and distal (7.2 cm) regions of the imaging volume (n = 11). The error bars demonstrate the standard error. MSPREP and T2IR provided significantly better blood suppression than both DIR and SPSAT.

Area measurements are summarized in **Table 4.1**. T2IR and MSPREP provided statistically comparable lumen area, total vessel area, and vessel wall area at all three locations. While all techniques yielded statistically comparable vessel wall area at all locations, lumen area and total vessel wall area from DIR and SPSAT were generally significantly smaller than those of MSPREP and T2IR, except in the proximal region.

T2IR and MSPREP received higher image quality scores than either SPSAT or DIR in middle and distal regions, while the differences among all four techniques were not significant or only marginally significant in the proximal region (Fig.4.7). Image quality difference between MSPREP and T2IR was not statistically significant except in the middle region, where T2IR had higher average image quality (P=0.02). DIR and SPSAT received an average score of approximately 2 (“fair”) for all regions. The middle and distal regions receive a better image quality score (2.5-3 or “good”) than the proximal region (2 or "fair") for both T2IR and MSPREP (P<0.01).

Table 4.1. Lumen area, total vessel area, and vessel wall area measurements obtained with black-blood 3D SSFP in the popliteal artery (n = 11).

	DIR	SPSAT	MSPREP	T2IR
Lumen area (mm^2)				
Proximal	29 ± 8†*	27 ± 10†*	33 ± 10	33 ± 10
Middle	23 ± 7†*	20 ± 7†*	29 ± 8	29 ± 8
Distal	16 ± 5†*	17 ± 5†*	24 ± 8	23 ± 6
Total vessel area (mm^2)				
Proximal	52 ± 11*	51 ± 12†*	55 ± 15	55 ± 14
Middle	42 ± 11†*	39 ± 10†*	47 ± 11	48 ± 11
Distal	31 ± 8†*	32 ± 8 †*	39 ± 10	39 ± 9
Vessel wall area (mm^2)				
Proximal	23 ± 4	24 ± 6	22 ± 6	21 ± 5
Middle	19 ± 5	20 ± 3	19 ± 3	19 ± 3
Distal	15 ± 3	15 ± 3	15 ± 3	16 ± 3

† indicates significance compared to T2IR (P < 0.05).
* indicates significance compared to MSPREP (P < 0.05).

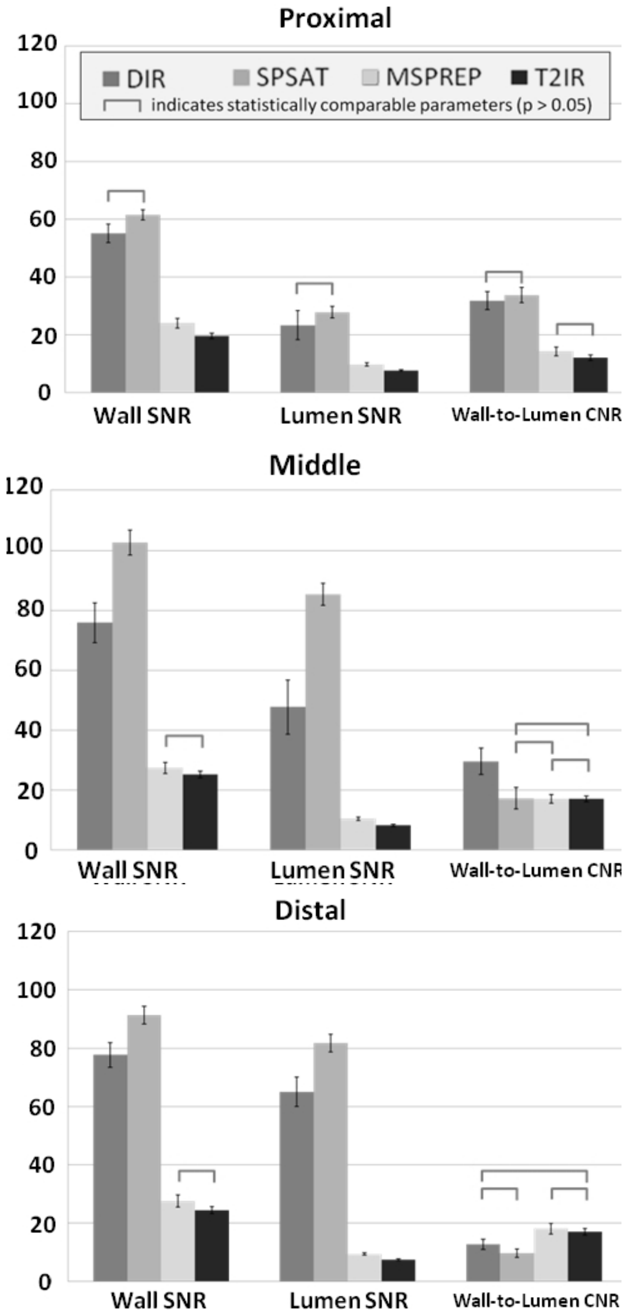

Figure 4.6 Comparison of four black-blood techniques.
with respect to wall SNR, lumen SNR, and wall-to-lumen CNR measured at the proximal (2.4 cm from the superior end), middle (4.8 cm), and distal (7.2 cm) regions of the imaging volume (n = 11). The error bars demonstrate the standard error. MSPREP and T2IR provided significantly better blood suppression than both DIR and SPSAT.

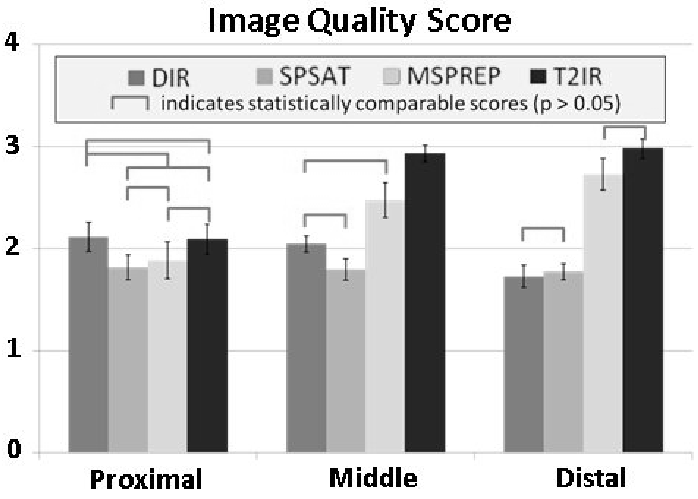

Figure 4.7 Image quality scores of the four black-blood techniques.
at the proximal, mid and distal regions of the 9 cm axial imaging volume. T2IR and MSPREP provided the best overall image quality.

4.6.2 High Resolution Imaging Feasibility

All 11 volunteers were scanned successfully. For the T2IR-SSFP sequence, the optimal inversion TI was determined to be 421± 87 msec. For the T2IR-FSE sequence, 10 out of 11 volunteers yielded optimal suppression at the simulated value (353 msec), which was derived using Bloch simulation based on manual inspection of three two-minute low-resolution scout scans each acquired at TI = 300, 353, and 400 msec. One volunteer had an optimal TI = 300 msec, and an additional 250 msec scout scan was also performed on this volunteer. This resulted in the average TI = 348 ± 15 msec.

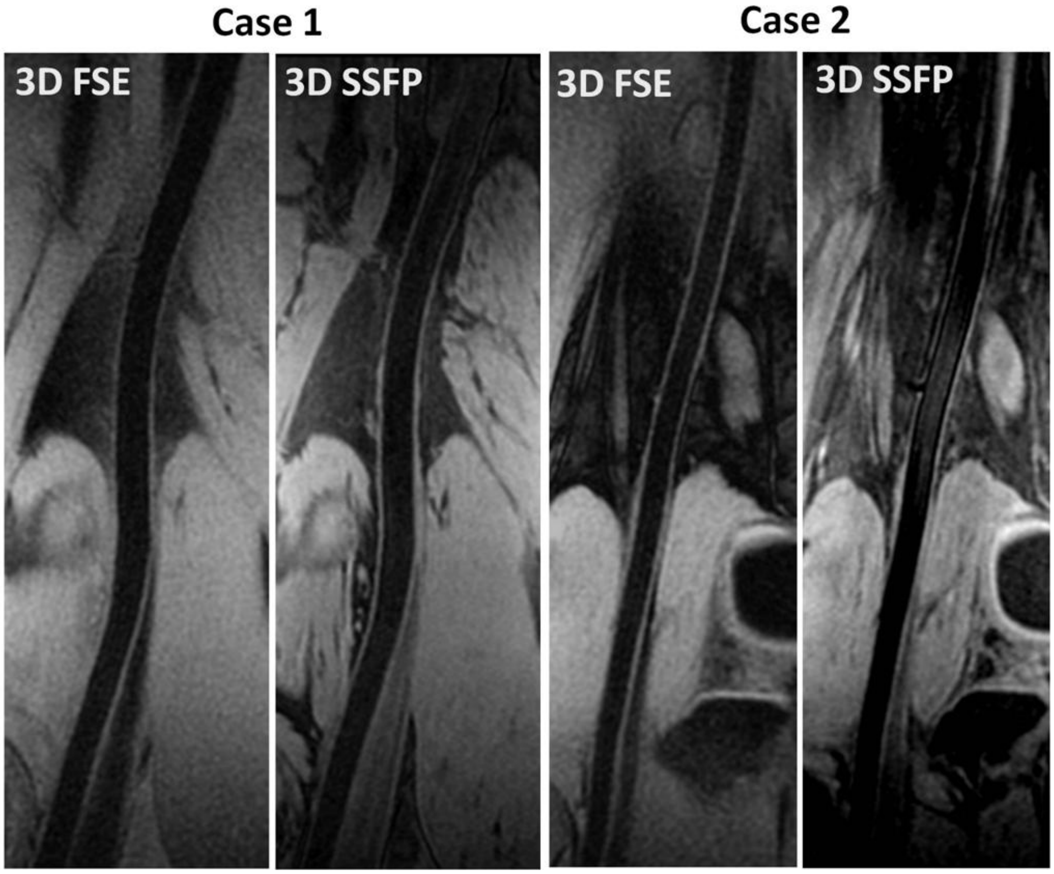

Figure 4.8 Curved reformatted views obtained with 3D FSE and SSFP acquisitions.

Figure 4.8 shows the curved reformatted views obtained with 3D FSE and SSFP acquisitions. In case 1, excellent blood suppression is obtained with both techniques throughout the imaging volume. In case 2, suboptimal blood suppression can be observed in the superior half of the 3D volume acquired with T2IR-SSFP. Muscle SNR from T2IR prepared FSE and SSFP readouts were: 36 ± 4, and 46 ± 8, respectively. The muscle-to-lumen CNR values were: 27 ± 4 and 37 ± 7, respectively. T2IR-SSFP provided 26% higher muscle SNR and 39% higher muscle-to-lumen CNR than T2IR-FSE.

Suboptimal blood suppression was observed in the upper half of the imaging volume in four of the T2IR-SSFP cases (Case 2), while T2IR-FSE provided consistent global blood suppression.

4.7 Discussion

In both studies, the preliminary results in healthy volunteers demonstrated the feasibility of 3D T2IR SSFP vessel wall imaging of the popliteal artery using both an axial prescription, as well as a larger coronal prescription. The T2IR-SSFP technique covering a 10cm axial slab provided good quality black-blood images within a clinically reasonable scan time of 4 minutes, while higher resolution imaging using a coronal view with 20cm coverage is also feasible with increased scan time.

4.7.1 Black-Blood Magnetization Comparison

Compared to conventional inflow-based DIR and SPSAT techniques, flow-independent T2IR and velocity-based MSPREP were found to provide superior blood suppression over a 9 cm axial segment of the popliteal artery, particularly in the distal region where the inflow effect diminishes substantially. Unlike DIR and SPSAT, T2IR and MSPREP do not rely on the inflow of blood with nulled signal into the imaging volume and therefore are also suited for coronal and sagittal acquisitions which can cover the lower extremity vasculature more efficiently than the axial acquisition used in this study (63,72). T2IR can provide reliable blood suppression in other image plane orientations such as in the coronal (72) or oblique planes (73). While the weakness of DIR and SPSAT for thick slab black-blood MRI has been well recognized (74,75) and reported in previous comparison studies (56,75), this work directly compares these techniques against the more recently developed MSPREP and T2IR techniques using the same imaging pulse sequence, scanner setup and subjects. As the effectiveness of blood suppression in DIR and SPSAT degrades with increasing slab thickness, the results presented here may provide practical guidance for thin slab targeted vessel wall imaging of the lower extremities.

Compared to DIR and SPSAT, MSPREP and T2IR provided lower wall SNR, which may be overcome by imaging at higher field strengths such as 3T (76), especially when high spatial resolution is desired. Compared to MSPREP, T2IR provided similar wall-to-lumen CNR, and received comparable or higher image quality scores. While T2IR can provide global blood suppression regardless of blood flow velocity, direction, and spatial resolution, MSPREP relies on velocity-induced signal dephasing within the imaging voxel. It therefore depends on voxel size and may be suboptimal in regions with slow blood flow such as along the wall-lumen boundary (56). This difference may be important in diseased vessels with slower blood flow, although this remains to be investigated.

In a previous study, a single image of the popliteal vessel wall was acquired in ~6.5 min using a 2D T2IR FSE sequence. Here, 56 high resolution popliteal vessel wall images were acquired in about 4 minutes, representing almost two orders of magnitude scan time reduction on a per slice basis. This substantial time saving can be attributed to the higher SNR efficiency of 3D imaging and the SSFP acquisition, which is as shown in the comparison between FSE and SSFP readouts (66). This SNR advantage also permits acquisitions with higher resolution, potentially leading to the improved visualization of small plaque components (75,76).

The optimal FOS value of 2.0 cm/s for MSPREP in the popliteal artery was comparable with that reported by Koktzoglou et al (3.3 cm/s calculated from reported b-value = 1.1 s/mm2 and gradient area = 231 msec mT/m) (52) and Wang et al (3.0 cm/s calculated from reported first-order gradient moment m1 = 784 mT ms2/m) (53)in the carotid artery. However, it was substantially smaller than that reported by Fan et al (135 cm/s calculated from m1 = 17.4 mT ms2/m) for non-contrast MRA of the lower extremity (77). This large discrepancy may be explained by the different purposes of MSPREP: whereas small velocity-encoding gradients may be sufficient to generate good quality angiograms, larger gradients are needed to suppress intraluminal signal.

In this study, a significant decrease in image quality score was noted in the proximal region compared to the middle and distal region scores for both T2IR and MSPREP. This may be due to the increased curvature of the popliteal artery with respect to the axial imaging volume in the proximal region, leading to lower wall SNR (**Figure 4.6**) and increased wall blurring when compared to the middle and distal regions where the artery is fairly straight. The effects of vessel orientation on vessel wall depiction and SNR have been demonstrated in the carotid bifurcation (78). Potential remedies include using higher field strengths to improve SNR and higher resolution to reduce partial volume effect.

This study has several limitations. First, black-blood preparations were synchronized with the peripheral trigger to maximize the blood suppression of the flow-based techniques. As a consequence, each technique imaged the vessel wall at a different phase in the cardiac cycle, which may have affected the vessel wall area measurements. Second, while electrocardiographic gating may have provided improved flow timing for flow-sensitive black-blood techniques, peripheral gating was used to simplify the experimental setup and was found to adequately capture the period of systolic peak flow in all subjects as evidenced by the phase contrast flow measurements. Third, black-blood parameter optimization was performed on a single slice at the middle of the imaging volume to simplify the scout scan procedures, which may lead to suboptimal blood suppression elsewhere within the volume. For flow-based techniques in particular, blood suppression depends on blood velocity and it is generally difficult to determine a single optimal value for the black-blood parameter that would provide uniform blood suppression. Fourth, patients with peripheral arterial occlusive disease were not enrolled in this preliminary study. The performance of T2IR and MSPREP remains to be evaluated in the presence of slower blood flow in diseased arteries. Fifth, plaque characterization generally requires a multi-contrast imaging protocol. While SPSAT does not alter the image contrast of stationary tissues, DIR, MSPREP and T2IR magnetization preparations induce T1, T2, and mixed T1 and T2 weighting, respectively. According to the results of this study, the utility of T2IR for plaque characterization remains therefore to be evaluated.

4.7.2 High Resolution Imaging

This study extended the large-volume 3D T2IR vessel wall MRI of the popliteal artery with 0.8mm isotropic resolution at 1.5T, depicting the vessel wall of the popliteal artery throughout the scan coverage, allowing volume reformats for further examination by a clinician to detect vascular diseases such as atherosclerotic plaque and vasculitis.

Upon comparing T2IR-prepared SSFP and FSE images, SSFP is inherently a bright-blood contrast and is more susceptible to luminal artifacts from inflowing fresh blood beyond the range of the localized transmit coil when T2IR is played out. In this study, three out of the eleven cases yielded inflow of unsuppressed blood signal in the proximal region of the imaging FOV. Use of an array with a larger scan coverage, such as a cardiac array or a body transmit coil would alleviate this problem. Additionally, the use of larger coils would also allow bilateral coverage for examination of both left and right peripheral vasculature simultaneously, and the feasibility of this bilateral imaging approach was recently demonstrated at 3T with the T2IR-FSE sequence, for which an adiabatic fat inversion pulse was used to null the fat signal to address the off-resonance that limits the conventional fat saturation performed at 1.5T.

As demonstrated in this study, FSE with variable refocusing flip angles can prolong the echo train; however, unlike SSFP steady state signal, the FSE pseudo steady state signal may be exhausted before the end of the echo train, which may lead to reduced SNR. This warrants further investigation.

The 12 minute long scan time allowed the acquisition of a truly isotropic coronal volume with 20cm in-plane and 6cm through-plane coverage. True isotropic resolution allows reformatting of the acquired 3D volume into any desired imaging plane, which may be useful for clinical examination of the vessels of interest. However, further scan time reduction would greatly benefit the clinical applicability of this technique. In this study, a full k-space sampling scheme was used to acquire all k-space data for the 3D volume reconstruction; therefore, undersampling strategies can be incorporated for additional scan-time reduction.

4.7.3 Conclusion

In conclusion, flow-independent 3D T2IR SSFP and FSE imaging of the popliteal vessel wall is feasible with effective blood suppression across a thick imaging volume. Compared to conventional DIR and SPSAT techniques for 2D imaging, MSPREP and T2IR provide similar image quality and are better suited for thick slab 3D black-blood vessel wall imaging. A large 20cm coronal volume acquired with T2IR yielded submillimeter and isotropic resolution images of the popliteal vessel wall, which may be useful for assessment of atherosclerotic plaque in patients with peripheral vascular diseases.

Chapter 5

2D FAT IMAGE NAVIGATOR-BASED CORONARY MRA

Coronary imaging requires techniques that address motion of the coronary arteries – namely the cardiac cycle and respiration – which varies from patient to patient. Respiratory motion in particular provides a significant challenge in free-breathing coronary magnetic resonance angiography (CMRA), as it causes the imaging target (the coronary arteries) to change its position throughout the respiratory cycle. Moreover, both cardiac and respiratory motion may vary within each patient’s scan as a result of variable heart rate and drifting breathing pattern, making scan time reduction a notable priority for improving the acquisition.

In the research arena, development of coronary MR imaging technology has been very active and pursued in many fronts: including scan time reduction by undersampling, motion gating and correction, large volume coverage for whole-heart coronary imaging, high-resolution black-blood preparation vessel wall imaging. However, these active and ongoing research interests have yet translated into a coronary imaging technique that can be used routinely in the clinical arena, including at our site at Weill Cornell Medical College. This is primarily due to respiratory motion during the CMRA imaging, which provides a significant challenge from the development of a reliable CMRA imaging technology.

Currently, the state-of-art scanners by the major MRI manufacturers provide the CMRA sequences with navigator that excites a superior-inferior (SI) cylinder of tissue from the diaphragm-liver interface, and have been used in high-resolution coronary imaging for tracking motion and suppressing respiratory motion artifacts that significantly limit this technique. A 1D cylindrical pencil-beam is prescribed on the right diaphragmatic-liver interface to monitor SI motion.

5.1 Clinical Overview

5.1.1 The Pencil-Beam Navigator

Early works with Coronary imaging had incorporated breath-held techniques (79), but using a navigator to monitor respiratory position enabled free-breathing methods that overcame the limitations of breath holding (80); namely the challenges required in patient cooperation, limited duration of data acquisition, and consequently low resolution and image quality. Such techniques acquire a pencil-beam navigator echo during a free-breathing cardiac scan to monitor the motion of the diaphragm dome and to gate data acquisition. Typically, a fixed diaphragmatic navigator measurement is scaled by a factor of 0.6 as an indirect measurement of cardiac position (81), and motion is addressed either in a retrospective manner or in a prospective manner using respiratory gating. However, the pencil-beam navigator approach has several limitations: first, it requires careful positioning away from the heart to avoid interference with imaging echoes, which may lead to operator-dependence. Second, it is sensitive to drifting breathing patterns, which may result in very long scan times. Third, the diaphragm navigator does not directly monitor motion of the heart, and assumes that the motion between the diaphragm and heart to be linear, but in practice, hysteresis has been observed between the two. Additionally, a diaphragm-liver navigator acquisition is only limited to Superior-Inferior (SI) motion tracking, and is unable to track complex motion such as rotation, dilation, and transverse displacements of the coronary arteries.

Therefore, motion gating and correction strategies to address respiratory motion can be categorized into one or more of the following: first is novel navigator design, which utilizes a new navigator pulse for determining cardiac position. The second is prospective navigator data processing, which provides position information of the heart immediately to the MRI scanner data acquisition. The third is retrospective gating/correction, which uses the navigator motion profile to selectively identify the best k-space signal from an oversampled set of data, or applies a motion correction using the measured navigator displacements. Due to the limitations of the existing 1D pencil-beam navigator, navigator technology development for the direct monitoring of motion of the heart during free breathing has recently become an area of great research interest, which has the potential to provide more accurate measurement of cardiac position.

5.1.2 Direct Coronary Navigator Tracking

Over the last decade, numerous methods that directly monitor the position of the heart during free breathing have been developed (19,82-98). One approach is the use of a fat selective navigator that tracks the bulk motion of the epicardial fat in a prospectively gated CMRA (19,82-84). Other approaches utilize self-navigated strategies (85-87). However, these methods only acquire a set of 1D projections of the excited fat or self-navigated volumes, and may lack sensitivity to the actual cardiac motion. Because of this, image-based navigators have been considered, acquiring images of the heart at every heartbeat, either in a self-gated manner (89-91), or using a separate navigator (92-98). For example, Keegan et al. have developed a 3D volumetric navigator that selectively excites the epicardial fat (92), and was used for retrospective motion correction. Image-based navigator approaches have allowed improved tracking of the cardiac position at each heartbeat, but these approaches often perform retrospective gating and motion correction because of the limited time for data extraction and motion detection. Prospective gating strategies have been previously shown to both reduce scan time and improve image quality (99,100) compared to retrospective gating methods, but these real-time methods demand rapid processing to extract motion between the end of navigator acquisition and start of imaging, which is ideally below 40 ms (101). Therefore, image-based strategies with non-rectilinear navigator or self-navigated sampling methods such as 3D Cones (90) trajectory and spiral navigators (92) are unsuited for prospective gating. Only a few image-based navigators with Cartesian sampling schemes have been used for prospectively gated coronary imaging (96-98).

Despite active and ongoing interest in numerous direct cardiac monitoring and image-based approaches at the research level, navigator tracking with a 1D diaphragmatic pencil-beam with prospective gating is still considered the standard approach for clinical coronary MR imaging today, because of its relative ease to set up, its straightforward manner to extract respiratory motion, and its availability on regular scanner hardware from most major MR vendors. On the other hand, many novel approaches at the research level typically require an elaborate setup process that includes one or more calibration scans for navigator planning and saturation band prescriptions (19,96,102), and/or a dedicated processing (87,89,90,92,94) that require dedicated hardware unavailable on standard hospital scanners.

5.1.3 The Goal of this Work

The goal of this work is to develop a method that can be routinely used in the clinical arena while offering reliable coronary images compared the 1D diaphragmatic navigator. This chapter proposes a novel image-based navigator that depicts coronary artery at each heartbeat and employs the navigator image into a prospectively gated CMRA scan. The 2D fat imaging navigator described in 5.2 is rapidly processed in real-time using custom-built software system that performs on the scanner hardware's real-time infrastructure outlined in **Section 5.3**. This system provides operator interaction to rapidly examine and select an ROI suitable for direct coronary motion information extraction at every heartbeat. The 2D navigator real-time image processing is also optimized to meet the timing constraints for allowing prospective gating with PAWS. After completion of the prospectively gated acquisition, the acquired k-space is applied a translational motion correction using the 2D coronary artery displacements. This method is incorporated as 3D coronary SSFP MRA sequence for rapid setup, acquisition, and enhanced image quality compared to conventional methods.

The Cartesian 2D fat image based navigator provides an anatomical 2D image of the epicardial fat surrounding the coronary arteries to clearly visualize coronary artery motion. This navigator is incorporated into a prospectively gated 3D SSFP CMRA sequence with

PAWS for imaging of the right coronary artery (RCA) for rapid image acquisition. The proposed navigator-gated CMRA images with PAWS are then compared with a prospectively gated CMRA using a 1D diaphragmatic pencil beam with a 5mm gating window.

5.2 2D Fat Image Navigator Design

Cardiac fat navigator has the advantage of its signal to not interfere with imaging. Therefore, it can be synchronously be used in Coronary MRA sequences to directly monitor the motion of the heart by spatially & spectrally selectively exciting the epicardial fat surrounding the targeted coronary artery. Recent works has shown this method performed using a 3-echo acquisition for SI, LR, and AP motion extraction, as well as with spiral trajectory to allow 2D and 3D volumetric acquisition and with an in-depth motion correction (92,93).

This section describes the development of the 2D Cardiac Fat Image Navigator pulse sequence design, which acquires a spatially and spectrally selective image of the epicardial fat using repeated phase encodes. Compared to non-Cartesian trajectories such as radial or spiral, this acquisition does not require any computationally heavy reconstructions to generate the navigator image, thereby making feasible the real-time 2D displacement tracking method for prospective PAWS gating as described in **Section 5.3**.

5.2.1 RF Excitation Pulse Optimization

The work here focuses on the development of spectrally fat selective excitation methods, as these RF excitation methods have advantages over water-selective excitation methods as explained previously in **Section 5.1**. Two major families of spectrally selective RF pulses were considered: the first is the Shinnar-LeRoux (SLR) optimized pulses (103), which uses four parameters – namely pulse duration, the RF bandwidth, pass-band ripple percentage, and the stop-band ripple percentage to design the RF time-course using an iterative approach, and are optimized to have the largest pass-band and amplitude. SLR pulse design was performed on a dedicated pulse design software (GE Healthcare, Waukesha WI).

The second family of such spectrally selective pulses includes the spectral-spatial (SPSP) excitation pulses, which provides an additional spatial selectivity through a slab selective encoding (103).

Optimization of the RF excitation was performed in a phantom experiment, where the number of binomial pulse train lobes were varied between 3 and 5 (1-2-1, 1-3-3-1, and 1-4-6-4-1) and spectrally selective RF pulses of lengths 5.2ms, 8.0msec, 10.0 msec and 16.0 msec optimized by the Shinnar-LeRoux algorithm with both linear and minimum phases were also examined. The TR_{nav} and fat-to-water signal intensity ratio were compared to determine the optimal scheme for the 2D fat selective imaging.

5.2.2 The 2D Cardiac Fat Image Navigator Design

From the experiments described in **5.2.1** (results in **5.7.1**), the 1-3-3-1 binomial SPSP excitation was determined to provide the ideal combination of optimal TR_{nav} and a sufficiently high fat-to-water signal intensity ratio for its application as a 2D fat image navigator. Both balanced-SSFP and SPGR readouts were considered, and preliminary experience showed that the SPGR design required no additional preparation before and after the acquisition of the final 2D navigator echo, thus making the time between end of navigator acquisition and CMRA SSFP imaging readouts minimal. In contrast, the SSFP navigator readout required both a dummy preparatory pulse, as well as a half-TR tip-up pulse that added an additional 6.9 msec after navigator phase encodes and prior to the fat saturation pulse.

The proposed Cartesian 2D cardiac fat image navigator acquires a 6cm thick coronal slice that captures the epicardial fat excited by a spectral-spatial (SPSP) excitation (104) (1-3-3-1 binomial pulse train, flip angle = 20°, pulse length = 7.8 ms), and each excitation followed by a single phase encode readout and a spoiler (navigator TR = 12.8 ms). Repeated phase encodes (24-32 echoes) were acquired in a total of 280-380ms, using a reverse centric view order to minimize the time delay between the acquisitions of the k-space center of navigator and image data for improved motion tracking (101).

5.3 Real-Time Interactive Motion Gating with PAWS

The general infrastructure of the real-time processing on the GE scanner platform is described in ***2.3.3***. In order to enable prospective PAWS gating with a 2D fat image navigator, a real-time interactive software system was designed to allow rapid 2D navigator image processing, including during-the-scan ROI selection, template matching, and PAWS gating with sufficient buffer time to account for additional load on the processor during the time-critical block between the end of navigator acquisition and the start of imaging. The developed real-time interactive (RTI) software system is similar in principle to real-time systems previously developed on the GE MRI platforms as described in (105-107).

The primary consideration for enabling 2D motion extraction for prospective gating is given to fast computation to process the navigator k-space data immediately after it is acquired. Once the cardiac motion has been extracted from the navigator data, the software must also rapidly communicate with the waveform generation board that runs the modified MRI pulse sequence and instructs which k-space views should be acquired for the current heartbeat. Additionally, a real-time user interface is desired to allow continuous monitoring and adjustment (if necessary) of navigator signal and tracking parameters. To achieve these goals, a custom-built *back-end* software component is designed to process the raw navigator signal from the receiver coils on the APS board. A second *front-end* component, which runs on the VRE board, provides a graphical user interface (GUI) for real-time display that allows manual prescription of the 2D ROI by the operator from any previously acquired 2D navigator image.

This component runs on the scanner hardware responsible for image reconstruction, but its GUI is forwarded to the scanner console.

Prospective gating using a 2D navigator image requires that all *back-end* computational tasks are completed within *time-critical block*, a temporal window corresponding to the duration between the last navigator echo and the start of SSFP imaging data acquisition. The *front-end* replicates the same data processing as the *back-end* for displaying the navigator images and the motion extracted from the 2D template matching, but its computation completes within a more relaxed time constraint and therefore is *non-time critical*.

The developed software system requires operator interaction for selection of 2D ROI during the initial heartbeats of the CMRA scan (the setup phase). No interaction is necessary during the prospective 3D SSFP CMRA acquisition when the PAWS algorithm is used for gating (the acquisition phase). **Figure 5.1** shows the block diagram of the developed CMRA sequence.

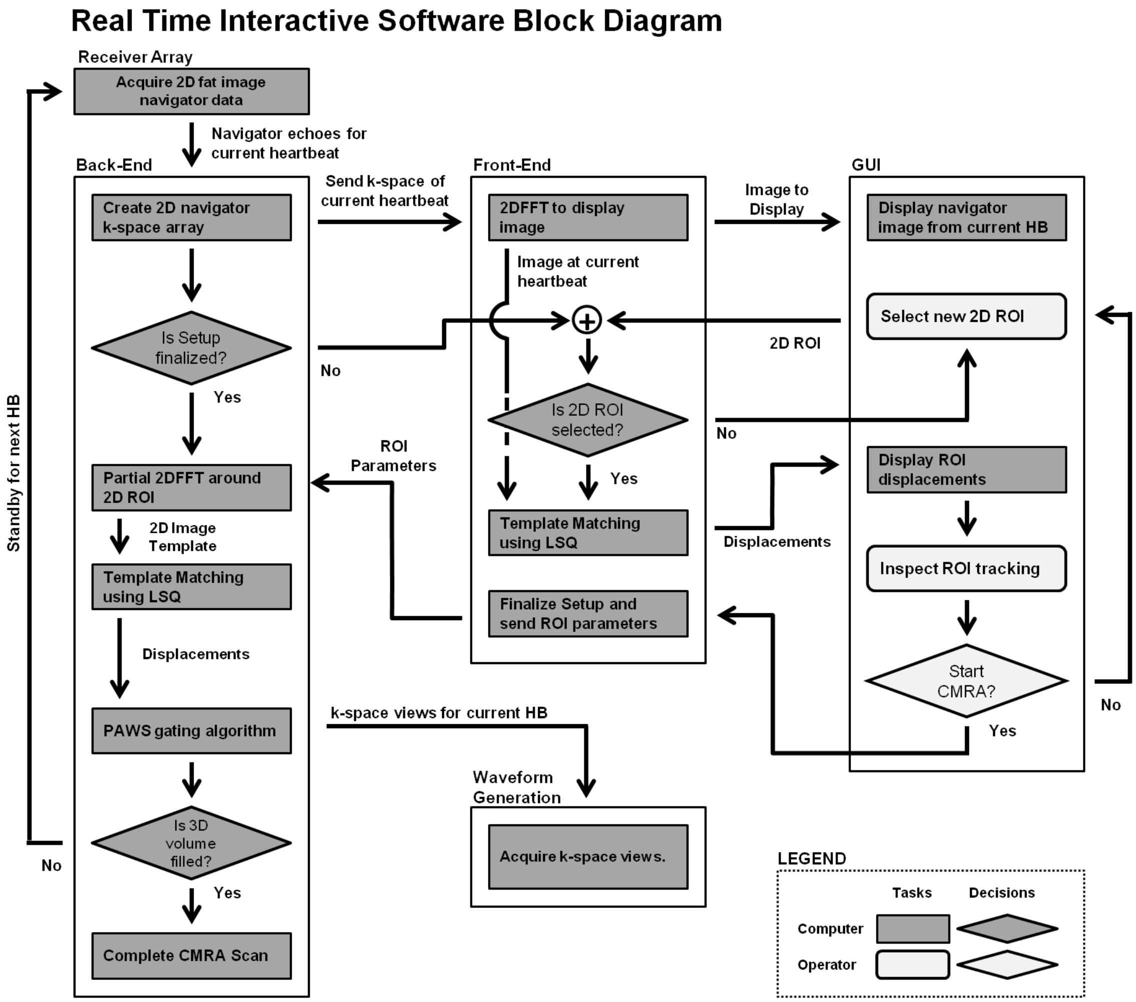

Figure 5.1 Schematic of the Real-Time Interactive Software System
The echoes acquired in one heartbeat are used for ROI selection during setup phase, and are rapidly processed using the PAWS algorithm once CMRA commences. The PAWS-gated acquisition stops when the 3D SSFP k-space volume is filled. Dark-shaded boxes are performed by the computer, and light-shaded boxes are performed by the operator.

5.3.1 Back End Considerations

For real-time processing of the 2D navigator images, the navigator data acquisition and storage utilizes a variation of previously described software systems (83,106-110), which reroutes the storage of navigator echo data onto a dedicated buffer memory on the APS board and shared by our software, instead of reading from the scanner's BAM once data transfer and storage completes.

For prospective gating of navigator data with template matching between each 2D navigator image and an operator-selected 2D region of interest to extract cardiac motion, all computational tasks required completion initially within a 50 msec *time-critical block* (a temporal window corresponding to the duration between final navigator echo and the start of SSFP imaging data acquisition; this was later reduced to 20 msec) with sufficient buffer time to accommodate the heaviest computational load and returning the appropriate set of instructions to the scanner waveform gateway for which set of imaging data to acquire for that heartbeat. For enabling prospective motion correction by slice following, all computation required completion prior to the 6KR ramp-up, whose slab also requires adjustment.

5.3.2 Front End Consideration

Figure 5.2 shows the front end display on the host console. The graphical user interface enables the user to quickly set up, examine, and validate whether the 2D ROI template of the coronary artery is yielding an error-free template match at every heartbeat for accurate coronary mapping.

All non-time-critical tasks performed on the front-end include data storage at each heartbeat, visual displays that update to the most recent heartbeat, 2D ROI selection, and template matching for display. These tasks are performed on the VRE board, which waits for the 2D navigator k-space signal from the APS, and then performs the reconstruction and display of matching results on the front-end GUI displayed on the host. The console GUI enable simple mouse interaction to allow operator selection of the ROI from any previously acquired 2D navigator echoes. The selected ROI is returned to the APS for template matching upon selecting the gating method, and commencing the prospectively gated SSFP acquisition. The 2D image ROI selected by the operator on the host console GUI, the relevant parameters for reconstruction are sent to the APS end and performed outside of the time-critical block for the current heartbeat.

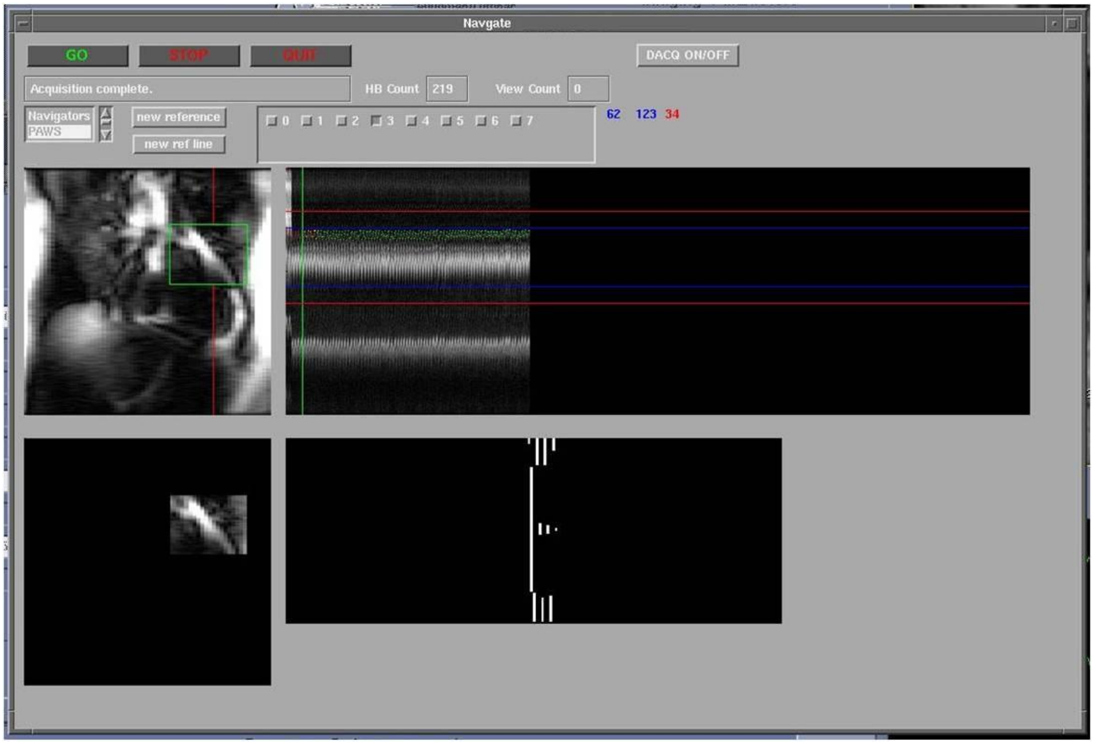

Acquisition complete.

HB Count 219

View Count 0

Navigators PAWS

Figure 5.2 The front end for RTI selection and processing of 2D ROIs. The Coronal 2D navigator image of the epicardial fat is updated after every heartbeat of the scan (top left panel), and a GUI interface allows 2D ROI selection (bottom left panel). The selected ROI can be rapidly checked for accuracy with the timecourse display of an operator-selected line (top right panel). The progress of PAWS gating is also shown (bottom right panel), and is updated every heartbeat until completion of the scan.

5.3.3 Implementation

A dedicated APS processing software component was developed in allowing 2D processing in a fast and efficient manner on the APS, and enabled communication with both the AGP for instructing the scanner and VRE for RTI display and ROI selection.

The *back-end* is initialized by receiving the 2D ROI from the *front-end* selected in the setup phase. For every heartbeat during the acquisition phase, the 2D navigator image is only partially reconstructed around the regions necessary for 2D template matching. The template matching uses a least-squares (LSQ) algorithm (111) over two steps (see below) to reduce computational cost. In our preliminary implementation, only the superior-inferior (SI) displacement component of the detected 2D ROI displacement is used for PAWS gating. The following is a more detailed description of each process:

2D Image Reconstruction: First, a computationally inexpensive 1DFFT is performed over the entire image in the phase encode direction. This is followed by a more computationally expensive 1DFFT in the SI direction to achieve higher spatial resolution by zero-padded interpolation. The FFT in the SI direction is limited to only those readout lines that will be used in the ROI template matching, described below.

Template Matching: A 2D LSQ algorithm is used to perform template matching between the selected ROI and the partially reconstructed navigator image for the heartbeat, from which the 2D displacement values in the SI and left-right (LR) directions are measured. The actual matching algorithm is performed in two steps in order to reduce the overall computation time by eliminating computations on comparisons that are unlikely to match.

First, a 1D LSQ matching of a reference line (selected by the operator during the setup phase) on the navigator image is performed, giving an approximate SI position of the current cardiac position with respect to the 2D template. Second, this displacement is used as an initial guess for a full 2D ROI matching, where the 2D LSQ search is now performed over an additional 16 mm x 16mm search window. This allows for a reduction in the acceptable search window by approximately two folds compared to using a full search window, yielding a similar factor in the processing time saved.

PAWS gating: The measured SI displacement is measured for PAWS gating, (Phase ordering with Automatic Window Selection), which is a sorting algorithm that uses the cardiac position derived from the SI displacement as input to efficiently complete data acquisition. The k-space views acquired per heartbeat segment are organized into groups of views called *frames*, and the frames are numerically indexed for running the PAWS algorithm. In PAWS, each bin represents one-third of the total gating window size, and displacements measured from the 2D navigator are sorted into one of these bins. Each bin has an initial frame, either at the start, middle, or end of all frame indices, and cycle through in modulo 3. The bins initialized on the extremal frames from the start or end of the frame index would acquire frames sequentially towards the middle index, while the middle bin fills its bin in such way to even out the number of unacquired frames between the two adjacent bins. The bottom display panel in **Figure 2.5**, as well as the bottom right panel in **Figure 5.1** shows typical PAWS-gated CMRA scans either in progress or at completion. While PAWS was originally developed to address respiratory drift and reduce residual motion artifacts in long CMRA scans (> ~5mins), it effectively aligns the k-space center at similar respiratory positions and minimizes total acquisition time. The SSFP imaging k-space parameters to acquire for that heartbeat is determined. The AGP waveform processor is instructed by the back-end on which k-space views to acquire for the current heartbeat.

RSP Processing – the PAWS-derived instructions from the APS are updated via communication link with the RSP section of the pulse sequence running on the AGP board. All time-critical computation are completed within the playout of the fat saturation pulse prior to the initial SSFP catalyzation pulse (the first of the 6 Kaiser-Bessel ramp-up pulses) in the RSP section of the pulse sequence running on the AGP.

All time-critical computations require completion within the time needed to perform the fat saturation pulse and the SSFP catalyzation, which was a six Kaiser-Bessel flip angle ramp-up (112). These pulses are approximately 19 ms and 28 ms, respectively.

The k-space views specified in the RSP for the current heartbeat is acquired over mid-diastole of the CMRA scan. The k-space views are sequentially stored on a 2 GB memory block on the BAM, separate from the space allocated for the final 3D volume reconstruction. The scan completes when all k-space views from the optimal set of bins are filled.

After completion of the CMRA scan, the acquired k-space data are re-organized and sorted into the BAM space allocated for GE’s reconstruction software component according to the PAWS-designated bins, as well as the ky and kz position of each acquired view. Once the fully sampled k-space volume from the completed 3-bin gating window is sorted into the BAM section for volume reconstruction, GE’s post-processing software system performs its black-box volume reconstruction which involves a proprietary method to filter, and reconstruct the 3D volume.

5.4 Retrospective Motion Correction by K-Space Shift

Motion correction was performed retrospectively using k-space shift theorem by the 2D displacement measured from the coronary artery branch depicted in the 2D fat image navigator. According to the k-space shift theorem, the acquired coronary MRA k-space data was retrospectively modulated by a linear phase, which corresponds to a pixel-wise translational shift in the image domain.

A region-of-interest (ROI) based template matching was performed with 2D least-squares, and the 2D displacement vector in the frame of the coronal plane was determined. This translational motion was then converted in the double oblique plane of the CMRA prescription using an appropriate rotation matrix. A linearly varying k-space phase shift was applied in each orthogonal direction of the double-oblique plane.

5.5 3D Coronary SSFP CMRA Sequence

Figure 5.3 shows the schematics of the Cartesian 2D fat image navigator-enabled CMRA sequence, which acquired an oblique volume of the right coronary artery (RCA). The 3D SSFP CMRA sequence parameters were as follows: TR = 4.6 msec, TE = 1.8 msec, FA = 90^o, 256x256x12, rBW = ±62.5 kHz, FOV = 26.0 x 26.0 cm, VPS = 32 with a centric view order, slice thickness = 3.0mm. The SSFP imaging train was preceded by a spectrally selective fat saturation and 6 Kaiser-Bessel ramp-up pulses. For the prospectively gated sequence, navigator data transfer was incorporated immediately after the acquisition of the final phase encode, and prior to the 6KR readout.

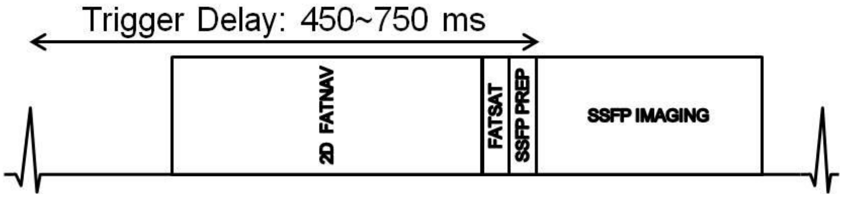

Figure 5.3 Schematic of the 3D SSFP Coronary MRA Sequence
The 3D CMRA sequence is gated by ECG, and a trigger delay measured from a cine-scout scan is used to acquire SSFP CMRA k-space during mid-diastole when there is minimal cardiac motion. The SSFP is preceded by a 2D navigator, 19 msec Fat Saturation pulse, and a 6 Kaiser-Bessel dummy ramp-up pulse train that takes a total of 28 msec to prepare the SSFP signal for image acquisition by minimizing transient oscillation.

For the ungated sequence with 100% navigator efficiency, no data oversampling was performed, and the scan completed after 128 heartbeats (HB) and a total scan time = 2 minutes for a nominal heart rate of 60 BPM. For the prospectively gated CMRA sequence, the scan commenced by acquiring the 2D navigator data, and the operator prescribed a rectangular 2D ROI on the left coronary artery displayed on the RTI interface at end-exhalation. Once the template matching was visually verified, PAWS gated acquisition of the CMRA data commenced by operator input.

5.6 Study Design and Experimentation

5.6.1 Direct Coronary Motion Tracking with 2D Fat Image Navigator

A preliminary in-vivo experiment was performed using the selected scheme on eight healthy volunteers (age = 39 ± 12) on a 1.5T GE Signa HDx scanner using an 8-channel cardiac array under an IRB approved protocol and written informed consent. The protocol additionally included an 8-second breath-held high resolution scan of the 2D fat image navigator, as well as a 640-heartbeat scan that acquired both 2D fat image navigator immediately followed by a 1D diaphragm-liver pencil-beam scan. Image quality scores of the 100% navigator efficient CMRA were assessed by an experienced radiologist in a blinded manner for all experiments. For the ungated and motion corrected CMRA, RCA visualization score was given on a 5-point scale (0=non-diagnostic, 1=poor, 2=fair, 3=good, 4=excellent).

5.6.2 Prospectively gated CMRA

Twelve additional healthy subjects (mean age = 28 years ± 5) were scanned using the proposed prospectively gated 2D fat navigator CMRA sequence, where the PAWS gating window was 2.5 mm. For comparison, a diaphragmatic pencil-beam navigator gated CMRA sequence with equivalent imaging parameters and a 5 mm PAWS gating window was also acquired. The two CMRA sequences were acquired in a randomized order. The coronal 2D navigator had a FOV equal to 27x20 cm (LRxSI), and the pencil-beam length was 13 cm. A rectangular 2D ROI was prescribed around the epicardial fat near the root of the left coronary artery branch (see **Figure 5.2 left panels**), due to its relative ease for ROI selection and visual inspection during setup. A relative image quality score using a 5-point scale (-2 = significantly worse, -1 = marginally worse, 0 = comparable, 1 = marginally better, 2 = significantly better) was assigned, with one image favored after showing a pair of images of the RCA in a blinded manner.

5.6.3 Statistical Analysis

Image quality scores were compared using Wilcoxon's Signed-Rank test, and the student's t-test was used to compare scan times and navigator efficiencies. Pearson's correlation was employed to examine similarities between the epicardial fat motion and the diaphragm-liver motion tracked by both the pencil-beam and the 2D fat image navigator.

5.7 Results

5.7.1 Optimization of 2D Navigator Excitation

Figure 5.4 shows the phantom experiment results. The top row shows the fat selective excitations with the SPSP binomial pulses, and the bottom row shows the SLR-designed RF excitations centered on the fat frequency with 10 and 16 msec pulses. The center frequency of each family of RF pulses was set to -220 Hz for fat selective excitation.

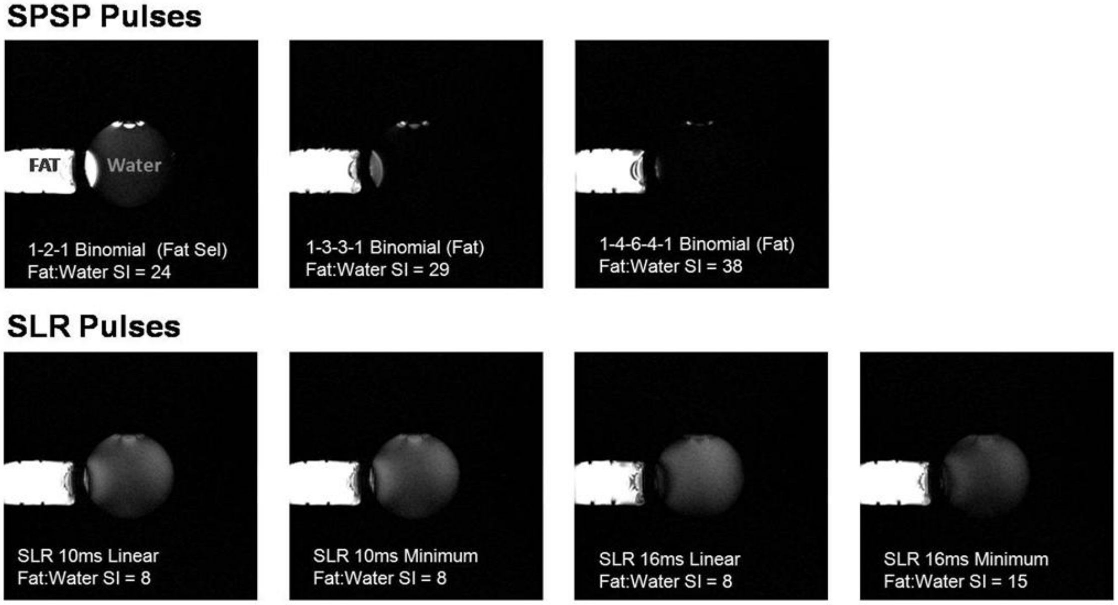

Figure 5.4 Comparison of SPSP designed RF excitations
Fat and water phantom. Between the 1-2-1, 1-3-3-1, and 1-4-6-4-1 SPSP RF excitation pulses, the 1-3-3-1 excitation pulse with an RF duration of 7.9ms, and a total TR_{SPSP} of 12.8ms including readout was selected for the 2D fat image navigator.

Upon examining the fat-to-water signal intensity values, SLR designed RF pulses in general were unable to suppress water signal when compared to the SPSP pulses, and this was more evident with the 5.2 and 8 msec SLR designed pulses (not shown in figure).

Figure 5.5 shows examples of the cardiac images acquired using the proposed SPSP navigator excitation. The first was acquired over a breath-hold over eight heartbeats, and the remaining two were acquired over one heartbeat, reconstructed at the spatial resolution incorporated by the RTI system for prospective gating, as well as at the post processed resolution for retrospective motion correction. In the fat selective images, the liver is also visualized.

Compared to the 1-4-6-4-1 binomial pulse, the 1-3-3-1 binomial pulse was found to provide comparable spectral selection with shorter repetition time (TR_{NAV} = 12.8 msec vs. 15.1 msec). The epicardial fat surrounding the left and right artery branches was better depicted in the coronal plane than in the sagittal plane. For these reasons, a coronal 2D view of the epicardial fat excited with the 1-3-3-1 SPSP binomial pulse train was selected for further experimentation in human subjects.

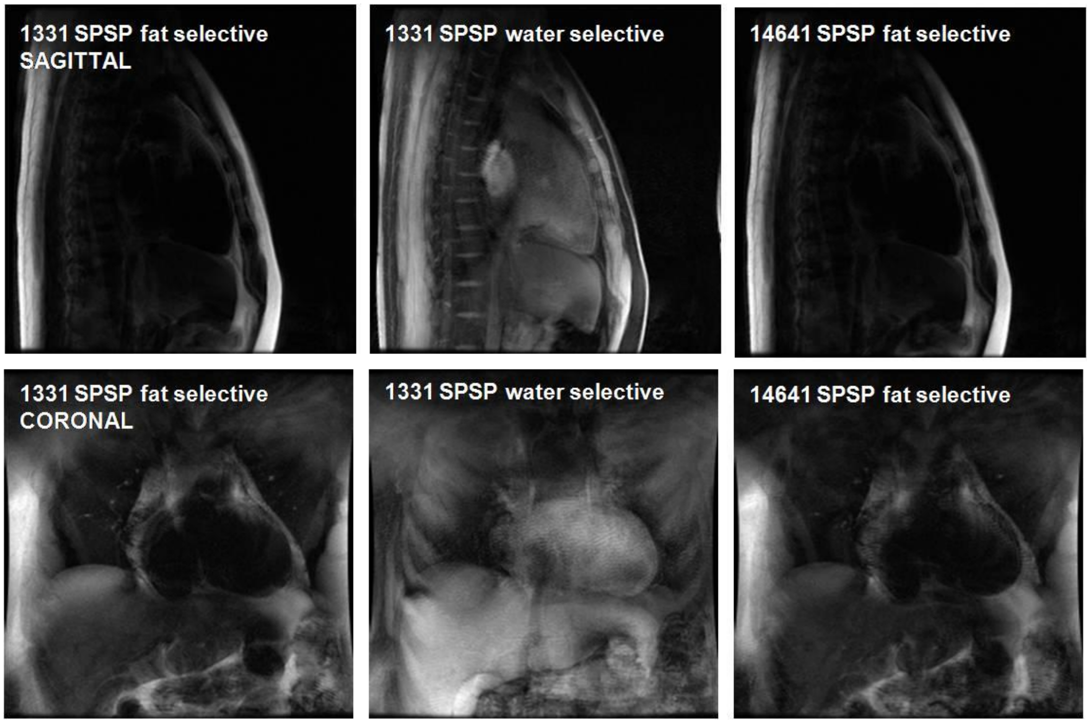

Figure 5.5 SPSP excitation-based Fat Selective Navigators over a breath-hold
1-3-3-1 fat (left), water (middle) and 1-4-6-4-1 fat selective SPSP excitations (right) over a breath-hold with sagittal (top rows) and coronal (bottom rows) views of the chest over a 6cm slab.

5.7.2 Comparison of Coronary Artery position with Diaphragm-Liver Motion

2D fat navigator using the 1-3-3-1 SPSP excitation RF was acquired along with a 1D diaphragmatic pencil-beam navigator at each heartbeat over 640 heartbeats to analyze cardiac and diaphragmatic motion over a 12-minte span to examine drifting in the acquired breathing patterns. **Figures 5.6 and 5.7** each the SI respiratory motions extracted from the 2D cardiac fat and diaphragmatic navigators, and a scatter-plot comparing the two measurements in a pair of subjects.

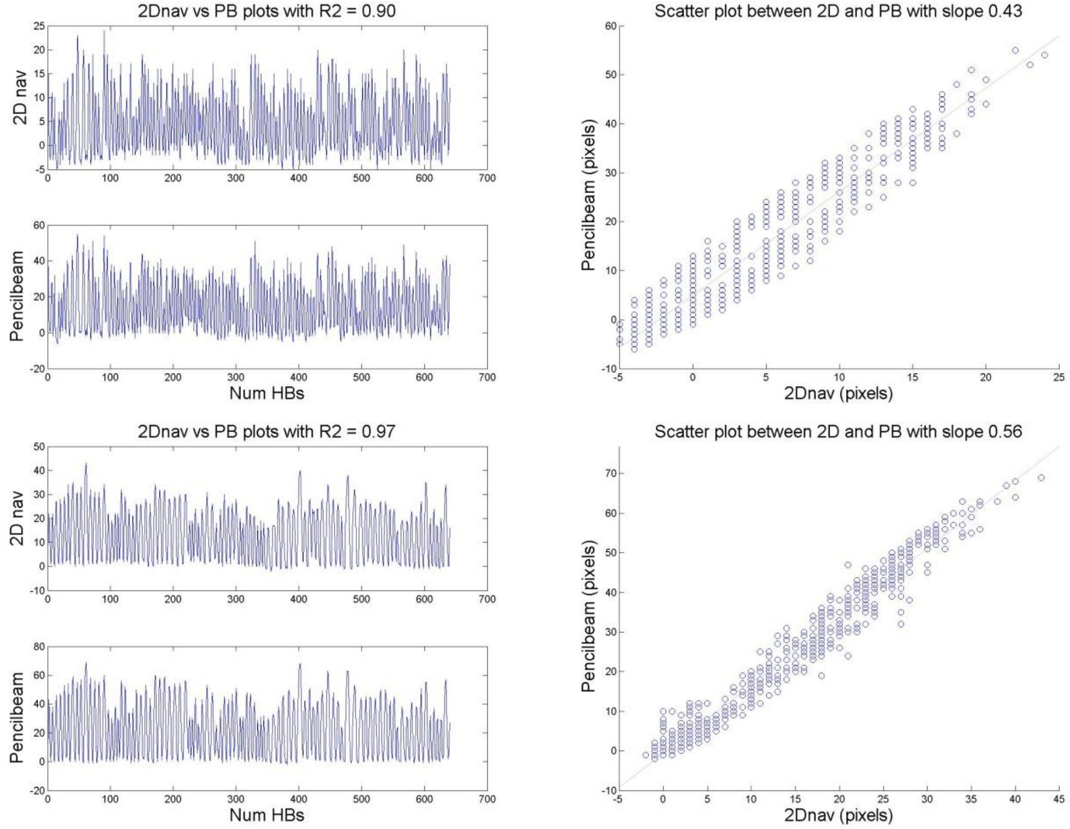

Figure 5.6 Respiratory motion profiles from 2D navigator and 1D pencil-beam

In these two volunteer cases, the direct cardiac SI motion and the diaphragm-liver motion profiles correlated highly over 640 heartbeats. In these cases, drifting was not observed over the 12-minute span, as the relative position at end expiration remained at the same level. Little differences were observed between the two measurements, yielding a narrow scatter plot distribution and a high Pearson's correlation (R^2 = 0.90 and 0.97, respectively).

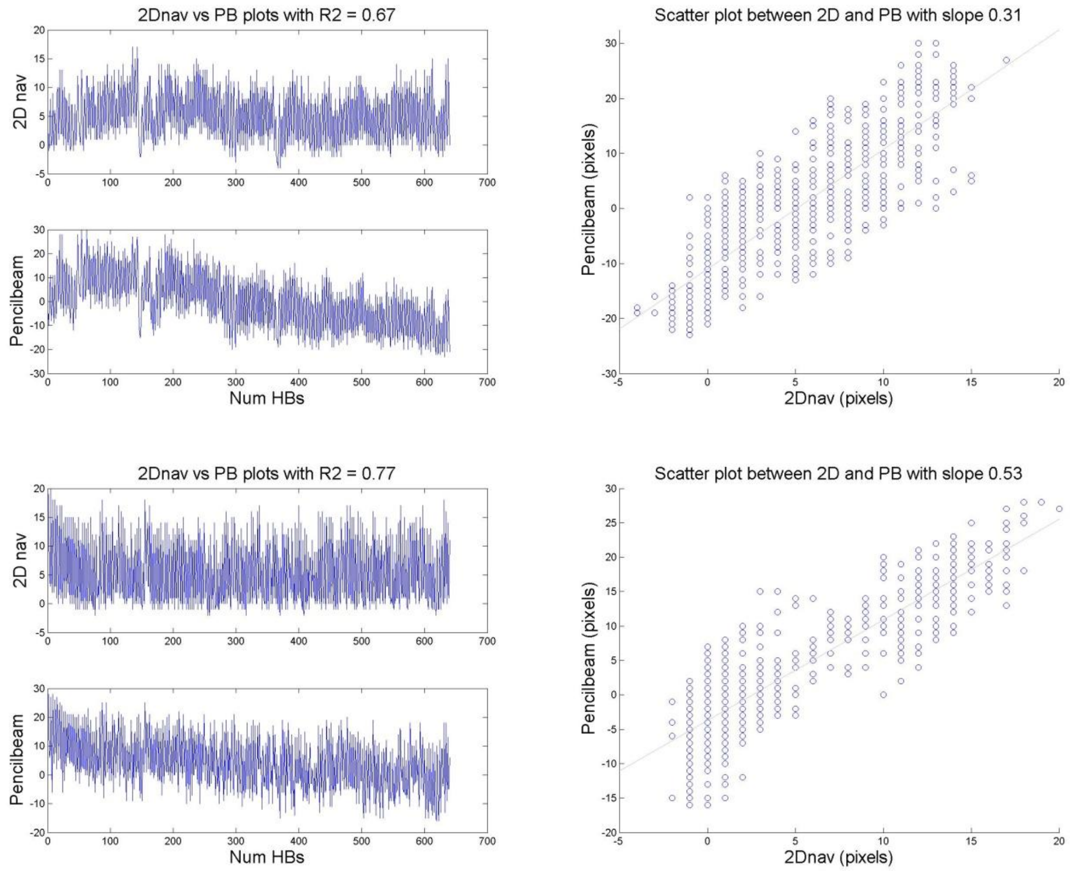

Figure 5.7 Additional motion profiles from 2D navigator and 1D pencil-beam
In these two volunteer cases, the direct cardiac SI motion and the diaphragm-liver motion profiles yielded a lower correlation over the acquired 640 heartbeats. In both of these cases, a drifting breathing pattern was observed over the 12-minute span, as the diaphragmatic position at end expiration reached a lower position over the duration of the scan. However, the extracted cardiac position from the 2D navigator did not show the drifting observed by the pencil-beam, and the Pearson's correlation values were also lower (R^2 = 0.67 and 0.77, respectively) than the cases in Figure 5.6.

The average Pearson's correlation coefficient between diaphragmatic motion and the SI motion extracted from the 2D fat image navigator was $R^2 = 0.80 \pm 0.09$. Subject-to-subject variability between diaphragmatic and cardiac position during respiratory motion can be observed by comparing cases with high correlation **(Figure 5.6)** versus cases with low correlation due to increased motion hysteresis between the heart and the diaphragm **(Figure**

5.7). The motion range of the heart extracted from the 2D fat image navigator over 12 minutes across all eight volunteers was 4.3 ± 0.2 mm in the LR direction, and 11 ± 4 mm in the SI direction. In all cases, a fixed 16 x 16 mm (LRxSI) search window adjusted by an initial guess from 1D LSQ matching was found to provide the same motion estimates as a full 2D template search.

5.7.3 Validation of the Real-Time Interactive Software System

Table 5.1 shows the average time required for each task performed during the *time-critical block* performed on the *back-end* from one volunteer case. The measured time was averaged over 100 consecutive heartbeats from a single coil element.

The ROI-independent process included a total of 196 1DFFTs of size 64 (after zero filling) in the phase encode direction, and required 3.3 ms to complete. For rapid template matching, a computationally more expensive 1DFFT was performed selectively in the readout direction, where each 1DFFT required an average time of 0.3 ms with zero-filling to 256 pixels. The initial 1D LSQ matching required 0.1 ms. The second template matching step required approximately 2-6 ms for a fixed 2D search window of 16 mm x 16 mm, where its variability depended on the ROI area that ranged from approximately 800 to 1800 pixels.

Figure 5.8 the scatter plot of average processing time of the ROI-dependent processes (SI-direction 1DFFTs and 2D LSQ matching) versus the selected ROI size for all 12 volunteer cases. The processing time was averaged over all acquired heartbeats during the acquisition phase for each subject. The processing time was found be to highly correlated ($R^2 = 0.97$) with the size of the selected 2D ROI, indicating that a large 2D ROI becomes more computationally expensive and may result in a run-time error, especially if more than one coil element is used (which further increases processing time linear in the number of coils used). The ROI-dependent processes required 6-13 ms for computation in this study.

The processing time required for PAWS gating and sending instructions to the waveform generator was less than 1 ms, therefore a total of 9-18 ms was required to perform all tasks during the *time-critical block*, leaving sufficient buffer time (> 29 ms) out of the allotted 47 ms between the end of 2D fat image navigator acquisition and the start of CMRA acquisition to avoid any run-time errors during the scan.

Table 1 Average processing time for Operations and Tasks on the back-end processor

Back-End Tasks on the APS	Processing Time
ROI-size Independent Tasks	
LR-direction 1D FFTs (64 points; 196 lines total)	3.3 msec
ROI-size Dependent Tasks (2D ROI = [74x13]; 962 pixels)	
SI-direction 1D FFTs (256 points; 18 lines total)	5.1 msec
1D LSQ matching for estimate of SI position	0.1 msec
2D LSQ matching for detailed template matching	3.1 msec
Miscellaneous Tasks	
PAWS algorithm	< 0.1 msec
Sending Signal to Waveform Generator	< 0.3 msec
Total *Back-End* Processing Time	~ 13 msec

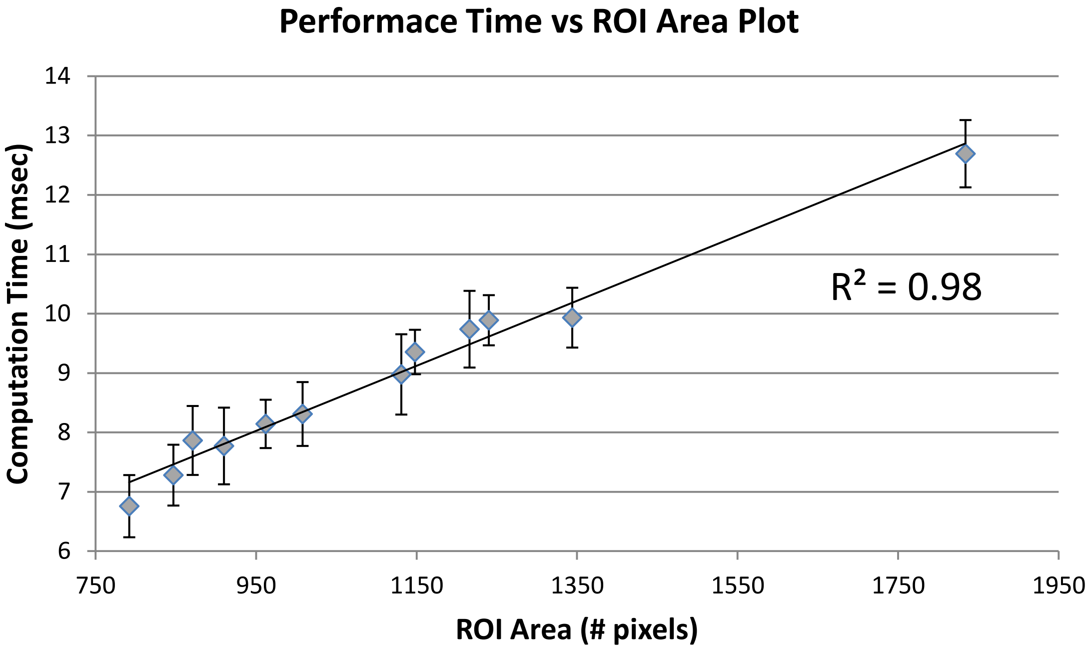

Figure 5.8 2D Template Matching performance Time vs ROI area
This plot indicates that the computation time linearly correlates with the number of pixels selected for the 2D ROI. The computational time over all heartbeats during PAWS-gated acquisition is reported. Standard deviation is shown for each case as an error bar.

5.7.4 Direct Coronary Motion Tracking with 2D Fat Image Navigator

All eight healthy volunteers were scanned successfully. The epicardial fat surrounding two artery branches can be clearly seen in the low-resolution image. **Figure 5.10** shows the coronary artery images from two volunteers, where image quality improved substantially after applying *MC*; this is particularly notable in Case 2, which suffered from severe motion artifacts. The RCA score was significantly higher (P = 0.02) with *MC* (2.8 ± 0.6) than without *MC* (1.9 ± 0.7).

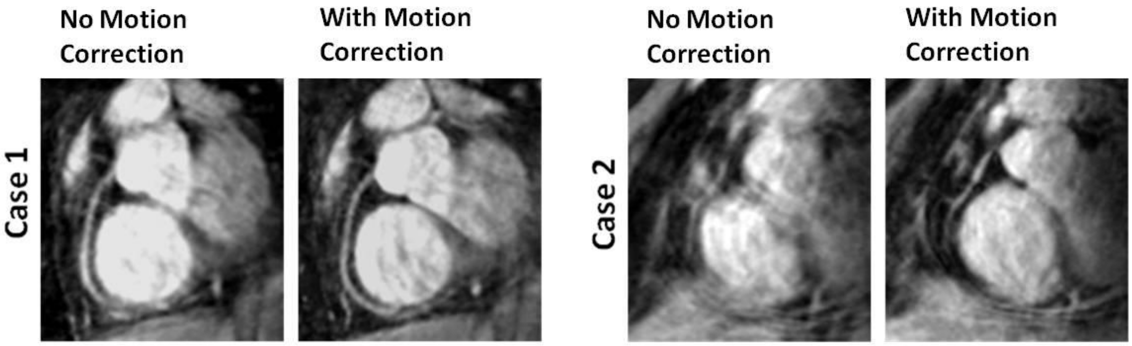

Figure 5.9 Ungated CMRA corrected with retrospective motion correction
Displacements measured from 2D fat image navigator were used for correction by k-space shift.

5.7.5 *Prospectively gated CMRA*

All scans completed successfully. **Figure 5.11** shows examples of the 2D cardiac fat navigator and 1D diaphragmatic navigator gated CMRA. The proposed method required 48 ± 11 sec for navigator setup and 193 ± 28 sec for free-breathing CMRA data acquisition. Pencil-beam navigator gated CMRA had an automated 23 ± 3 sec navigator setup, but took 264 ± 55 sec to complete, resulting in 37% longer imaging time or 41% more heartbeats than the proposed 2D fat image navigator based method. Cardiac fat navigator efficiency was 65 ± 6% (2.5 mm gating window), compared to 46 ± 9% diaphragmatic navigator efficiency (5 mm gating window) ($P < 0.05$). Relative image quality scores favored the proposed method over the conventional diaphragmatic navigator acquisition by 0.8 ± 1.1 ($P < 0.05$). Of the 12 cases imaged, four received comparable image quality scores, three received a +1 score, and four received a score of +2 favoring the proposed method. One case favored the diaphragmatic pencil-beam-derived image, yielding a score of -1.

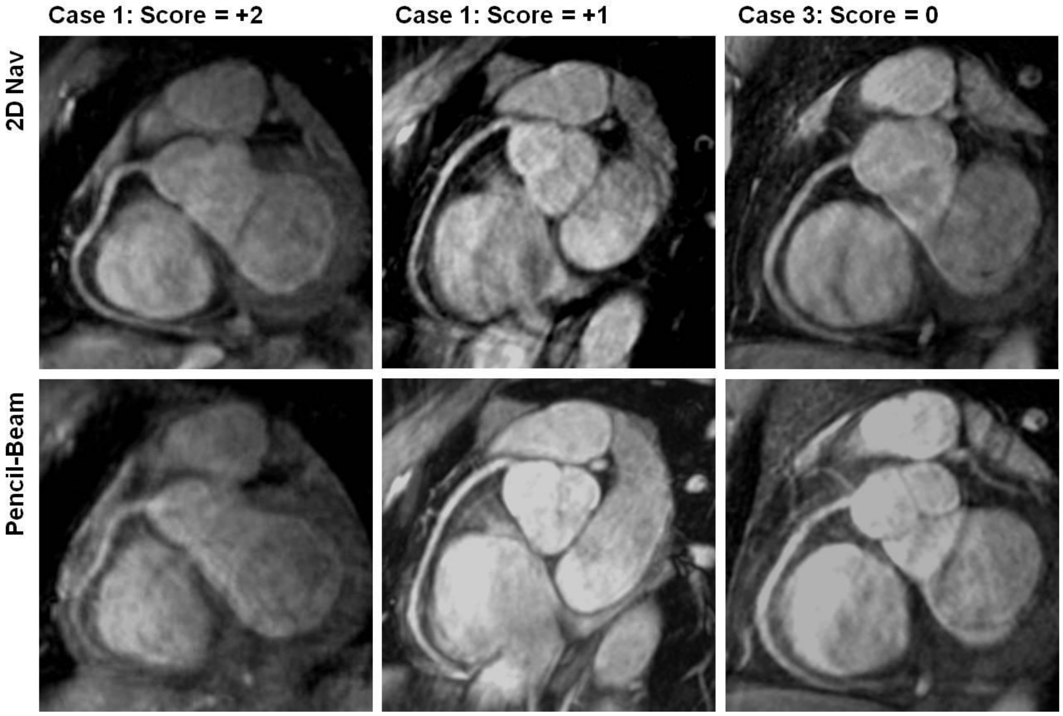

Figure 5.10 Prospectively PAWS-gated CMRA from two Navigator methods
A relative image quality score was assessed in a blinded manner between a pair of volumes. Reformatted images from three volunteer cases are shown, each receiving a score favoring the proposed method by 2, 1, and a comparable score of 0 (left, middle, right). In all of these cases, improved contrast is observed the lumen and the surrounding myocardial tissue due to effective fat suppression likely caused by additional fat excitation by the 2D navigator's SPSP RF pulse train played out before Fat Sat.

5.8 Discussions

The preliminary results in a cohort of healthy volunteers have demonstrated the feasibility of using the proposed 2D fat image navigator with prospective PAWS gating for imaging of the right coronary artery with a 3D SSFP MRA sequence. The proposed 2D fat image navigator 3D SSFP CMRA with PAWS required less than one minute for setup, and was faster while yielding improved image quality compared to the conventional CMRA acquired using prospective PAWS with 1D pencil-beam navigator tracking.

Comparing liver-diaphragm motion with actual cardiac motion has demonstrated a subject-dependent variability in the cardiac position with respect to respiratory motion. This was particularly notable in cases where drifting occurred while tracking diaphragmatic motion with the 1D pencil-beam, but the relative coronary artery positions remained unchanged. The presence of subjects that demonstrated drifting in their breathing position as measured by diaphragmatic motion while the drifting was not observed in the actual cardiac motion strengthens the hypothesis that direct coronary motion tracking may benefit free-breathing coronary MRA sequences, which further validates the direct monitoring approach presented in this chapter.

The proposed 2D navigator-derived images provided good visualization of the epicardial fat surrounding the right and left arteries, allowing tracking of both bulk and localized motion of the entire heart or each depicted artery branch. Unlike water-based 2D image navigators, such as SSFP-based readouts with low flip angles, the fat selective excitation using a 1-3-3-1 binomial SPSP pulse does not excite water signal and therefore minimizes any signal-to-noise ratio (SNR) reduction during imaging, nor does it present cross-talk artifacts between the navigator and 3D imaging FOVs. Compared to using a spatially-non-selective SLR-designed RF excitation, the coronal prescription of the 2D navigator FOV excited by the SPSP pulse was easy to use and did not require additional calibration scans for navigator setup, which was necessary in previous fat selective approaches as these methods used an SLR-designed RF pulse (20) that suppresses the chest wall fat using multiple spatial saturation bands (19,82,83,113,114).

The 2D Cartesian fat selective navigator is computationally efficient for rapid motion signal extraction directly from the epicardial fat branches surrounding the coronary arteries. In this study, our fat selective 2D navigator method isolated images from only one coil element for real-time processing. The implemented rapid navigator processing and motion extraction algorithm took between 10 and 19 ms, enabling prospective gating using the PAWS algorithm without encountering run-time errors. 2D Cartesian acquisition navigators have been used in a prospective manner for coronary imaging (16), reporting a computation time of ~15 ms for processing a 2D navigator image from one coil element with similar spatial dimensions (25x20 cm LRxSI) and reconstructed to a 128 x 64 (SI x LR) matrix during its corresponding *time-critical block* and using a template matching algorithm that detects sub-pixel shifts. The processing times reported in this work are comparable, however our method utilized a 2D navigator image with a matrix of 256x64, which increases the computational cost for both image reconstruction and motion extraction.

The conservative PAWs gating window yielded high quality images of the RCA without the use of motion correction methods in this study. With effective visualization of the epicardial fat surrounding the coronary artery after every heartbeat, it would be possible to employ either prospective (28) or retrospective motion correction schemes (29). Prospective slice following requires that the displacement information is available prior to the first SSFP catalyzation pulse but was not performed in this preliminary study. Retrospective motion correction can be performed using positional information from multiple localized regions of the artery branch. The left and right coronary arteries depicted in our 2D fat image navigator allow selective extraction of localized regions for each artery for motion correction. Prospective and retrospective motion correction schemes using the 2D navigator-derived coronary artery position, and incorporating LR information for prospective PAWS gating are areas of ongoing research.

The proposed navigator acquired up to 32 phase encodes for an acquisition time of up to 380 ms. This may render the detected motion less accurate and may be problematic in patients with high heart rates The use of a reverse centric view order results in the acquisition of central navigator k-space as close as possible to SSFP imaging. . Partial k-space acquisition at the cost of reduced SNR can reduce this acquisition time. Acquiring the navigator with non-rectilinear trajectories such as spiral (12), with real-time regridding performed immediately after each spiral leaf, may be considered to further reduce the navigator duration at the cost of increased processing time.

The RTI software developed for this work was implemented on the standard clinical scanner hardware by enabling the pulse sequence to communicate with two software components that each run concurrently during the CMRA data acquisition without use of any additional dedicated hardware on the GE scanner platform. It was built on top of the previous work designed for 1D PAWS-tracking that is routinely used for clinical imaging. Because of the relative ease of setup, the proposed prospectively 2D navigator-gated CMRA method is promising for clinical use in a patient population, as well as for 2D navigator image processing in other cardiac MR sequences. This is the subject of further investigation.

There are several limitations in this study. First, the long 2D navigator acquisition may not be suitable in combination with magnetization preparation methods. Second, this study did not employ any motion correction methods to further improve image quality or improve the gating window size. Further evaluation of a prospectively gated CMRA combined with either prospective or retrospective motion correction is required. Third, as the proposed navigator image is a projection of a 6 cm coronal slab, the acquired motion cannot distinguish between overlapping artery branches in the 2D projection. This may be addressed by acquiring a navigator volume in 3D (12).

Future work for CMRA imaging include validation of the technique for patient imaging, technology improvement by imaging at higher fields including 3T, and developing an appropriate motion correction method that further exploits the position of arterial branches in 2D for both targeted and whole-heart imaging. As this study utilized a fully sampled data acquisition scheme to enable a 3-minute CMRA scan per targeted coronary plane with a 65% navigator efficiency, additional scan time reduction can be appreciated by incorporating fast undersampling methods (such as parallel imaging and compressed sensing) and more efficient non-rectilinear sampling trajectories into the 3D SSFP acquisition. The 2D navigator imaging method can also be used with other cardiac sequences, such as multi-breath held 3D cine-SSFP imaging with inter-scan motion correction, as well as in non-cardiac imaging applications that may benefit from regular motion monitoring.

In conclusion, direct real-time motion tracking of coronary arteries is feasible using the 2D fat image navigator for a prospectively gated 3D SSFP coronary MRA sequence. The proposed method is capable of rapidly processing 2D navigator data, including ROI selection, template matching, and PAWS gating. This software was demonstrated on a commercial clinical MR scanner, which is potentially useful for further clinical applications. The developed 2D fat image navigator provides shorter scan time, higher navigator efficiency, and improved image quality compared to the conventional 1D diaphragmatic pencil-beam navigator.

Chapter 6

CONCLUSIONS

This thesis describes three techniques; the first developed a routine clinical assessment of diastolic dysfunction through automated processing of routine cine-CMR images. The second developed a large-volume 3D imaging of the peripheral vessel wall through the use of a T2IR black-blood magnetization preparation. The third developed a 2D fat image navigator for direct coronary tracking, and incorporated this into a prospectively gated 3D SSFP CMRA sequence through development of an RTI software system for easy and rapid ROI selection on the existing scanner system.

6.1 Future Work: LV Diastolic Assessment

In this study, volume filling curves generated using the LV-METRIC algorithm differentiated the presence or absence of echo-evidenced diastolic dysfunction in a cohort of subjects with normal systolic function (ejection fraction > 55%). One direction for further investigation is to examine the presence of diastolic dysfunction in another cohort of population with variable systolic function. Another is improving the basal and apical slice segmentation, which can further reduce the time spent for manual inspection of the segmented images.

6.1.1 Subsequent works on Diastolic Assessment

Subsequent work by Mendoza et al (115) have recently demonstrated the use of a combination of volume-filling derived parameters to further distinguish the severity of diastolic performance. The method allowed distinction between normal diastology, mild (grade 1) restrictive filling, and severe (grade 3) impaired relaxation in patients with myocardial infarction who were imaged with cine-CMR. Additionally, assessment of diastolic dysfunction has gained research attention using automated segmentation on other cine-based methods, including phase-contrast MRI. For example, Bollache et al. have shown the validity of using MRI for diastolic assessment through a comparison with echo results (116), and this method also required an automated segmentation algorithm.

In 2012, Maciera et al. provided a review of existing CMR-based approaches that were used in the assessment of diastolic function, which also examined techniques that reported diastolic performance parameters, including: atrial filling ratios, PFR and NPFR; tissue tagging-based myocardial strain analysis, and mitral inflow velocity curves obtained with PC sequences. The cross-literature analysis determined that the DVR 80 presented in (117) (and also **Chapter 3** of this thesis) "*has been shown to yield the best performance versus echocardiography to detect diastolic dysfunction*" (118).

6.1.2 Basal Slice Segmentation

Automated identification and segmentation of the basal and apical slices also pose notable challenges, particularly due to the presence of left ventricular outflow tract (LVOT) on the basal slice, and due to small through-plane motion of the heart that becomes notable in the apical slice. In the study presented in Chapter 3, approximately half of the 101 patient cases required some sort of manual intervention and correction for these extremal slices (117). The absence of an automated method to account for this error and the relatively high correction rate (approximately 1 in every 2 examinations) has resulted in a complete inspection of all segmented volumes manually by the operating clinician to be necessary upon use of the full-volume segmentation using the LV-METRIC algorithm; this has resulted in an average processing time of 2 minutes per case, where the actual algorithm required less than 30 seconds to process the volume curves, and the remaining time was used to manually inspect and correct for any segmentation errors on these extremal slices. Therefore, basal slice, and to a lesser extent apical slice segmentation have been an area of ongoing research interest. Recent works by Wang, Pei et al have shown some promising preliminary results in this respect (119,120). Wang's method uses a continuity assumption in segmented volumes from each image in both spatial (slice) and temporal (phase) directions. This information is used to detect and correct the basal and apical slice volumes accounting for LVOT, as well as through-plane motion during the cardiac cycle (119). Pei's method uses a geometric prior from non-basal slices to first identify the LV axis from the central positions of the LV, then detects the presence of effusion through the LVOT, and corrects for this error by superimposing the boundary from the adjacent slice. These methods are both computationally inexpensive, and have shown potential for further clinical utility to fully automate LV segmentation for both systolic and diastolic analysis using cine-CMR.

6.2 Future Work: 3D Black-Blood Vessel Wall Imaging

The most notable challenge before T2IR prepared vessel wall imaging comes at a cost of reduced SNR due to an overall T2 decay in the muscle signal. In this thesis, multiple echo acquisition (NEX = 2) was used to improve the overall SNR of these images. Migration to 3T (76), as well as using larger receiver arrays with more channels can immediately aid in scan time reduction. Imaging at higher field strengths can lead to improved SNR that is roughly proportional to the magnetic field strength.

6.2.1 Note about 3T imaging

While 3T imaging with FSE has been demonstrated some success in a preliminary study through use of an adiabatic fat inversion with a separate scout scan (76), 3T imaging with SSFP offers greater challenges due to its sensitivity to B0 inhomogeniety, which results in off-resonance artifacts. Alternating TR (ATR) SSFP methods, originally developed for providing spectral selectivity by combining TR of different lengths with RF phase cycling (121), have shown resistance against off-resonance artifacts in prior studies (122-124). Of note, wideband SSFP methods, which utilize a relaxed TR spacing to achieve spectral selectivity (123), may be suited for black-blood SSFP imaging with T2IR. While the longer SSFP TRs may result in fewer views acquired per total segment of T2IR-SSFP’s repetition time, this method can provide both fat suppression, which required an adiabatic inversion and a corresponding scout scan for evaluating fat suppression in (76), and have less constraints due to SAR limitations.

Therefore, ATR-based SSFP acquisition methods, such as T2IR-wideband-SSFP may offer a new direction to further pursue in black-blood imaging at 3T.

6.2.2 Note about Cardiac Black-Blood Imaging

Additionally, cardiac applications of 3D black-blood magnetization preparation have recently become an area of notable research interest for characterization of myocardial function (73,125,126). These methods overcome the limitation of flow-dependent and 2D BB techniques shown for cardiac applications in prior studies (51,127,128). Some preliminary results have recently been demonstrated for both cardiac black-blood, and coronary vessel wall imaging.

T2IR-SSFP, the pulse sequence which was developed in Chapter 4 of this thesis, can be used in combination with the 2D fat image navigator developed in Chapter 5. However, numerous challenges need to be addressed before pursuing coronary vessel wall imaging. These include the long navigator readout time, the relatively low SNR, and the subsequently long scan time to potentially acquire sufficient SNR for coronary wall imaging. Some ideas are listed in **6.3.2**.

6.3 Future Work: 2D Fat Image Navigator Based CMRA

In this thesis, the feasibility of using a fat selective navigator was demonstrated for direct tracking of the coronary arteries. Furthermore, the proposed navigator was incorporated into a prospectively gated CMRA sequence, which has led to both improved navigator efficiency and image quality. Beyond this point, there are several directions for further research. The first is in technology development, and the second is validation in a clinical population.

6.3.1 Technology Development: Further Scan Time Reduction

The first notable improvement can be realized by migrating from a fully sampled Cartesian scheme used in this study to a scheme with some undersampling scheme combined with accelerated imaging reconstruction based on parallel imaging (10,11), compressed sensing (12), or both. The work in this thesis focused on improving both image quality and reducing scan time by utilizing a fully sampled Cartesian scheme, which for the targeted RCA imaging requires just over 128 heartbeats with a centric SSFP scheme (69) that fully samples the 3D k-space volume.

Undersampling of random high-frequency k-space lines has shown significant success in free-breathing CMRA protocols to reduce scan time while fully sampling the center of k-space to maintain high SNR (129,130). Such approaches can be synchronously incorporated into an existing navigator-gated CMRA sequence by modifying the view order scheme to enable fewer acquisitions before acquiring sufficient k-space data for an accelerated coronary image. A Cartesian ky-kz radial scheme (131-133), its variation (129), or in combination with a Compressed Sensing-based reconstruction (130), would merit further investigation. Such approaches would require addressing anticipated eddy-current based artifacts due to k-space skipping with SSFP. A SPGR-based readout could alternatively be used at the expense of high T1/T2 contrast of blood signal offered by balanced SSFP.

Non-Cartesian sampling schemes may also be considered for scan time reduction. Sampling trajectories such as spiral (18,92,134-136), radial (137-139), or hybrid approaches (90) have previously shown success in reducing scan times with additional advantages of being resistant to motion due to oversampling of center of k-space resulting in an overall k-space averaging effect, but image reconstruction from these non-Cartesian reconstruction are usually computationally expensive, and may therefore be more challenging to incorporate at the majority of hospital sites for routine clinical imaging. These approaches must consider both the available scanner hardware on product MRI scanners, in addition to the computational load to perform the necessary processing.

6.3.2 Technology Development: Motion Correction

Further improvements in both navigator image quality and the corresponding motion correction from the acquired 2D navigator approach can benefit the proposed CMRA technique. One major limitation of the low-resolution fat image navigator is the relatively long 2D SPSP-based navigator TR, which makes the repeated phase encodes unsuitable with magnetization preparation methods, such as T2Prep (140,141), as well as black-blood preparations for vessel wall imaging, including MSPREP (54,65,125) and T2IR (65,66). As stated previously in **Section 5.8**, one solution to reduce the SPSP RF excitation pulse duration is to migrate to imaging at 3T (142). While higher field imaging introduces a new set of challenges that are less prevalent at 1.5T, such as B0 field inhomogeneity and relatively high SAR, strategies similar as those presented in ***6.2.1*** can be considered, including ATR-based SSFP acquisition schemes (122,143,144) for both fat saturation and suppression of off-resonance artifacts.

This work incorporated a k-space shift based motion correction to improve image quality in a limited capacity. Delineation of a 2D projection of the target artery has the potential for utilizing a more elaborate motion correction method. One method is to develop a geometric motion model of the target artery branch (or multiple branches in the case of whole-heart CMRA), and apply the geometric model to correct localized regions of the artery branches. As new motion correction methods become realized, the gating window size can also be considered additional scan time reduction.

6.3.3 Validation in Clinical Population

The second direction to pursue is in the imaging of the patient population. Two study designs are proposed here: the first will demonstrate feasibility by imaging patients who undergo routine cardiac MRI at the Weill Cornell Medical College with the following technique. This study will be demonstrated on a small patient population of ~10 subjects. The second study design will image patients who also undergo coronary CTA within 7 days of the CMRA protocol. Patients will be recruited from those referred for a coronary CTA, and the MRI protocol will be offered within 7 days of the CTA. Both MR and CT images will be examined according to the appropriate AHA classification for evaluation of stenotic regions in the coronary artery.

BIBLIOGRAPHY

1. Haacke E, Brown R, Thompson M, Venkatesan R. Magnetic Resonance Imaging - Physical Principles and Sequence Design. New York: Wiley-Liss.; 1999.

2. Bernstein M, King B, Zhou X. Handbook of MRI Pulse Sequences: Academic Press.; 2004.

3. Pauly J, Le Roux P, Nishimura D, Macovski A. Parameter relations for the Shinnar-Le Roux selective excitation pulse design algorithm [NMR imaging]. Medical Imaging, IEEE Transactions on 1991;10(1):53-65.

4. Shinnar M, Eleff S, Subramanian H, Leigh JS. The synthesis of pulse sequences yielding arbitrary magnetization vectors. Magn Reson Med 1989;12(1):74-80.

5. Shinnar M, Bolinger L, Leigh JS. The synthesis of soft pulses with a specified frequency response. Magn Reson Med 1989;12(1):88-92.

6. Shinnar M, Bolinger L, Leigh JS. The use of finite impulse response filters in pulse design. Magn Reson Med 1989;12(1):81-87.

7. Hennig J, Welz AM, Schultz G, Korvink J, Liu Z, Speck O, Zaitsev M. Parallel imaging in non-bijective, curvilinear magnetic field gradients: a concept study. MAGMA 2008;21(1-2):5-14.

8. Stockmann JP, Ciris PA, Galiana G, Tam L, Constable RT. O-space imaging: Highly efficient parallel imaging using second-order nonlinear fields as encoding gradients with no phase encoding. Magn Reson Med 2010;64(2):447-456.

9. Gallichan D, Cocosco CA, Schultz G, Weber H, Welz AM, Hennig J, Zaitsev M. Practical considerations for in vivo MRI with higher dimensional spatial encoding. MAGMA 2012.

10. Wang Y. Description of parallel imaging in MRI using multiple coils. Magnetic Resonance in Medicine 2000;44(3):495-499.

11. KP. P, M. W, MB. S, P. B. SENSE: sensitivity encoding for fast MRI. Magnetic Resonance in Medicine 1999;42(5):952-962.

12. Lustig M, Donoho D, Pauly J. Sparse MRI: The application of compressed sensing for rapid MR imaging. Magnetic Resonance in Medicine 2007;58(6):1182-1195.

13. Griswold M, Jakob P, Heidemann R, Nittka M, Jellus V, Wang J, Kiefer B, Haase A. Generalized autocalibrating partially parallel acquisitions (GRAPPA). Magnetic Resonance in Medicine 2002;47(6):1202-1210.

14. Wildermuth S, Debatin JF, Huisman TA, Leung DA, McKinnon GC. 3D phase contrast EPI MR angiography of the carotid arteries. J Comput Assist Tomogr 1995;19(6):871-878.

15. Edelman R, Chien D, Kim D. Fast selective black blood MR imaging. Radiology 1991;181(3):655-660.

16. Brittain J, Olcott E, Szuba A, Gold G, Wright G, Irarrazaval P, Nishimura D. Three-dimensional flow-independent peripheral angiography. Magn Reson Med 1997;38(3):343-354.

17. Kressler B, Spincemaille P, Prince MR, Wang Y. Reduction of reconstruction time for time-resolved spiral 3D contrast-enhanced magnetic resonance angiography using parallel computing. Magn Reson Med 2006;56(3):704-708.

18. Kressler B, Spincemaille P, Nguyen T, Cheng L, Hai Z, Prince M, Wang Y. Three-dimensional cine imaging using variable-density spiral trajectories and SSFP with application to coronary artery angiography. Magnetic Resonance in Medicine 2007;58(3):535-543.

19. Spincemaille P, Nguyen T, Prince M, Wang Y. Model-free slice following using the cardiac fat navigator: enhanced gating efficiency for 3D SSFP coronary MRA. 2009; Honolulu, HI. p 1891.

20. Jhooti P, Gatehouse P, Keegan J, Bunce N, Taylor A, Firmin D. Phase ordering with automatic window selection (PAWS): A novel motion-resistant technique for 3D coronary imaging. Magnetic Resonance in Medicine 2000;43(3):470-480.

21. Devereux RB, Roman MJ, Liu JE, Welty TK, Lee ET, Rodeheffer R, Fabsitz RR, Howard BV. Congestive heart failure despite normal left ventricular systolic function in a population-based sample: the Strong Heart Study. Am J Cardiol 2000;86(10):1090-1096.

22. Vasan RS, Larson MG, Benjamin EJ, Evans JC, Reiss CK, Levy D. Congestive heart failure in subjects with normal versus reduced left ventricular ejection fraction: prevalence and mortality in a population-based cohort. J Am Coll Cardiol 1999;33(7):1948-1955.

23. Magorien DJ, Shaffer P, Bush CA, Magorien RD, Kolibash AJ, Leier CV, Bashore TM. Assessment of left ventricular pressure-volume relations using gated radionuclide angiography, echocardiography, and micromanometer pressure recordings. A new method for serial measurements of systolic and diastolic function in man. Circulation 1983;67(4):844-853.

24. Villari B, Betocchi S, Pace L, Piscione F, Russolillo E, Ciarmiello A, Salvatore M, Condorelli M, Chiariello M. Assessment of left ventricular diastolic function: comparison of contrast ventriculography and equilibrium radionuclide angiography. J Nucl Med 1991;32(10):1849-1853.

25. Muntinga HJ, van den Berg F, Knol HR, Niemeyer MG, Blanksma PK, Louwes H, van der Wall EE. Normal values and reproducibility of left ventricular filling parameters by radionuclide angiography. Int J Card Imaging 1997;13(2):165-171; discussion 173.

26. van Geuns RJ, Baks T, Gronenschild EH, Aben JP, Wielopolski PA, Cademartiri F, de Feyter PJ. Automatic quantitative left ventricular analysis of cine MR images by using three-dimensional information for contour detection. Radiology 2006;240(1):215-221.

27. Lynch M, Ghita O, Whelan PF. Automatic segmentation of the left ventricle cavity and myocardium in MRI data. Comput Biol Med 2006;36(4):389-407.

28. Codella NC, Weinsaft JW, Cham MD, Janik M, Prince MR, Wang Y. Left ventricle: automated segmentation by using myocardial effusion threshold reduction and intravoxel computation at MR imaging. Radiology 2008;248(3):1004-1012.

29. Lang RM, Bierig M, Devereux RB, Flachskampf FA, Foster E, Pellikka PA, Picard MH, Roman MJ, Seward J, Shanewise JS, Solomon SD, Spencer KT, Sutton MS, Stewart WJ, Group CQW, Committee ASoEsGaS, Echocardiography EAo. Recommendations for chamber quantification: a report from the American Society of Echocardiography's Guidelines and Standards Committee and the Chamber Quantification Writing Group, developed in conjunction with the European Association of Echocardiography, a branch of the European Society of Cardiology. J Am Soc Echocardiogr 2005;18(12):1440-1463.

30. Nagueh SF, Appleton CP, Gillebert TC, Marino PN, Oh JK, Smiseth OA, Waggoner AD, Flachskampf FA, Pellikka PA, Evangelista A. Recommendations for the evaluation of left ventricular diastolic function by echocardiography. J Am Soc Echocardiogr 2009;22(2):107-133.

31. H F. Feigenbaum's Echocardiography. Philadelphia: Lippincott Williams & Wilkins; 1996.

32. Kawaji K, Codella NC, Chu CW, Devereux RB, Prince MR, Wang Y, Weinsaft JW. A Novel Method for Cine-CMR Automated Assessment of Left Ventricular Diastolic Dysfunction. 2009; Honolulu, HI. p 650.

33. Lee HY, Codella NC, Cham MD, Weinsaft JW, Wang Y. Automatic left ventricle segmentation using iterative thresholding and an active contour model with adaptation on short-axis cardiac MRI. IEEE Trans Biomed Eng 2010;57(4):905-913.

34. Papavassiliu T, Kühl HP, Schröder M, Süselbeck T, Bondarenko O, Böhm CK, Beek A, Hofman MM, van Rossum AC. Effect of endocardial trabeculae on left ventricular measurements and measurement reproducibility at cardiovascular MR imaging. Radiology 2005;236(1):57-64.

35. Mancini GB, Slutsky RA, Norris SL, Bhargava V, Ashburn WL, Higgins CB. Radionuclide analysis of peak filling rate, filling fraction, and time to peak filling rate.

Response to supine bicycle exercise in normal subjects and patients with coronary disease. Am J Cardiol 1983;51(1):43-51.

36. Akincioglu C, Berman DS, Nishina H, Kavanagh PB, Slomka PJ, Abidov A, Hayes S, Friedman JD, Germano G. Assessment of diastolic function using 16-frame 99mTc-sestamibi gated myocardial perfusion SPECT: normal values. J Nucl Med 2005;46(7):1102-1108.

37. Iskandrian AS, Bemis CE, Hakki AH, Heo J, Kimbiris D, Mintz GS. Ventricular systolic and diastolic impairment during pacing-induced myocardial ischemia in coronary artery disease: simultaneous hemodynamic, electrocardiographic, and radionuclide angiographic evaluation. Am Heart J 1986;112(2):382-391.

38. Garrido JM, Gerson MC, Hoit BD, Walsh RA. Load independence of early diastolic filling parameters in the anesthetized canine model. J Nucl Med 1993;34(9):1520-1528.

39. Hammermeister KE, Warbasse JR. The rate of change of left ventricular volume in man. II. Diastolic events in health and disease. Circulation 1974;49(4):739-747.

40. Hartiala JJ, Mostbeck GH, Foster E, Fujita N, Dulce MC, Chazouilleres AF, Higgins CB. Velocity-encoded cine MRI in the evaluation of left ventricular diastolic function: measurement of mitral valve and pulmonary vein flow velocities and flow volume across the mitral valve. Am Heart J 1993;125(4):1054-1066.

41. Rathi VK, Doyle M, Yamrozik J, Williams RB, Caruppannan K, Truman C, Vido D, Biederman RW. Routine evaluation of left ventricular diastolic function by cardiovascular magnetic resonance: a practical approach. J Cardiovasc Magn Reson 2008;10:36.

42. Paelinck BP, Vrints CJ, Bax JJ, Bosmans JM, de Roos A, Lamb HJ. Tissue cardiovascular magnetic resonance demonstrates regional diastolic dysfunction in remote tissue early after inferior myocardial infarction. J Cardiovasc Magn Reson 2007;9(6):877-882.

43. Edvardsen T, Rosen BD, Pan L, Jerosch-Herold M, Lai S, Hundley WG, Sinha S, Kronmal RA, Bluemke DA, Lima JA. Regional diastolic dysfunction in individuals

with left ventricular hypertrophy measured by tagged magnetic resonance imaging--the Multi-Ethnic Study of Atherosclerosis (MESA). Am Heart J 2006;151(1):109-114.

44. Yamanari H, Kakishita M, Fujimoto Y, Hashimoto K, Kiyooka T, Katayama Y, Otsuka F, Emori T, Uchida S, Ohe T. Effect of regional myocardial perfusion abnormalities on regional myocardial early diastolic function in patients with hypertrophic cardiomyopathy. Heart Vessels 1997;12(4):192-198.

45. Kudelka AM, Turner DA, Liebson PR, Macioch JE, Wang JZ, Barron JT. Comparison of cine magnetic resonance imaging and Doppler echocardiography for evaluation of left ventricular diastolic function. Am J Cardiol 1997;80(3):384-386.

46. Maceira AM, Prasad SK, Khan M, Pennell DJ. Normalized left ventricular systolic and diastolic function by steady state free precession cardiovascular magnetic resonance. J Cardiovasc Magn Reson 2006;8(3):417-426.

47. Paelinck BP, de Roos A, Bax JJ, Bosmans JM, van Der Geest RJ, Dhondt D, Parizel PM, Vrints CJ, Lamb HJ. Feasibility of tissue magnetic resonance imaging: a pilot study in comparison with tissue Doppler imaging and invasive measurement. J Am Coll Cardiol 2005;45(7):1109-1116.

48. Bellenger NG, Marcus NJ, Davies C, Yacoub M, Banner NR, Pennell DJ. Left ventricular function and mass after orthotopic heart transplantation: a comparison of cardiovascular magnetic resonance with echocardiography. J Heart Lung Transplant 2000;19(5):444-452.

49. Papavassiliu T, Kühl HP, van Dockum W, Hofman MB, Bondarenko O, Beek IA, van Rossum AC. Accuracy of one- and two-dimensional algorithms with optimal image plane position for the estimation of left ventricular mass: a comparative study using magnetic resonance imaging. J Cardiovasc Magn Reson 2004;6(4):845-854.

50. Janik M, Cham MD, Ross MI, Wang Y, Codella N, Min JK, Prince MR, Manoushagian S, Okin PM, Devereux RB, Weinsaft JW. Effects of papillary muscles and trabeculae on left ventricular quantification: increased impact of methodological variability in patients with left ventricular hypertrophy. J Hypertens 2008;26(8):1677-1685.

51. Felmlee J, Ehman R. Spatial presaturation: a method for suppressing flow artifacts and improving depiction of vascular anatomy in MR imaging. Radiology 1987;164(2):559-564.

52. Koktzoglou I, Li D. Diffusion-prepared segmented steady-state free precession: Application to 3D black-blood cardiovascular magnetic resonance of the thoracic aorta and carotid artery walls. J Cardiovasc Magn Reson 2007;9(1):33-42.

53. Wang J, Yarnykh V, Hatsukami T, Chu B, Balu N, Yuan C. Improved suppression of plaque-mimicking artifacts in black-blood carotid atherosclerosis imaging using a multislice motion-sensitized driven-equilibrium (MSDE) turbo spin-echo (TSE) sequence. Magn Reson Med 2007;58(5):973-981.

54. Nguyen T, de Rochefort L, Spincemaille P, Cham M, Weinsaft J, Prince M, Wang Y. Effective motion-sensitizing magnetization preparation for black blood magnetic resonance imaging of the heart. J Magn Reson Imaging 2008;28(5):1092-1100.

55. Liu C, Bley T, Wieben O, Brittain J, Reeder S. Flow-independent T_2-prepared inversion recovery black-blood MR imaging. Journal of Magnetic Resonance Imaging 2010;31(1):248-254.

56. Brown R, Nguyen T, Spincemaille P, Cham M, Choi G, Winchester P, Prince M, Wang Y. Effect of Blood Flow on Double Inversion Recovery Vessel Wall MRI of the Peripheral Arteries: Quantitation with T2 Mapping and Comparison with Flow-Insensitive T2-Prepared Inversion Recovery Imaging. MRM 2010;63(3):736-744.

57. Mani V, Itskovich V, Szimtenings M, Aguinaldo J, Samber D, Mizsei G, Fayad Z. Rapid Extended Coverage Simultaneous Multisection Black-Blood Vessel Wall MR Imaging. Radiology 2004;232(1):281-288.

58. Kim W, Stuber M, Bornert P, Kissinger K, Manning W, Botnar R. Three-Dimensional Black-Blood Cardiac Magnetic Resonance Coronary Vessel Wall Imaging Detects Positive Arterial Remodeling in Patients With Nonsignificant Coronary Artery Disease. Circulation 2002;106(3):296-299.

59. Fayad ZA, Fuster V, Fallon JT, Jayasundera T, Worthley SG, Helft G, Aguinaldo JG, Badimon JJ, Sharma SK. Noninvasive In Vivo Human Coronary Artery Lumen and

Wall Imaging Using Black-Blood Magnetic Resonance Imaging. Circulation 2000;102(5):506-510.

60. Yuan C, Beach K, Smith L, Jr., Hatsukami T. Measurement of Atherosclerotic Carotid Plaque Size In Vivo Using High Resolution Magnetic Resonance Imaging. Circulation 1998;98(24):2666-2671.

61. Makhijani M, Hu H, Pohost G, Nayak K. Improved blood suppression in three-dimensional (3D) fast spin-echo (FSE) vessel wall imaging using a combination of double inversion-recovery (DIR) and diffusion sensitizing gradient (DSG) preparations. Journal of Magnetic Resonance Imaging 2010;31(2):398-405.

62. Isbell D, Meyer C, Rogers W, Epstein F, DiMaria J, Harthun N, Wang H, Kramer C. Reproducibility and reliability of atherosclerotic plaque volume measurements in peripheral arterial disease with cardiovasculr magnetic resonance. J Cardiovasc Magn Reson 2007;9:71-76.

63. Zhang Z, Fan Z, Carrol T, Y. C, Weale P, R. J, Li D. Three-Dimensional T2-Weighted MRI of the Human Femoral Arterial Vessel Wall at 3.0 Tesla. Investigative Radiology 2009;44(9):619-626.

64. Mohajer K, Zhang H, Gurell D, Ersoy H, Ho B, Kent KC, Prince MR. Superficial femoral artery occlusive disease severity correlates with MR cine phase-contrast flow measurements. J Magn Reson Imaging 2006;23(3):355-360.

65. Kawaji K, Nguyen TD, Zou Z, Reig B, Winchester PA, Shih A, Spincemaille P, Prince MR, Wang Y. Three-dimensional flow-independent balanced steady-state free precession vessel wall MRI of the popliteal artery: Preliminary experience and comparison with flow-dependent black-blood techniques. J Magn Reson Imaging 2011.

66. Kawaji K, Nguyen T, Spincemaille P, Reig B, Winchester P, Prince M, Wang Y. High-Resolution 3D Isotropic Black-Blood Imaging with T2prep Inversion Recovery: Comparison between FSE and SSFP. ISMRM. Stockholm, Sweden2010. p 3027.

67. Yarnykh V, Yuan C. Multislice double inversion-recovery black-blood imaging with simultaneous slice reinversion. J Magn Reson Imaging 2003;17(4):478-483.

68. Nayak K, Rivas P, Pauly J, Scott G, Kerr A, Hu B, Nishimura D. Real-time black-blood MRI using spatial presaturation. J Magn Reson Imaging 2001;13(5):807-812.

69. Nguyen T, Ding G, Watts R, Wang Y. Optimization of view ordering for motion artifact suppression. Magnetic Resonance Imaging 2001;19(7):951-957.

70. Busse R, Hariharan H, Vu A, Brittain J. Fast spin echo sequences with very long echo trains: Design of variable refocusing flip angle schedules and generation of clinical T_2 contrast. Magnetic Resonance in Medicine 2006;55(5):1030-1037.

71. Lim RP, Storey P, Atanasova IP, Xu J, Hecht EM, Babb JS, Stoffel DR, Chang H, McGorty K, Chen Q, Rusinek H, Belmont HM, Lee VS. Three-dimensional electrocardiographically gated variable flip angle FSE imaging for MR angiography of the hands at 3.0 T: initial experience. Radiology 2009;252(3):874-881.

72. Nguyen T, Kawaji K, Spincemaille P, Prince M, Wang Y. Large field-of-view submillimeter isotropic resolution bilateral peripheral vessel wall MRI using 3D fast spin echo with flow-insensitive blood suppression at 3 Tesla. ISMRM. Stockholm, Sweden2010. p 3691.

73. Nguyen T, Kawaji K, Spincemaille P, Reig, B., Cham M, Prince M, Wang Y. Three dimensional black blood MRI with extensive cardiothoracic coverage: A feasibility study in healthy volunteers. 2010; Stockholm, Sweden. p 3650.

74. Simonetti O, Finn J, White R, Laub G, Henry D. Black blood T2-weighted inversion-recovery MR imaging of the heart. Radiology 1996;199(1):49-57.

75. Balu N, Chu B, Hatsukami T, Yuan C, Yarnykh V. Comparison between 2D and 3D high-resolution black-blood techniques for carotid artery wall imaging in clinically significant atherosclerosis. Journal of Magnetic Resonance Imaging 2008;27(4):918-924.

76. Nguyen T, Kawaji K, Spincemaille P, Cham M, Winchester P, Prince M, Wang Y. 3D peripheral vessel wall MRI with flow-insensitive blood suppression and isotropic resolution at 3 Tesla. 2009; East Lansing, Michigan, USA. p 3.8.

77. Fan Z, Sheehan J, Bi X, Liu X, Carr J, Li D. 3D noncontrast MR angiography of the distal lower extremities using flow-sensitive dephasing (FSD)-prepared balanced SSFP. Magnetic Resonance in Medicine 2009;62(6):1523-1532.

78. Antiga L, Wasserman BA, Steinman DA. On the overestimation of early wall thickening at the carotid bulb by black blood MRI, with implications for coronary and vulnerable plaque imaging. Magnetic Resonance in Medicine 2008;60(5):1020-1028.

79. Manning WJ, Li W, Edelman RR. A preliminary report comparing magnetic resonance coronary angiography with conventional angiography. N Engl J Med 1993;328(12):828-832.

80. Sachs TS, Meyer CH, Hu BS, Kohli J, Nishimura DG, Macovski A. Real-time motion detection in spiral MRI using navigators. Magn Reson Med 1994;32(5):639-645.

81. Wang Y, Riederer SJ, Ehman RL. Respiratory motion of the heart: kinematics and the implications for the spatial resolution in coronary imaging. Magn Reson Med 1995;33(5):713-719.

82. Nguyen T, Nuval A, Mulukutla S, Wang Y. Direct monitoring of coronary artery motion with cardiac fat navigator echoes. Magnetic Resonance in Medicine 2003;50(2):235-241.

83. Nguyen T, Spincemaille P, Prince M, Wang Y. Cardiac fat navigator-gated steady-state free precession 3D magnetic resonance angiography of coronary arteries. Magnetic Resonance in Medicine 2006;56(1):210-215.

84. Nguyen TD, Spincemaille P, Cham MD, Weinsaft JW, Prince MR, Wang Y. Free-breathing 3D steady-state free precession coronary magnetic resonance angiography: comparison of diaphragm and cardiac fat navigators. J Magn Reson Imaging 2008;28(2):509-514.

85. Stehning C, Börnert P, Nehrke K, Eggers H, Stuber M. Free-breathing whole-heart coronary MRA with 3D radial SSFP and self-navigated image reconstruction. Magn Reson Med 2005;54(2):476-480.

86. Lai P, Larson AC, Bi X, Jerecic R, Li D. A dual-projection respiratory self-gating technique for whole-heart coronary MRA. J Magn Reson Imaging 2008;28(3):612-620.

87. Liu J, Spincemaille P, Codella NC, Nguyen TD, Prince MR, Wang Y. Respiratory and cardiac self-gated free-breathing cardiac CINE imaging with multiecho 3D hybrid radial SSFP acquisition. Magn Reson Med 2010;63(5):1230-1237.

88. Stehning C, Börnert P, Nehrke K, Dössel O. Free breathing 3D balanced FFE coronary magnetic resonance angiography with prolonged cardiac acquisition windows and intra-RR motion correction. Magnetic Resonance in Medicine 2005;53(3):719-723.

89. Bhat H, Ge L, Nielles-Vallespin S, Zuehlsdorff S, Li D. 3D projection reconstruction based respiratory motion correction technique for free-breathing coronary MRA. ISMRM. Stockholm, Sweden2010. p 669.

90. Wu HH, Gurney PT, Hu BS, Nishimura DG, McConnell MV. Free-breathing multiphase whole-heart coronary MR angiography using image-based navigators and three-dimensional cones imaging. Magn Reson Med 2012.

91. Henningsson M, Koken P, Stehning C, Razavi R, Prieto C, Botnar RM. Whole-heart coronary MR angiography with 2D self-navigated image reconstruction. Magn Reson Med 2012;67(2):437-445.

92. Keegan J, Gatehouse P, Yang G, Firmin D. Non-model-based correction of respiratory motion using beat-to-beat 3D spiral fat-selective imaging. Journal of Magnetic Resonance Imaging 2007;26(3):624-629.

93. Scott AD, Keegan J, Firmin DN. Beat-to-beat respiratory motion correction with near 100% efficiency: a quantitative assessment using high-resolution coronary artery imaging. Magn Reson Imaging 2011;29(4):568-578.

94. Scott AD, Keegan J, Firmin DN. High-resolution 3D coronary vessel wall imaging with near 100% respiratory efficiency using epicardial fat tracking: reproducibility and comparison with standard methods. J Magn Reson Imaging 2011;33(1):77-86.

95. Kawaji K, Spincemaille P, Nguyen TD, Thimmappa N, Cooper MA, Prince MR, Wang Y. Direct Coronary Artery Motion Tracking from Cartesian 2D Fat Image Navigator for Motion Corrected Coronary MRA. 2012; Melbourne, Australia. p 3813.

96. Henningsson M, Smink J, Razavi R, Botnar RM. Prospective respiratory motion correction for coronary MR angiography using a 2D image navigator. Magn Reson Med 2012.

97. Dewan M, Hager GD, Lorenz CH. Image-based coronary tracking and beat-to-beat motion compensation: feasibility for improving coronary MR angiography. Magn Reson Med 2008;60(3):604-615.

98. Kawaji K, Spincemaille P, Nguyen T, Thimmappa N, Cooper M, Weinsaft J, Prince M, Wang Y. Efficient Coronary MR Angiography: Real-Time Interactive 2D Fat Image Navigator Motion Tracking for PAWS Gating and Targeted Motion Correction. 2012; Chicago, IL. p Abstract Accepted.

99. Nguyen TD, Spincemaille P, Cham MD, Weinsaft JW, Prince MR, Wang Y. Free-breathing 3-dimensional steady-state free precession coronary magnetic resonance angiography: comparison of four navigator gating techniques. Magn Reson Imaging 2009;27(6):807-814.

100. Du Y, McVeigh E, Bluemke D, Silber H, Foo T. A comparison of prospective and retrospective respiratory navigator gating in 3D MR coronary angiography. Int J Cardiovascular Imaging 2001;17:287-294.

101. Spuentrup E, Manning W, Botnar R, Kissinger K, Stuber M. Impact of navigator timing on free-breathing submillimeter 3D coronary magnetic resonance angiography. Magnetic Resonance in Medicine 2002;47(1):196-201.

102. Nguyen TD, Spincemaille P, Weinsaft JW, Ho BY, Cham MD, Prince MR, Wang Y. A fast navigator-gated 3D sequence for delayed enhancement MRI of the myocardium: comparison with breathhold 2D imaging. J Magn Reson Imaging 2008;27(4):802-808.

103. Meyer C, Pauly J, Macovskiand A, Nishimura D. Simultaneous spatial and spectral selective excitation. Magnetic Resonance in Medicine 1990;15(2):287-304.

104. Meyer CH, Pauly JM, Macovski A, Nishimura DG. Simultaneous spatial and spectral selective excitation. Magn Reson Med 1990;15(2):287-304.

105. Hardy CJ, Darrow RD, Nieters EJ, Roemer PB, Watkins RD, Adams WJ, Hattes NR, Maier JK. Real-time acquisition, display, and interactive graphic control of NMR cardiac profiles and images. Magn Reson Med 1993;29(5):667-673.

106. Tokuda J, Morikawa S, Haque HA, Tsukamoto T, Matsumiya K, Liao H, Masamune K, Dohi T. New 4-D imaging for real-time intraoperative MRI: adaptive 4-D scan. Med Image Comput Comput Assist Interv 2006;9(Pt 1):454-461.

107. Guttman MA, Kellman P, Dick AJ, Lederman RJ, McVeigh ER. Real-time accelerated interactive MRI with adaptive TSENSE and UNFOLD. Magn Reson Med 2003;50(2):315-321.

108. Hardy CJ, Darrow RD, Pauly JM, Kerr AB, Dumoulin CL, Hu BS, Martin KM. Interactive coronary MRI. Magn Reson Med 1998;40(1):105-111.

109. Kerr AB, Pauly JM, Hu BS, Li KC, Hardy CJ, Meyer CH, Macovski A, Nishimura DG. Real-time interactive MRI on a conventional scanner. Magn Reson Med 1997;38(3):355-367.

110. Tokuda J, Morikawa S, Haque HA, Tsukamoto T, Matsumiya K, Liao H, Masamune K, Dohi T. Adaptive 4D MR imaging using navigator-based respiratory signal for MRI-guided therapy. Magn Reson Med 2008;59(5):1051-1061.

111. Wang Y, Grimm RC, Felmlee JP, Riederer SJ, Ehman RL. Algorithms for extracting motion information from navigator echoes. Magn Reson Med 1996;36(1):117-123.

112. Le Roux P. Simplified model and stabilization of SSFP sequences. Journal of Magnetic Resonance 2003;163(1):23-37.

113. Nguyen T, Spincemaille P, Cham M, Weinsaft J, Prince M, Wang Y. Free-breathing 3D steady-state free precession coronary magnetic resonance angiography: Comparison of diaphragm and cardiac fat navigators. J Magn Reson Imaging 2008;28(2):509-514.

114. Kawaji K, Spincemaille P, Nguyen TD, Agrawal M, Prince MR, Wang Y. Epicardial Fat Image Navigator for Direct Cardiac Motion Tracking with Applications in a Prospectively Gated Free-Breathing 3D SSFP Coronary MRA Sequence. BMES. Hartford, CT2011. p 156.

115. Mendoza DD, Codella NC, Wang Y, Prince MR, Sethi S, Manoushagian SJ, Kawaji K, Min JK, LaBounty TM, Devereux RB, Weinsaft JW. Impact of diastolic dysfunction severity on global left ventricular volumetric filling - assessment by automated segmentation of routine cine cardiovascular magnetic resonance. J Cardiovasc Magn Reson 2010;12:46.

116. Bollache E, Redheuil A, Clément-Guinaudeau S, Defrance C, Perdrix L, Ladouceur M, Lefort M, De Cesare A, Herment A, Diebold B, Mousseaux E, Kachenoura N. Automated left ventricular diastolic function evaluation from phase-contrast cardiovascular magnetic resonance and comparison with Doppler echocardiography. J Cardiovasc Magn Reson 2010;12:63.

117. Kawaji K, Codella NC, Prince MR, Chu CW, Shakoor A, LaBounty TM, Min JK, Swaminathan RV, Devereux RB, Wang Y, Weinsaft JW. Automated segmentation of routine clinical cardiac magnetic resonance imaging for assessment of left ventricular diastolic dysfunction. Circ Cardiovasc Imaging 2009;2(6):476-484.

118. Maceira AM, Mohiaddin RH. Cardiovascular magnetic resonance in systemic hypertension. J Cardiovasc Magn Reson 2012;14:28.

119. Wang L, Pei M, Codella NC, Weinsaft JW, Prince MR, Wang Y. Algorithmic Quantification of Left Ventricle Segmentation in 4D Cardiac Magnetic Resonance Imaging based on Spatio-temporal Continuity. 2011; Montreal, Canada. p 3281.

120. Pei M, Wang L, Li J, Fan M, Wang Y. A Geometric Method Based on Mass Center Drifting Detection for Improving Basal Left Ventricle Automated Segmentation. 2011; Montreal, Canada.

121. Leupold J, Hennig J, Scheffler K. Alternating repetition time balanced steady state free precession. Magn Reson Med 2006;55(3):557-565.

122. Nayak KS, Lee HL, Hargreaves BA, Hu BS. Wideband SSFP: alternating repetition time balanced steady state free precession with increased band spacing. Magn Reson Med 2007;58(5):931-938.

123. Lee HL, Shankaranarayanan A, Pohost GM, Nayak KS. Improved 3-Tesla cardiac cine imaging using wideband. Magn Reson Med 2010;63(6):1716-1722.

124. Gonçalves SI, Ziech ML, Lamerichs R, Stoker J, Nederveen AJ. Optimization of alternating TR-SSFP for fat-suppression in abdominal images at 3T. Magn Reson Med 2012;67(3):595-600.

125. Srinivasan S, Hu P, Kissinger KV, Goddu B, Goepfert L, Schmidt EJ, Kozerke S, Nezafat R. Free-breathing 3D whole-heart black-blood imaging with motion sensitized driven equilibrium. J Magn Reson Imaging 2012.

126. Andia ME, Henningsson M, Hussain T, Phinikaridou A, Protti A, Greil G, Botnar RM. Flow-independent 3D whole-heart vessel wall imaging using an interleaved T2-preparation acquisition. Magn Reson Med 2012.

127. Simonetti OP, Finn JP, White RD, Laub G, Henry DA. "Black blood" T2-weighted inversion-recovery MR imaging of the heart. Radiology 1996;199(1):49-57.

128. Yarnykh V, Yuan C. T1-insensitive flow suppression using quadruple inversion-recovery. Magn Reson Med 2002;48(5):899-905.

129. Moghari MH, Akçakaya M, O'Connor A, Basha TA, Casanova M, Stanton D, Goepfert L, Kissinger KV, Goddu B, Chuang ML, Tarokh V, Manning WJ, Nezafat R. Compressed-sensing motion compensation (CosMo): a joint prospective-retrospective respiratory navigator for coronary MRI. Magn Reson Med 2011;66(6):1674-1681.

130. Akçakaya M, Basha TA, Chan RH, Rayatzadeh H, Kissinger KV, Goddu B, Goepfert LA, Manning WJ, Nezafat R. Accelerated contrast-enhanced whole-heart coronary MRI using low-dimensional-structure self-learning and thresholding. Magn Reson Med 2012;67(5):1434-1443.

131. Spincemaille P, Nguyen T, Wang Y. View ordering for magnetization prepared steady state free precession acquisition: Application in contrast-enhanced MR angiography. Magnetic Resonance in Medicine 2004;52(3):461-466.

132. Spincemaille P, Hai ZX, Cheng L, Prince M, Wang Y. Motion artifact suppression in breath hold 3D contrast enhanced magnetic resonance angiography using ECG ordering. Conf Proc IEEE Eng Med Biol Soc 2006;1:739-742.

133. Du J. Contrast-enhanced MR angiography using time resolved interleaved projection sampling with three-dimensional Cartesian phase and slice encoding (TRIPPS). Magn Reson Med 2009;61(4):918-924.

134. Meyer C, Hu B, Nishimura D, Macovski A. Fast Spiral Coronary Artery Imaging. Magnetic Resonance in Medicine 1992;28(2):202-213.

135. Manning WJ, Edelman RR. Magnetic resonance coronary angiography. Magn Reson Q 1993;9(3):131-151.

136. Sakuma H, Takeda K, Higgins CB. Fast magnetic resonance imaging of the heart. Eur J Radiol 1999;29(2):101-113.

137. Peters DC, Korosec FR, Grist TM, Block WF, Holden JE, Vigen KK, Mistretta CA. Undersampled projection reconstruction applied to MR angiography. Magn Reson Med 2000;43(1):91-101.

138. Liu J, Wieben O, Jung Y, Samsonov AA, Reeder SB, Block WF. Single breathhold cardiac CINE imaging with multi-echo three-dimensional hybrid radial SSFP acquisition. J Magn Reson Imaging 2010;32(2):434-440.

139. Nam S, Akçakaya M, Basha T, Stehning C, Manning WJ, Tarokh V, Nezafat R. Compressed sensing reconstruction for whole-heart imaging with 3D radial trajectories: A graphics processing unit implementation. Magn Reson Med 2012.

140. Brittain J, Hu B, Wright G, Meyer C, Macovski A, Nishimura D. Coronary angiography with magnetization-prepared T2 contrast. Magn Reson Med 1995;33(5):689-696.

141. Nezafat R, Stuber M, Ouwerkerk R, Gharib AM, Desai MY, Pettigrew RI. B1-insensitive T2 preparation for improved coronary magnetic resonance angiography at 3 T. Magn Reson Med 2006;55(4):858-864.

142. Bieri O, Mamisch TC, Trattnig S, Kraff O, Ladd ME, Scheffler K. Optimized spectrally selective steady-state free precession sequences for cartilage imaging at ultra-high fields. MAGMA 2008;21(1-2):87-94.

143. Gonçalves SI, Ziech ML, Lamerichs R, Stoker J, Nederveen AJ. Optimization of alternating TR-SSFP for fat-suppression in abdominal images at 3T. Magn Reson Med 2012;67(3):595-600.

144. Lee HL, Shankaranarayanan A, Pohost GM, Nayak KS. Improved coronary MR angiography using wideband steady state free precession at 3 tesla with sub-millimeter resolution. J Magn Reson Imaging 2010;31(5):1224-1229.